JYU DISSERTATIONS 650

Maryam Sabooni Asre Hazer

Electronic and Optical Properties of Gold Clusters with Carbene Ligands using Density Functional Theory Calculations

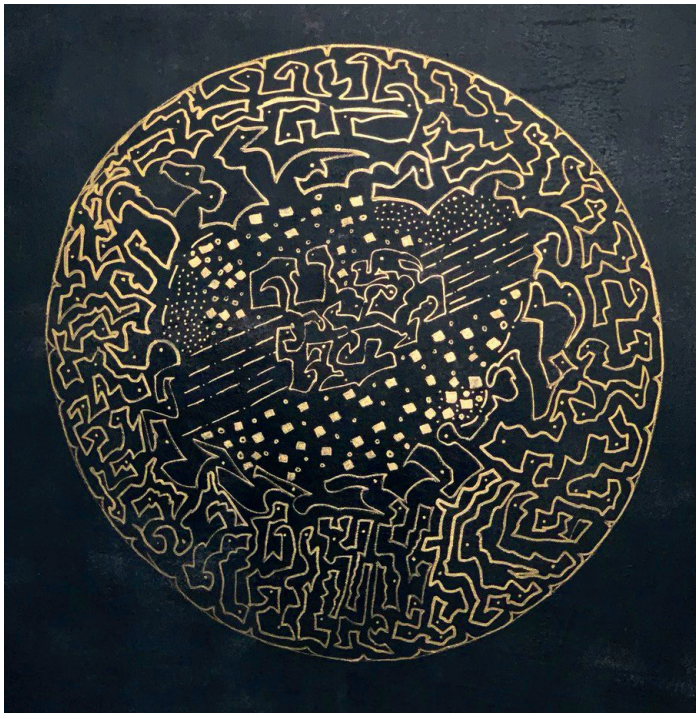

UNIVERSITY OF JYVÄSKYLÄ
FACULTY OF MATHEMATICS
AND SCIENCE

JYU DISSERTATIONS 650

Maryam Sabooni Asre Hazer

Electronic and Optical Properties of Gold Clusters with Carbene Ligands using Density Functional Theory Calculations

Esitetään Jyväskylän yliopiston matemaattis-luonnontieteellisen tiedekunnan suostumuksella
julkisesti tarkastettavaksi yliopiston Ylistönrinteen salissa FYS1
kesäkuun 9. päivänä 2023 kello 12.

Academic dissertation to be publicly discussed, by permission of
the Faculty of Mathematics and Science of the University of Jyväskylä,
in Ylistönrinne, auditorium FYS1, on June 9, 2023 at 12 o'clock noon.

JYVÄSKYLÄN YLIOPISTO
UNIVERSITY OF JYVÄSKYLÄ

JYVÄSKYLÄ 2023

Editors
Hannu Häkkinen
Department of Chemistry, University of Jyväskylä
Ville Korkiakangas
Open Science Centre, University of Jyväskylä

Painting on the cover by Maryam Sabooni Asre Hazer.

At the heart of this painting lies a mesmerizing circular form, meticulously painted with details and captivating characters. While observing the painting from a distance, the finer nuances remain hidden, symbolizing the elusive nature of the nanocluster's world beyond our naked eye's perception. It represents the realm where the intricate dance of particles unfolds. This painting not only serves as a visual spectacle but also embodies the core essence of the thesis. It invites the viewer to ponder the hidden intricacies of the nanocluster world, where perception and understanding are only revealed through dedicated exploration and scientific inquiry.

ISBN 978-951-39-9635-2 (PDF)
URN:ISBN:978-951-39-9635-2
ISSN 2489-9003

Permanent link to this publication: http://urn.fi/URN:ISBN:978-951-39-9635-2

ABSTRACT

Sabooni Asre Hazer, Maryam
Electronic and Optical Properties of Gold Clusters with Carbene Ligands using Density Functional Theory Calculations
Jyväskylä: University of Jyväskylä, 2023, 68 p. (+included articles)
(JYU Dissertations
ISSN 2489-9003; 650)
ISBN 978-951-39-9635-2 (PDF)
Diss.

In recent decades the investigation of ligand-protected metal nanoclusters has garnered significant attention due to their unique properties and molecule-like features. Protected gold clusters have been of particular interest, for which various stabilizing ligands such as phosphines, thiolates, carbenes, and halides have been used. N-heterocyclic carbenes have recently emerged as one of the most essential organic ligands due to their potential to form robust metal-ligand bonds. Recent research has focused on the special role of NHCs in stabilizing gold nanoclusters compared to other ligands. This study employed density functional theory methods to assess the electronic structures and optical absorption properties of ligand-protected metal nanoclusters. Furthermore, molecular dynamics simulations assisted in the recognition of structurally stable isomers. The outcomes presented in this thesis contribute to a broader comprehension on the properties of metal nanoclusters and set the groundwork for exploring novel forms of ligand-protected metal nanoclusters.

Keywords: gold clusters, carbene ligands, density functional theory, molecular dynamics, electronic structure, optical absorption

TIIVISTELMÄ (ABSTRACT IN FINNISH)

Karbeeneilla suojattujen kultaklusterien elektroniset ja optiset ominaisuudet tiheysfunktionaaliteoriaa käyttäen

Viime vuosikymmeninä molekyyleillä suojatut metallinanoklusterit ovat herättäneet merkittävää kiinnostusta nanotieteissä niiden ainutlaatuisten ominaisuuksiensa takia. Erityisen huomion kohteena ovat olleet kultananoklusterit ja niiden suojaamiseksi onkin käytetty monia erilaisia orgaanisia molekyylejä, kuten fosfiineja, tiolaatteja, karbeeneja ja halideja. Näistä molekyyleistä N-heterosyklisten karbeenien on viime aikoina havaittu olevan erityisen mielenkiintoisia, koska ne muodostavat hyvin vahvoja sidoksia metallien kanssa. Viimeaikaiset tutkimukset ovat yrittäneet selvittää karbeenien erityistä luonnetta kulta-nanoklustereiden stabiloinnissa verrattuna muun tyyppisiin suojaaviin molekyyleihin. Mainittuihin aiheisiin liittyen tässä väitöskirjatutkimuksessa käytettiin tiheysfunktionaaliteoriaa ligandisuojattujen metallinanoklustereiden elektronirakenteen ja optisten absorptio-ominaisuuksien tutkimiseen. Lisäksi molekyylidynamiikkasimulaatioiden avulla pyrittiin löytämään ja tunnistamaan rakenteellisesti stabiileja vaihtoehtoisia klusterirakenteita eli klusteri-isomeereja. Tässä väitöskirjassa esitetyt tulokset edistävät metallinanoklustereiden ominaisuuksien ymmärrystä suuremmassa kuvassa ja luovat pohjaa täysin uusien ligandisuojattujen metallinanoklustereiden tutkimukselle.

kultaklusterit, karbeeniligandit, tiheysfunktionaaliteoria, molekyylidynamiikka, elektronirakenne, optinen absorptio

Author

Maryam Sabooni Asre Hazer
Department of Chemistry
University of Jyväskylä
Jyväskylä, Finland

Supervisors

Prof. Hannu Häkkinen
Departments of Physics and Chemistry
University of Jyväskylä
Jyväskylä, Finland

Dr. Sami Malola
Department of Physics
University of Jyväskylä
Jyväskylä, Finland

Reviewers

Prof. Christine Aikens
Department of Chemistry
Kansas State University
Manhattan, KS, USA

Prof. Mikko Linnolahti
Department of Chemistry
University of Eastern Finland
Joensuu, Finland

Opponent

Prof. Alvaro Muñoz-Castro
Department of Chemical Sciences
San Sebastián University
Santiago, Chile

PREFACE

This thesis represents the culmination of my academic pursuits over the past four years as a member of the research group led by Professor Hannu Häkkinen at the University of Jyväskylä. The work presented in this thesis includes one peer-reviewed publication together with a manuscript that both were solely conducted by the researchers at the Nanoscience Center in Jyväskylä, and two additional peer-reviewed publications accomplished through strong international collaboration.

The focus of my research has been on computational investigations for the electronic and optical properties of ligand-protected metal nanoclusters. Throughout my work, I have been fascinated by the unique nature of metal nanoclusters and the findings that come with understanding their origins. This thesis marks a significant milestone in my academic journey, and I am grateful for the opportunity to share my research with the scientific community.

Jyväskylä, March 2023

Maryam Sabooni Asre Hazer

ACKNOWLEDGEMENTS

Throughout my doctoral journey, I have experienced remarkable academic enlightenment, which has expanded my comprehension of achieving a harmonious work-life balance. The challenges and triumphs of this period have fueled my passion and resilience, enabling me to fully embrace my studies and evolve professionally and personally. I am immensely grateful for the opportunities provided to me which have led me to this pivotal moment in my academic journey.

I would like to start by expressing my heartfelt appreciation to my supervisor, Professor Hannu Häkkinen, for believing in me and providing me with the opportunity to be his PhD student. I am immensely grateful for the privilege of working within his group, where my enthusiasm for the field of nanoclusters was sparked. I am truly thankful for the insightful and constructive feedback he provided on my dissertation and the associated research works. In addition to his valuable scientific guidance, I am deeply grateful to him for inspiring me to continue pursuing my artistic endeavors during my PhD studies. It was through his empowering words that I found the motivation to hold several art exhibitions in Finland, a truly rewarding and enriching experience.

I am extremely thankful to Dr. Sami Malola, who supervised me throughout my PhD study. His mentorship has profoundly impacted my scientific growth, as I have gained valuable knowledge and insight from his vast expertise. I am deeply grateful for his significant guidance and input on all my research endeavors and this dissertation, as each discussion has led to a wealth of learning experiences and newfound understanding.

Significantly, I would like to thank Professor Christine Aikens and Professor Mikko Linnolahti for their thorough review and thoughtful remarks on my dissertation. Their substantial input allowed me to improve my dissertation. I sincerely thank Professor Alvaro Muñoz-Castro, for accepting to be my opponent and for devoting his time and effort to the thorough evaluation of my research work.

I would like to express my gratitude to our international collaborators, including the research groups led by Professor Cathleen Crudden, Professor Tatsuya Tsukuda, and Professor Nanfeng Zheng. I am grateful for the opportunity to collaborate with them on research projects beyond those associated with this dissertation, further enriching my academic experience. These experiences, beyond the scope of this dissertation, have allowed me to broaden my knowledge, collaborate with esteemed professionals, and contribute to cutting-edge research.

I would like to acknowledge the Academy of Finland and the C2MCI institute (hosted by the Queen's University in Kingston, Canada) for funding my work.

I would like to extend special thanks to my current and former group members who have been part of my journey since the beginning of my PhD study. Our engaging academic discussions, collaborative experiences with the faculty, and the outdoor activities we participated in together have greatly enriched my overall doctoral experience.

I wish to extend my deepest appreciation to Professor Karoliina Honkala for her consistent availability and the robust support she continually provides to the PhD students. I thank everyone at NSC for creating such a great work environment. I would like to thank Professor Shawulienu Kezilebieke for the inspiring science discussions we had during coffee breaks. I am thankful to Henri Lyyra for teaching me the skills of heavy deadlifts through his gym training.

Last but certainly not least, I would like to express my heartfelt appreciation to my family, who have been a constant source of love, support, and encouragement throughout my academic journey. Through every step of my academic and personal growth, my family has been my rock and offered valuable guidance and reassurance. Their faith in my abilities has continuously inspired me to push beyond my limits no matter the challenges I faced. Their love transcends words and their unwavering presence in my life has been a source of comfort and strength.

ACRONYMS

ASE	Atomic simulation environment
BEEF-vdW	Bayesian error estimation functional-van der Waals
Bn	Benzene
DFT	Density functional theory
DFT-MD	DFT-based molecular dynamics simulations
DTCM	Dipole transition contribution map
e-h	electron-hole
Et	Ethyl
GGA	Generalized gradient approximation
GLLB-SC	Gritsenko-Leeuwen-Lenthe-Baerends (solid correlation)
GPAW	Grid projector-augmented wave (code package)
HOMO	Highest occupied molecular orbital
iPr	isopropyl
KS	Kohn-Sham
LR-TDDFT	Linear-response time-dependent density functional theory
LUMO	Lowest unoccupied molecular orbital
MD	Molecular dynamics
Me	Methyl
M-L	metal-ligand
NHC	N-heterocyclic Carbene
PBE	Perdew-Burke-Ernzerhof exchange-correlation functional
PAW	Projector-augmented wave
PDOS	Projected density of states
p-MBA	para-mercaptobenzoic acid
SAMs	Self-assembled monolayers
SP-DFT	spin-polarized density functional theory
STM	Scanning tunneling microscopy
TD-DFPT	Time-dependent density functional perturbation theory
TD-DFT	Time-dependent density functional theory
UV	Ultraviolet
xc	exchange-correlation
$\mathbf{Y}_{lm}$	Spherical harmonics with quantum numbers l and m

LIST OF INCLUDED ARTICLES

PI **Maryam Sabooni Asre Hazer**, Sami Malola and Hannu Häkkinen. Metal-ligand bond in complexes and clusters of Cu, Ag, and Au, with thiolates, phosphines, and N-heterocyclic carbenes (unsubmitted manuscript). .

PII Paul A. Lummis, Kimberly M. Osten, Tetyana I. Levchenko, **Maryam Sabooni Asre Hazer**, Sami Malola, Bryan Owens-Baird, Alex J. Veinot, Emily L. Albright, Gabriele Schatte, Shinjiro Takano, Kirill Kovnir, Kevin G. Stamplecoskie, Tatsuya Tsukuda, Hannu Häkkinen, Masakazu Nambo, and Cathleen M. Crudden. NHC-Stabilized Au_{10} Nanoclusters and Their Conversion to Au_{25} Nanoclusters. *J. Am. Chem. Soc. Au*, ***2(4)***, *875-885* , (2022).

PIII Kirsi Salorinne, Renee W. Y. Man, Paul A. Lummis, **Maryam Sabooni Asre Hazer**, Sami Malola, Jacky C.-H. Yim, Alex J. Veinot, Wenxia Zhou, Hannu Häkkinen, Masakazu Nambo, and Cathleen M. Crudden. Synthesis and properties of an Au_6 cluster supported by a mixed N-heterocyclic carbene–thiolate ligand. *Chem. Commun.*, ***56(45)***, *6102-6105*, (2020).

PIV **Maryam Sabooni Asre Hazer**, Sami Malola and Hannu Häkkinen. Isomer dynamics of the $[Au_6(NHC\text{-}S)_4]^{2+}$ nanocluster. *Chem. Commun.*, ***58(19)***, *3218-3221*, (2022).

Contribution: In manuscript [PI], the author conducted all calculations and analyses, as well as drafted the initial version of the manuscript. In publications [PII] and [PIII], the author performed all DFT calculations and contributed on writing the computational part of the initial draft. In publication [PIV], the author carried out all DFT calculations with the exception of the molecular dynamics simulations, did the analysis of all data, and also drafted the initial version of the manuscript. Additionally, the author made contributions to the two other publications that are listed on the next page.

LIST OF OTHER ARTICLES

API Hui Shen, Qingyuan Wu, **Maryam Sabooni Asre Hazer**, Xiongkai Tang, Ying-Zi Han, Ruixuan Qin, Chuxin Ma, Sami Malola, Boon K. Teo, Hannu Häkkinen, and Nanfeng Zheng. Regioselective hydrogenation of alkenes over atomically dispersed Pd sites on NHC-stabilized bimetallic nanoclusters. Chem, ***8(9)***, 2380-2392, (2022).

APII Hui Shen, Zhen Xu, **Maryam Sabooni Asre Hazer**, Qingyuan Wu, Jian Peng, Ruixuan Qin, Sami Malola, Boon K. Teo, Hannu Häkkinen and Nanfeng Zheng. Surface Coordination of Multiple Ligands Endows N-Heterocyclic Carbene-Stabilized Gold Nanoclusters with High Robustness and Surface Reactivity. Angew. Chem., ***133(7)***, 3796-3802, (2021).

CONTENTS

1 INTRODUCTION

To begin this chapter, I refer to Richard Feyman's inspiring speech "There is plenty of room at the bottom", delivered on December 1959 at the American physical society meeting in Pasadena, California [1]. In his speech, Feynman underlined the significance of exploring and understanding the function of matter at the nanoscale. He sparked a wave of interest in the field of nanoscience by emphasizing the idea of manipulating individual atoms and molecules to build nanomaterials, as well as developing machines and devices to operate with these materials on a far smaller scale than was previously considered possible. The advancement in the field of nanotechnology has led to the development of various machines and devices and has opened up new opportunities in the field of materials science with the development of tip-based microscopic and spectroscopic techniques. These techniques involve the use of sensitive measurements of electrons, forces, and photons in order to achieve incredibly high resolutions and sensitivities in the characterization and manipulation of materials at the atomic scale. One such invention that revolutionized the field of nanoscience is the scanning tunneling microscope (STM) [2]. The introduction of STM represents a significant breakthrough in the investigation of surface morphology and electronic structure, allowing for the creation and manipulation of atomic structures with exceptional atomic resolution. This instrument employs scanned local probes with a high spatial resolution to provide real-space information on surface morphology and electronic structure.

In the decades after Feynman's speech, there has been a surge of interest in the study of ligand-protected metal nanoclusters. The size of these clusters typically ranges from ten to a few hundred atoms (with the dimension up to a few nanometers), which makes them known as the bridging link between individual atoms and nanoparticles of the corresponding metals. Unlike metal nanoparticles, whose properties are defined by an average size and size distribution, nanoclusters are atomically-precise compositions with crystallographically resolved structures that

are accurately described by a chemical formula. Thus, the incorporation or removal of a single atom or electron may trigger a profound rearrangement of their electronic and geometric structures.

Extensive research has been conducted on ligand-protected group-11 metal (Cu, Ag, Au) nanoclusters [3, 4, 5] with dimensions close to the Fermi wavelength of electrons (about 1 nm) displaying pronounced quantum size effects. This thesis work focuses on gold nanoclusters that exhibit unique properties that differ from those of larger equivalents such as Au nanoparticles. In contrast to plasmonic Au nanoparticles, which exhibit continuous energy levels [6, 7], gold nanoclusters possess discrete electron states [8, 9, 10]. As a result, they display remarkable molecule-like features, such as a bandgap between the highest occupied molecular orbital and the lowest unoccupied molecular orbital (HOMO-LUMO), distinct absorption bands that arise from single electron transitions, high catalytic activity, enhanced photoluminescence, and chirality [11, 12, 13, 14, 15, 16].

The stabilization of metal nanoclusters is a necessary requirement owing to their high specific surface area and consequent high surface energy. To date, a variety of ligand groups have been employed to stabilize gold nanoclusters, including phosphines, thiolates, carbenes, halides, and alkynyls [17, 18, 19, 20, 21, 22, 23, 24]. The advancement of research in molecule-like properties of ligand-protected gold clusters has opened up possibilities for diverse applications such as catalysis, luminescence, and biosensing [17, 25, 26].

Initially, phosphines were employed to stabilize Au nanoclusters [27]. Ever since several successful efforts in the synthesis and characterization of phosphine-stabilized gold nanoclusters have been reported [28, 29, 30, 31, 32, 33]. The crystallization of the first thiolate-protected Au_{102}(*p*-MBA)$_{44}$ (*p*-MBA is 4-mercaptobenzoic acid) [34], stimulated further studies in the area of thiolate-protected gold nanoclusters [35, 36, 37, 38]. In addition to phosphines and thiolates, a variety of organic ligands such as selenolates [39], tellurolates [40], and N-heterocyclic carbenes (NHC) [41] have been employed to synthesize precise ligand-protected gold nanoclusters.

In recent years, there has been a growing body of evidence pointing to the importance of NHC ligands to stabilize gold nanoclusters. NHCs consist of a heterocyclic ring structure with at least one nitrogen atom located adjacent to the carbene wherein two coordinatively unsaturated electrons are present. The electronic sensitivity toward structural modifications makes them one of the most essential organic ligands to stabilize gold nanoclusters [42]. NHCs have been recognized for their potential to form robust and enduring metal-ligand bonds, which is attributed to the considerable strength of the σ-bond between the NHC and metal atoms. Consequently, NHCs are becoming one of the widely researched ligand types to functionalize gold nanoclusters both in organic and aqueous solvents

[22, 43, 44, 45].

The first crystal structure of NHC-protected Au nanocluster was reported for the $[(NHC\text{-}Au)_3]^+$ cluster [46]. The successful synthesis of NHC-protected Au nanoclusters containing more than three Au atoms was achieved in a study conducted by Crudden *et al*. [47]. In this study one PPh_3 ligand in $[Au_{11}(PPh_3)_8Cl_2]^+$ cluster was substituted with NHC, resulting in the increased stability of gold clusters comparing to all-phosphine clusters. These results directly elucidate the intrinsic properties of NHC, thereby emphasizing its prominent role in stabilizing gold clusters. This outcome also serves as compelling evidence of the superior stability of the C-Au bonding over the P-Au bonding. Subsequently, the first two fully NHC-stabilized Au clusters, $[Au_{13}(NHC)_9Cl_3]^{2+}$ [43] and $[Au_{25}(NHC)_{10}Br_7]^{2+}$ [48] were reported. Crudden *et al*. showed that the NHC-stabilized Au_{13} clusters exhibit higher stability than the corresponding phosphine clusters. They also observed strong luminescence properties, making them potentially useful in a variety of applications such as sensing, imaging, and optoelectronics [43]. Moreover, Zheng *et al*. reported the fully NHC-protected Au_{25} nanocluster displays outstanding thermal and air stability in solution, which is notably superior to that of thiolated Au_{25} clusters [48].

Despite the successes in the crystallization of metal nanoclusters, there is a risk of missing crucial information about the presence of different low-energy structural isomers. This raises the question of whether the crystallized structure is the only stable form in the experimental setting, as many metal nanoclusters have a tendency to decompose over time under different environmental influences [49, 50, 51]. As a result of these structural changes, different chemical species can coexist, especially in the solution phase, which can interfere with the process of crystallization. This query has been the subject of investigation in several published studies [52, 53], which have demonstrated that the physicochemical properties of metal nanoclusters are significantly influenced by the presence of various isomers, thereby affecting the process of crystallization of the nanoclusters. Thus, the study of isomerism of metal nanoclusters can lead to the discovery of previously unknown clusters or the identification of clusters with unique characteristics that can have significant implications in various fields [54].

As stated earlier, metal nanoclusters fill the gap between metal atoms and plasmonic nanoparticles. They possess precise monodispersed sizes and well-defined structures that facilitate the examination at the atomic level. Furthermore, the discrete electronic states allow for the comprehensive investigation of nanocluster isomers through the examination of various physicochemical properties. These characteristics offer a potential pathway for the atomic-scale investigation of isomerism.

To this end, theoretical calculations can offer valuable insights by exploring both

electronic and structural properties. Previous studies have demonstrated the efficacy of density functional theory (DFT) to study the isomerism of gold nanoclusters [55, 56]. Nevertheless, depending on the scale of the system or the purpose of the calculations, investigating isomers using DFT can be hindered by intrinsic constraints such as computational cost and a lack of requirement for analyzing temperature-dependent characteristics. The molecular dynamics simulation method has been proven to be successful for this purpose [57, 58].

This thesis first investigates the effects of different ligands on the properties of metal-ligand (M-L) bonding in various M-L complexes and ligand-protected metal nanoclusters presented in the manuscript [PI]. Our results are in accordance with the findings presented in the study conducted by Crudden *et al*. [59], which highlights the exceptional potential of NHCs to form stable bonds with metals. The emphasis then shifts to NHC-protected metal nanoclusters, where the electronic and optical characteristics of two distinct Au nanoclusters are thoroughly examined in publications [PII] and [PIII], respectively.

In the publication [PIV], we employed DFT-based molecular dynamics simulations (DFT-MD) to gain insights into the atomic-scale behavior of the $[Au_6(NHC\text{-}S)_4]^{2+}$ nanocluster and explore its potential isomers under varying temperatures. Our study has revealed the presence of at least seven potential isomers at different temperatures. We found that the unique structure of each isomer can have a major influence on its optical and electronic properties, emphasizing the importance of comprehending isomerism in protected metal clusters in order to use them for specific applications. Furthermore, our findings suggest that the crystallized structure of a cluster may not always correspond to its lowest energy isomer in the gas phase, and the opposite may also be true.

The following is how this thesis is organized: In chapter 2, I discuss the computational methodology employed in my work. In chapter 3, I discuss the findings of the manuscript [PI] and articles [PII]-[PIV]. Lastly, in chapter 4, I summarize the main insights of this thesis and discuss potential future research directions.

2 COMPUTATIONAL METHODOLOGY

This section provides an overview of the concepts required to comprehend the theoretical foundations upon which the computational tools relied. I will begin by introducing density functional theory (DFT) used in all calculations carried out. Furthermore, I will describe the real-space code package GPAW (Grid-based projector-augmented wave method) which has been used for all the calculations presented in this thesis. The molecular dynamics simulation conducted in paper [PIV] will next be explained. In closing, a variety of analytical techniques, including Bader charge, dipole transition contribution maps, and analysis of electron states will be presented.

2.1 Density functional theory

DFT is a quantum mechanical approach that provides solutions to the Schrödinger equation to find the ground state properties of many-body systems fully defined by electron density which is dependent on 3 spatial coordinates, rather than using a many-body wave function Ψ, a function of $3N$ variables. To introduce DFT, we start with the Born-Oppenheimer approximation, which allows us to isolate electron motion from nuclei, which simplifies solving the many-body Scrödinger equation as nuclei are assumed to be stationary. Thus the time-independent Schrödinger equation for electrons interacting in a fixed external potential $\widehat{V}_{ext}$ using atomic units can be stated as:

$$\widehat{H}\Psi = (\widehat{T} + \widehat{V}_{ext} + \widehat{W})\Psi = E\Psi, \tag{2.1}$$

where the total energy E is the eigenvalue of the Hamiltonian operator $\widehat{H}$, Ψ is the ground state wave function, $\widehat{T}$ is the kinetic energy operator, and $\widehat{W}$ represents the

electron-electron interaction.

In 1964, Hohenberg and Kohn established the groundwork for density functional theory by introducing two theorems [60]. First, the theorem states that the ground state electronic density of a system determines the external potential $V_{ext}[n]$, and that by solving the Schrödinger equation with this $V_{ext}[n]$, the many-body wavefunction and thus the true ground state electron density of the system can be determined. The second theorem shows that by constructing a universal functional $F[n]$ that is independent of the external potential, the ground state energy $E[n]$ in an N-electron system can be calculated as:

$$E[n] = T[n] + V_{ext}[n] + W[n] = \int n(\boldsymbol{r}) v_{ext}(\boldsymbol{r}) dr + F[n], \tag{2.2}$$

$$F[n] = T[n] + W[n], \tag{2.3}$$

where $\int n(\boldsymbol{r}) v_{ext}(\boldsymbol{r}) dr$, is a system-dependent term and includes the electron-nuclei interactions in the system, $F[n]$ is the Hohnberg-Kohn (HK) functional known as universal functional that yields the ground state energy of the system if and only if the used density is the true $n_0(\boldsymbol{r})$.

Although the HK theorem is accurate, the difficulties to solve HK equations arise from the unknown universal functional. In 1965, Kohn and Sham (KS) proposed a technique [61] to solve the $F[n]$ using a non-interacting N particle system in which the real system is turned into an alternative non-interacting reference system in which electrons travel in an effective one-particle potential in atomic units :

$$F[n] = T_s[n] + V_H[n] + E_{xc}[n], \tag{2.4}$$

$$T_s[n] = \sum_{i=1}^{N} \langle \psi_i \mid -\frac{1}{2}\nabla^2 \mid \psi_i \rangle, \tag{2.5}$$

$$V_H[n] = \frac{1}{2} \int \int d\boldsymbol{r} d\boldsymbol{r'} \frac{n(\boldsymbol{r}) n(\boldsymbol{r'})}{\mid \boldsymbol{r} - \boldsymbol{r} \mid}, \tag{2.6}$$

$$E_{xc}[n] = (T - T_s) + (W - V_H). \tag{2.7}$$

$T_s[n]$ is the kinetic energy of non-interacting particles, $V_H[n]$ is the Hartree energy, which describes the classical Coulomb energy and contains the energy of electron cloud, and $E_{xc}[n]$ is the exchange-correlation (xc) functional, which treats the ground-state density inaccuracies caused by the independent-particle approximation, as discussed in more detail in the next subchapter. Since now we have a better understanding of the universal functional, let us check the one-particle KS equations:

$$(-\frac{1}{2}\nabla^2 + v_{eff}(\boldsymbol{r}))\phi_i(\boldsymbol{r}) = \varepsilon_i \phi_i(\boldsymbol{r}), \tag{2.8}$$

where ε_i represents the eigenenergies, $\phi_i(\boldsymbol{r})$ is KS orbitals representing non-interacting electrons wavefunctions from which the exact ground state electron density of

the interacting system can be calculated. According to the Kohn-Sham theorem, we are seeking the ground state electron density of the interacting system $n_0(\boldsymbol{r}) = \sum_{i=1}^{N} |\phi_i(\boldsymbol{r})|^2$. As such, $v_{eff}(\boldsymbol{r})$ used in equation 2.8 is an effective potential that the individual particles observe, and therefore generates the density of the interacting system. This potential can be defined as:

$$v_{eff}[n] = v_0(\boldsymbol{r}) + v_H + v_{xc}, \tag{2.9}$$

$$v_{xc}[n](\boldsymbol{r}) = \frac{\delta E_{xc}}{\delta n(\boldsymbol{r})}, \tag{2.10}$$

where v_0 is a system-dependent external potential created by the nuclei. However, v_H is the classical Coulomb energy of the electrons cloud, and v_{xc} is the exchange-correlation potential which is defined as equation 2.10.

Starting with a guess for an initial electron density and using a chosen approximation for v_{xc}, the effective single particle KS potential can be calculated using equation 2.10. The KS equations are then solved by using the calculated potential. By applying $n_0(\boldsymbol{r}) = \sum_{i=1}^{N} |\phi_i(\boldsymbol{r})|^2$, a new electron density will be derived from the calculated eigenstates. The calculated density generates a new effective potential, which is input into the KS equations, creating new eigenstates and a new density. This iteration is continued until the density and effective potential are self-consistent. The self-consistency can be detected, *e.g.*, when the difference between the two most recent estimated densities is smaller than a pre-defined threshold.

2.1.1 Exchange-correlation functionals

Exchange-correlation (xc) functional is a crucial component of the Kohn-Sham equation, which portrays many-body effects in a quantum system. Exchange and correlation energies represent different interactions in a system, as exchange interaction occurs between electrons with the same spin; however, the correlation term is caused by the difference in energy between the exact energy of the true interacting system and the energy of the non-interacting KS system. The challenging part in DFT is to introduce a reasonable estimate for E_{xc}, which in its exact form would require the complete solution of the full many-body problem, yet unachievable. Various approximations based on known physical limits of electron gas are applied to calculate the exchange-correlation energy. Among all, generalized gradient approximation (GGA) is the approach used in this thesis. In this approximation, the functional depends on both electron density (n) and the gradient of electron density $\nabla n(\boldsymbol{r})$, which reveals how the density of electrons in a system varies with distance. This approach opens up the possibility that non-local electron effects can be evaluated due to the fact that the distribution of electron

density in a real system is not necessarily uniform. The following defines the xc energy functional based on GGA:

$$E_{\mathrm{xc}}^{\mathrm{GGA}}[n] = \int f^{\mathrm{GGA}}(n(\boldsymbol{r}), \nabla n(\boldsymbol{r}))d\boldsymbol{r}, \tag{2.11}$$

where $f^{\mathrm{GGA}}(n(\boldsymbol{r}), \nabla n(\boldsymbol{r}))$ is the GGA functional, which depends on both the electron density $n(\boldsymbol{r})$ and its gradient $\nabla n(\boldsymbol{r})$ at each point in space $\boldsymbol{r}$. There are several GGA functionals, such as PBE [62], GLLB-SC [63], and BEEF-vdW [64] Which are used in this thesis. Each of these functionals has a unique functional form of f^{GGA} which is determined by combining different approximations for the exchange and correlation parts.

All ground state calculations provided in this thesis used the PBE functional established by Perdew, Burke, and Ernzerhof [62], which is defined as:

$$E_{xc}^{PBE} = \epsilon_x^{hom} F(x) + \epsilon_c^{hom} + H(t), \tag{2.12}$$

in which the increment factor to the exchange (${\epsilon_x}^{hom}$) and correlation (${\epsilon_c}^{hom}$) energy of the homogeneous electron gas is given by the enhancement factor for the exchange energy $F(x)$, and the enhancement factor to the correlation energy $H(t)$.

Another functional that has been used in this thesis is GLLB-SC which is originally developed with the aim of providing calculations to accurately predict the band gaps of semiconductor and dielectric materials [65]. This functional is based on the GLLB-type exchange[66] and PBEsol correlation [67]. Notably, two independent studies have demonstrated the effectiveness of GLLB-SC in improving the accuracy of band gap values and in providing better agreement with experimental results. One of the studies [68] analyzed the band gap of a diverse set of 76 solids, including sp semiconductors, ionic insulators, rare gases, and strongly correlated solids. The study revealed that the accuracy of GLLB-SC is substantially superior to that of both LDA [69] and GGA methods and is comparable to that of hybrid functionals. In another study [70], it was determined that the band gap of phosphorene was elevated upon adsorption of boron nitride.

Moreover, to include the van der Waals interactions in our DFT calculations for the manuscript [PI], the BEEF-vdW (Bayesian Error Estimation Functional with van der Waals) functional was employed [64]. The BEEF-vdW incorporates numerous functionals to correctly explain and characterize a wide variety of atom-atom interactions, including covalent, metallic, and long-range interactions which are often not well-described by simpler functionals. BEEF-vdW is composed of an exchange energy term, which is comparable to the PBE functional, and a correlation energy term that combines elements of the LDA [69] and PBE [62]

functionals with a functional called vdW-DF2 [71], which was specifically designed to describe the vdW interactions.

In systems with an odd number of electrons such as some metal-ligand complexes studied in the manuscript [PI], it was essential to include the spin of the electrons; thus, using spin-polarized density functional theory (SP-DFT) allows the Kohn-Sham equations to be solved for each spin separately and includes a spin-dependent exchange-correlation potential in the calculations. The total electron density is separated into spin-up and spin-down electron densities, and the Kohn-Sham equations are solved independently for each of them. The total electron density is given by the sum of the spin-up and spin-down electron densities.

2.1.2 Linear response time-dependent density functional theory

As previously stated, for a stationary system DFT relies on the ground state electron density; however, to extend DFT to the time domain for excited systems, a time variable must be introduced which necessitates employing the time-dependent (TD) Schrödinger equation:

$$i\frac{\partial}{\partial t}\Psi(\mathbf{r_i},t) = \hat{H}(\mathbf{r_i},t)\Psi\left(\mathbf{r}_i,t\right), \tag{2.13}$$

where Ψ, the many-body electronic wave function, and the Hamiltonian operator ($\hat{H}$) depend not only on the position of all electrons $\mathbf{r}_i (i = 1, 2, ..., N)$ but also on time. As DFT for the static systems, the TDDFT relies on electron density with 4 variables to minimize the complexity of working with $3N + 1$ variables for the many-body wave function. The time-dependent electron density is given as:

$$n\left(\mathbf{r},t\right) = N\int |\Psi(\mathbf{r},\mathbf{r_2},...,\mathbf{r_N},t)|^2 d\mathbf{r_2}...d\mathbf{r_N}. \tag{2.14}$$

In a seminal work [72], it was demonstrated that for any interacting particle system, a one-to-one correspondence exists between the time-dependent electron density and the time-dependent external potential. This correspondence allows for an expansion in a Taylor series with respect to time, providing a foundation for understanding the response of the system to perturbations in the external potential.

For systems with weak external perturbation, the Taylor series expansion is only evaluated in the first order, yielding the linear response. In this thesis, the optical properties of gold nanoclusters were studied using linear response TDDFT (LR-TDDFT) employing Casida's formalism. Casida's equation represents an eigenvalue problem, as illustrated in equation 2.15. This equation is solved in the frequency domain, with the time variable, t, being transformed into the frequency variable, ω, through the application of the Fourier transformation [73, 74].

The eigenvalue problem involving the matrix Ω is solved as follows:

$$\Omega F = \omega_I^2 F. \tag{2.15}$$

Equation 2.16 provides the matrix elements of Ω:

$$\Omega_{ij,kl} = \delta_{i,k}\delta_{j,l}\left(\epsilon_l - \epsilon_k\right)^2 + 2\sqrt{\left(f_i - f_j\right)\left(\epsilon_j - \epsilon_i\right)}K_{ij,kl}\sqrt{\left(f_k - f_l\right)\left(\epsilon_l - \epsilon_k\right)}. \tag{2.16}$$

The subscripts i, j and k, l label the occupied and unoccupied Kohn-Sham states, respectively, and ϵ and f refer to the energy and the occupation numbers of occupied and unoccupied states. The coupling matrix $K_{ij,kl}$ consists of the Hartree and exchange-correlation parts given as:

$$K_{ij,kl} = \int \mathrm{d}\mathbf{r}\mathrm{d}\mathbf{r}'\phi_i^*(\mathbf{r})\phi_j(\mathbf{r})\left[\frac{1}{|\mathbf{r}-\mathbf{r}'|} + \frac{\delta^2 E_{\mathrm{xc}}[n]}{\delta n^2}\right]\phi_k(\mathbf{r}')\phi_l^*(\mathbf{r}'). \tag{2.17}$$

The solution of Casida's equations requires the calculation of the wave functions and energies of the ground state system, and the KS wave functions are natural choices as the basis functions.

2.2 Molecular dynamics simulations

In this dissertation, I present an investigation of potential isomers for a ligand-protected gold nanocluster via molecular dynamics (MD) simulations [75, 76]. The interatomic forces within the system are calculated using DFT. MD simulation is a computer-based method that sheds light on the dynamical behavior of a system, which is useful to explain in detail the experimental results that show usually the effects of dynamics for example in form of absorption or NMR spectra.

To perform MD simulations, it is necessary to define an ensemble for a system, which specifies the conditions under which the simulation is performed. One commonly used ensemble is the canonical ensemble (NVT) which is used in this thesis, in which the number of particles (N), volume (V), and temperature (T) of the system are held constant, but the energy is allowed to fluctuate. This serves as a model of the system that is in contact with a heat bath.

In MD simulations, increasing the temperature entails the addition of kinetic energy to the system, leading to atom displacements and velocities. In this context, the MD algorithms are responsible for updating the positions and velocities of the atoms at each time step, whereas underlying atomic interactions are given by DFT. In order to forecast how a set of atoms or molecules evolves over the course

of time, the solution of Newton's equations of motion $F = ma$ for the system is required. The total force acting on an atom can be calculated by taking the negative gradient of the potential energy of the system V with respect to the position of atom i as:

$$-\nabla_i V = m_i \frac{d^2 \mathbf{r}_i}{dt^2}. \tag{2.18}$$

The velocity Verlet algorithm as described below is a widely used method for integrating the positions and velocities of atoms in molecular dynamics simulations. The basic idea behind the velocity Verlet algorithm is to split the update of positions and velocities into two separate steps, allowing for a more accurate and stable calculation of trajectories. Here are the steps of the algorithm (Δt is the simulation time step):

1- Current forces $F(t)$ acting on the atoms using their current positions $r(t)$ are calculated.

2- The positions $r(t + \Delta t)$ using the current velocities $v(t)$ and the calculated forces $F(t)$ are updated as:

$$F(t) = r(t + \Delta t) = r(t) + v(t)\Delta t + \frac{(1/2)F(t)(\Delta t)^2}{m}.$$

3- The intermediate velocities $v(t + \frac{\Delta t}{2})$ are calculated as:

$$v(t + \frac{\Delta t}{2}) = v(t) + \frac{(1/2)F(t)\Delta t}{m}.$$

4- The new forces $F(t + \Delta t)$ using the updated positions $r(t + \Delta t)$ are calculated.

5- The velocities $v(t + \Delta t)$ are updated by using the intermediate velocities $v(t + \frac{\Delta t}{2})$ and the new forces $F(t + \Delta t)$ as:

$$v(t + \Delta t) = v(t + \frac{\Delta t}{2}) + \frac{(1/2)F(t + \Delta t)\Delta t}{m}.$$

6- Steps 1-5 for each time step in the simulation are repeated until one of the following stopping criteria is met: convergence of specific system properties, reaching the predetermined total simulation time, or completing the predefined number of time steps.

As the simulations in this thesis were run under NVT conditions, a thermostat is required to maintain a consistent temperature. The thermostat is a computational algorithm that is used to eliminate surplus energy and maintain the desired temperature of the system by modifying the Newtonian equations of the motion

that govern the movement of the particles. One common thermostat that is used in MD simulations is the Langevin thermostat [77]. The Langevin equation for an atom with mass m_i is given by:

$$F = -\frac{dV}{dr} - \gamma m_i \dot{r}_i + R_i(t). \tag{2.19}$$

Here, F is the total force acting on atoms, and $\dot{r}_i$ represents the time derivative of the position r_i of the ith particle. γ is damping constant (the Langevin friction coefficient), and R_i(t) is the Gaussian stochastic variable. The Gaussian stochastic variable $(R_i(t))$ represents the random force on a particle due to collisions with the heat bath particles at every given step, introducing thermal fluctuations into the system. The damping constant (γ) controls the coupling strength between the particle and the heat bath, affecting the system's equilibrium rate. Together, the friction term and the random force ensure the system reaches the desired temperature while maintaining the correct dynamics.

2.3 GPAW: Real-space grid implementation

GPAW (Grid-based Projector Augmented Wave) method [78, 79] is a real space grid-based implementation of the projector-augmented wave (PAW) method [80] which can be performed for a variety of systems, including nanostructures, surfaces, and interfaces to study a wide range of physical phenomena including structural optimization, electronic properties, vibrational and optical spectra, as well as molecular dynamics simulations. GPAW is a free and open-source software package is designed to be highly modular and flexible, allowing users to perform a wide range of calculations using different exchange-correlation functionals, boundary conditions, and other simulation parameters.

In addition to the capabilities of GPAW to perform DFT calculations, the atomic simulation environment (ASE) [81] as a set of Python libraries is designed to provide a unified interface for atomistic simulations and allows for the efficient and accurate calculation of physical properties. ASE provides the tools required to set up and conduct computations using the GPAW algorithm, including the generation of input files, calculation execution, and result post-processing. Furthermore, ASE includes a variety of tools for evaluating and visualizing the results of GPAW calculations.

GPAW bases its electronic structure computations on the PAW approach, which generates localized, atom-like orbitals that can be used to depict the electronic structure of a system. These orbitals are created by perturbing the wave functions

of the valence electrons in a system while accounting for the effect of the core electrons. The all-electron wave function (Ψ_n) is calculated as a product of the linear transformation using a projection operator ($\hat{T}$) on pseudo wave functions ($\tilde{\Psi}_n$), as shown in equation 2.23:

$$|\Psi_n\rangle = \hat{T}\left|\tilde{\Psi}_n\right\rangle, \tag{2.20}$$

the transformation between all-electron wave functions and pseudo-wave functions is restricted to a specific region around each atom (the augmentation sphere). According to equation 2.24, the transformation operator $\hat{T}$ is then formulated through the partial waves ($\phi_i{}^a$), the smooth partial waves $\tilde{\phi}_i^a$, and projector functions p_i^a. The transformation between all-electron and pseudo-wave functions in the GPAW method allows for a more efficient and accurate description of the electronic structure of a system, particularly for systems with a large number of valence electrons.

$$\hat{T} = 1 + \sum_a \sum_i \left(|\phi_i^a\rangle - |\tilde{\phi}_i^a\rangle\right)\langle p_i^a|\,. \tag{2.21}$$

Applying this method along with the real-space grid introduces an efficient representation of the wave functions for the system, efficient calculation of matrix elements required for the DFT calculations, and efficient parallelization of the calculations.

The atomic PAW setups for all Group-11 metals studied in this work include the scalar-relativistic corrections.

2.4 Analysis methods

2.4.1 Bader charge analysis

The local atomic charges in this thesis are determined using Bader charge analysis [82, 83, 84, 85], a technique for evaluating the charge distribution within a molecule or solid.

To perform Bader charge analysis, the all-electron density calculated by DFT was used as input. The analysis works by iteratively examining each grid point around the system and assigning it to a specific atom based on its electron density gradient behavior. This is done by following the deepest ascent path until the maximum density is found, which represents the position of the assigned atom. Once all grid points have been assigned, the Bader volumes of each atom can be defined, and the all-electron density can be integrated into these restricted volumes to

determine the number of electrons assigned to each atom. From this information, the local atomic charge can be determined.

2.4.2 Dipole transition contribution maps

A dipole transition contribution map (DTCM) [86] is a graphical representation of the contributions to the transition dipole moment of a system that is used in this thesis to investigate the origin of peaks in the absorption spectrum employing time-dependent density functional perturbation theory (TD-DFPT) [87] as implemented in GPAW.

All the transitions from the initial electron state α to the final unoccupied states β that contribute to the studied excitation at frequency ω can be accounted for by calculating the absorption coefficients $C^{\omega}_{\alpha\beta}$ using this approach. The DTCM is plotted as a two-dimensional map, with the energy of occupied states ($\varepsilon_{\mathrm{occ}}$) on the x-axis and the energy of unoccupied states ($\varepsilon_{\mathrm{unocc}}$) on the y-axis. The transitions are depicted as dots on the plot, and the density of the contour lines indicates the intensity of each contribution. The transitions over the two axes are presented by using Gaussian broadening. The DTCM is calculated using the following equation:

$$\mathrm{DTCM}\left(\varepsilon_{\mathrm{occ}}, \varepsilon_{\mathrm{unocc}}\right) = \sum_{\alpha}^{\mathrm{occ}} \sum_{\beta}^{\mathrm{unocc}} 2C^{\omega}_{\alpha\beta}\omega\mu_{\alpha\beta} \exp\left[-\left(\frac{\varepsilon_{\mathrm{occ}} - \varepsilon_{\alpha}}{\Delta\varepsilon}\right)^2 - \left(\frac{\varepsilon_{\mathrm{unocc}} - \varepsilon_{\beta}}{\Delta\varepsilon}\right)^2\right], \tag{2.22}$$

for the transition $\alpha \rightarrow \beta$ along the direction of the laser field, the dipole moment is indicated by $\mu_{\alpha\beta}$, and ω is the frequency of the excitation. The DTCM is typically visualized using a color map, with positive contributions shown in red and negative contributions shown in blue.

2.4.3 Angular momentum analysis of Kohn-Sham orbitals

In this thesis, the projected density of states (PDOS) analysis [8] was employed to describe the superatomic feature of the studied clusters. PDOS allows for the classification of orbital states within a cluster, including those that are delocalized throughout the entire cluster core, known as superatomic orbitals. The symmetries of each state are determined by introducing coefficients for the system as:

$$c_l(R_0) = \sum_m \int_0^{R_0} r^2 dr |\Psi_{nlm}(r)|^2, \tag{2.23}$$

where R_0 is the radius of the cluster region, which is manually specified to encompass the whole cluster. Using Kohn-Sham eigenfunctions ($\psi_n(\boldsymbol{r})$) projected onto spherical harmonics functions ($Y_{lm}(\boldsymbol{r})$) with respect to the center of the cluster, $\Psi_{nlm}(\boldsymbol{r})$ can be written as:

$$\Psi_{nlm}(r) = \int dr Y_{lm}(\hat{\boldsymbol{r}})^* \psi_n(\boldsymbol{r}). \tag{2.24}$$

In this approach, the projection weights (overlaps of each state) onto spherical harmonics functions with varying angular momenta are calculated. The magnetic quantum number, m establishes the spatial orientation of the orbitals, whereas l as an angular quantum number signifies the overall symmetry of functions. Finally, the Gaussian broadened PDOS can be used to visualize the goodness of the match of each KS state into different superatom state symmetries at different quantum numbers l that are usually distinguished by colors.

3 RESULTS AND DISCUSSION

In this section, I will discuss the implications and importance of the results presented in the manuscript [PI] and the publications [PII]-[PIV]. I will begin by delving into the role of ligands in bonding to different metal atoms as reported in the manuscript [PI] to broaden our understanding of metal-ligand (M-L) bond properties from small M-L complexes to bigger systems such as ligand-protected metal nanoclusters. The explanations provided in this thesis contribute to a comprehension of the reason why NHCs, rather than thiolates or phosphines, emerge as superior ligand candidates in the aforementioned studied systems. This finding is consistent with a study published by Crudden *et al* [59], in which they explain the argument for using NHCs instead of thiolates as ligands in the formation of self-assembled monolayers (SAMs) on gold surfaces. They found that the NHC SAMs display exceptional stability, withstanding severe conditions such as high temperatures, high pressure, and solvent exposure without significant deterioration or detachment from the gold surface. This stability is attributed to the strong covalent bonds formed between the NHCs and the gold surface compared to thiolates.

Following that, I focus my attention on the ligand-protected Au nanoclusters. Thus, in paper [PII], the physicochemical properties of $Au_{10}(NHC)_6Br_3]^+$, a novel 6-electron superatom cluster protected by NHC were studied. Moreover, the study of the electronic and optical properties of the non-superatom di-cation cluster protected by mixed NHC-S ligands $[Au_6(^{iPr}BnIm\text{-}C_2H_4\text{-}(\mu_3\text{-}S)_4]^{2+}$ ($[Au_6(NHC\text{-}S)_4]^{2+}$) is presented in article [PIII]. Lastly, in paper [PIV] by employing DFT-MD simulations the stability of crystallized $[Au_6(NHC\text{-}S)_4]^{2+}$ nanocluster is questioned by exploring possible isomers and comparing their stabilities. The findings suggest that crystallized structure is not necessarily the most stable configuration in the gas phase along with highlighting the importance of studying isomerization in metal nanoclusters.

3.1 Role of ligands in metal-ligand bond properties

In the manuscript [PI], a detailed investigation of the bonding interactions between ligands and metal atoms is presented for metal complexes and $[M_{13}L_6Br_6]^-$ clusters. The M-L complexes are composed of selected group-11 metal atoms (M = Cu, Ag, Au) bonding to various ligands (L= SCH_3, SC_8H_9, PPh_3, NHC^{Me}, NHC^{Et}, NHC^{iPr}, NHC^{Bn}) as are depicted in figure 3.1. Moreover, the clusters were constructed using the same group-11 metals and with L = PPh_3 and NHC. Figure 3.1 illustrates the PBE-optimized Au-L complexes and Au nanoclusters protected by NHC^{Me} and PPh_3, which serve as representative examples of the other systems examined in the study. Two functionals PBE and BEEF-vdW were used to study the effects of van der Waals interactions on the geometrical properties of the aforementioned systems. The electronic properties, however, were presented only for the PBE functional.

The chemical bonding of Group-11 coinage metals involves s and d valence orbitals, characterized by a fully occupied d shell and a singly occupied s shell in the form of nd^{10} $(n + 1)s^1$, where n=3, 4, and 5 correspond to Cu, Ag, and Au, respectively. The highest s-band of Group-11 atoms exhibits electron dispersion similar to that of alkali metals; however, unlike alkali metals, relativistic effects must be taken into account to accurately describe the properties of systems containing elements with a filled underlying d shell[88, 89, 90, 91, 92, 93, 94, 95, 96, 42].

The bond length comparison displayed in figure 3.2 reveals the sequence of M-L complexes to be Ag-L > Au-L > Cu-L for both PBE and BEEF-vdW. It was observed that BEEF-vdW resulted in slightly longer bond lengths, ranging from 0.04 to 0.14 Å when compared to the PBE. The smaller energy gap between the 3d and 4s orbitals in copper, compared to silver leads to increased involvement of both 3d and 4s orbitals in bond formation [97]. As a result, there is a higher degree of covalency and stronger bonds within copper compounds than silver counterparts.

The binding energies for the M-L complexes were calculated as follows: ΔE = (E[H_2]/2+E[M-SR]) - (E[M] + E[HSR]) for thiolates and ΔE = E[M-L] - (E[M]+E[L]) for phosphines and carbenes. In the case of phosphine- and carbene-protected metal clusters, the binding energy was determined using the formula: ΔE = $[E[M_{13}L_6Br_6]^-$ - $(E([M_{13}Br_6]^-$ + 6*L)]/6. The findings show that the binding energies are proportional to the bond lengths. Nevertheless, the gold complexes bonded to electron-donating ligands, such as PPh_3 and NHCs, exhibit higher binding energies compared to their copper counterparts. This occurrence can be attributed to the relativistic effects observed in gold atoms, which significantly influence their electronic properties and bonding behavior. Figure 3.2 reveals that the most and least stable compounds identified in the analysis are consistent between the PBE and BEEF-vdW calculations, exhibiting the same relative order

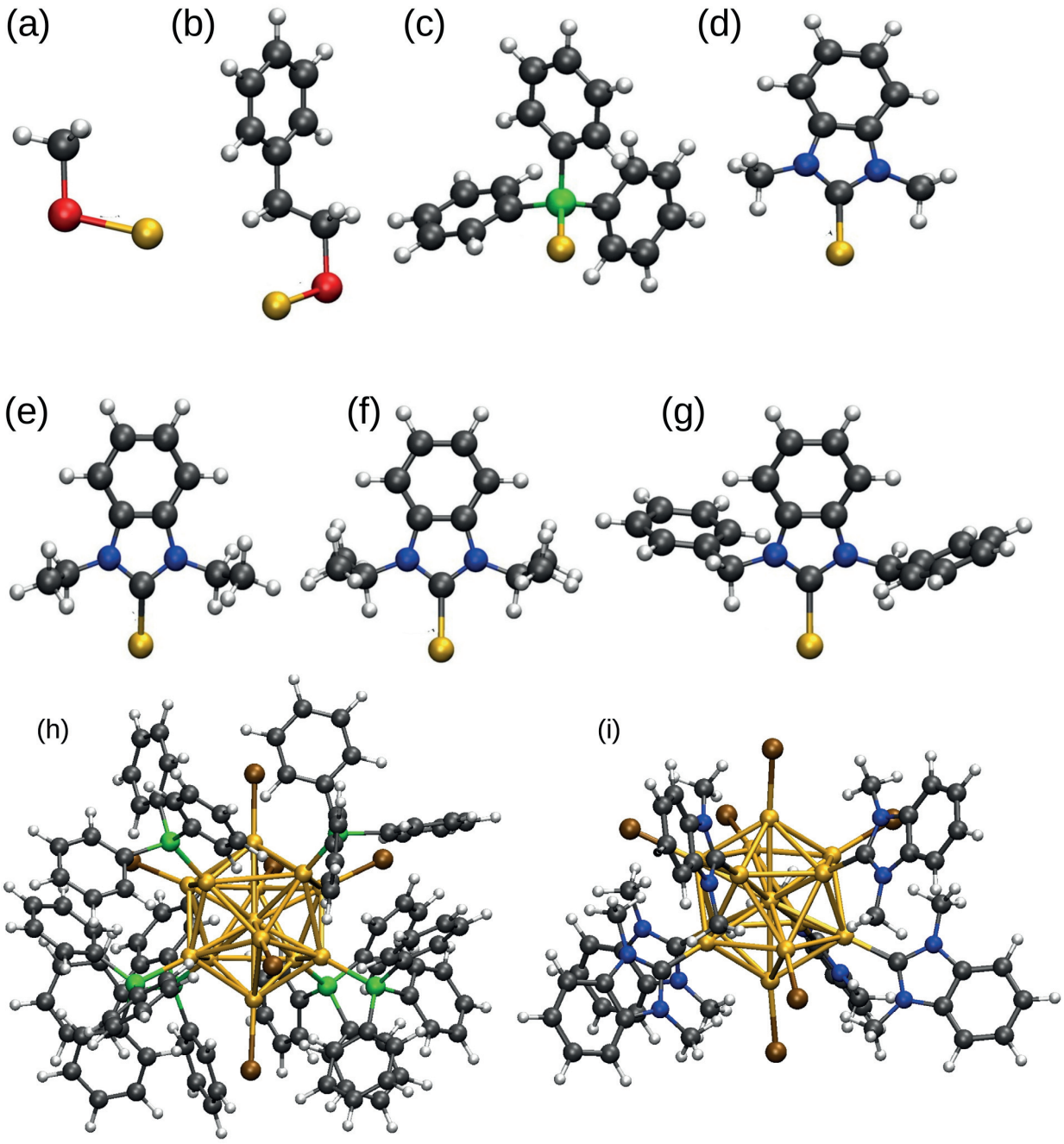

FIGURE 3.1 PBE optimized Au-L complexes for (a) Au-SCH_3, (b) Au-SC_8H_9, (c) Au-PPh_3, (d) Au-NHC^{Me}, (e) Au-NHC^{Et}, (f) Au-NHC^{iPr}, (g) Au-NHC^{Bn} along with two ligand protected Au clusters displayed in (h) $[Au_{13}(PPh_3)_6Br_6]^-$ and (i) $[Au_{13}(NHC^{Me})_6Br_6]^-$. Notice the atom radius depicted in the figure is not precisely reported. The color code for the different atoms is as follows: Au (yellow), S (red), C (black), H (white), P (green), N (blue), and Br (brown).

of energy values for these structures. The debate over the varied characteristics in group-11 elements despite similar valence electron configurations is explained by these effects which become more significant as the number of electrons increases from Cu to Au [98, 99, 100]. The relativistic effects in gold result in the expansion of the 5d orbitals (5d > 4d > 3d), consequently reducing the energy gap between the 5d and 6s orbitals in gold atom[101, 102, 103]. Moreover, the contraction of the outer s- and p-orbitals in gold results in decreased atomic size compared to when these effects are disregarded.

This constriction in Au explains the higher electron affinity compared to Cu and Ag (Au: 2.3 eV, Ag: 1.2 eV, Cu: 1.22 eV) [104]. The higher electron affinity suggests that gold is more inclined to attract electrons, resulting in a more stable and energetically favorable form of bonds with electron-donating ligands.

Additionally, a study conducted by Muñoz et al. [105] reported the influence of relativistic effects on the stabilization of dative carbon-metal bonds in coinage metal complexes, exemplified by NHC-MCl species (M = Cu, Ag, Au). Through a comparison of scalar relativistic and non-relativistic DFT calculations, they determined the extent to which relativistic effects contribute to various aspects of bond formation. They observed an increasing impact of relativistic effects from Cu (7.9%) to Ag (15.3%) and most notably for Au (39.9%). Relativistic effects contribute to the stabilization of interaction energy components, accentuating the reinforcement of σ-$PPh_3 \rightarrow$ M and σ-NHC $\rightarrow$ M bonds, as well as their electrostatic nature. This observation is analogous to the effect of ligands possessing different σ-donor capacities, implying that relativistic effects should be accounted for when assessing dative carbon-metal bonds, even in the case of lighter group elements.

Comparing different ligands, it was found that NHCs have higher ligand-metal bond strengths. This finding is aligned with the finding of a study [59] which explains that thiolate SAMs on the Au surface were replaced by NHCs due to the superior stability of carbene ligands. This stability can be attributed to the nature of metal-ligand bonds which is discussed more in detail in this work. Overall, this evidence supports the argument that NHCs can be a highly appealing choice as ligands in the field of nanometal clusters.

The electronic properties of M-L complexes (L = SCH_3, PPh_3, NHC^{Me}) were studied next. Figure 3.3 illustrates the PDOS of Cu-NHC^{Me} (a), Ag-NHC^{Me} (b), and Au-NHC^{Me} (c) for metal and carbon atoms, together with plotted occupied molecular orbitals (numbers 1 to 4 refer to HOMO to HOMO-3). Carbon atoms with the electronic configuration of $1s^2\ 2s^2\ 2p^2$ form a chemical bond with coinage metals having the electronic configuration of $nd^{10}(n+1)s^1$, which lead to the formation of an open-shell M-NHC complex. As shown in figure 3.3, the HOMO states in metal atoms which are primarily s-symmetric and ligand groups that have p-symmetry are responsible for the M-L bonding in Cu-C.

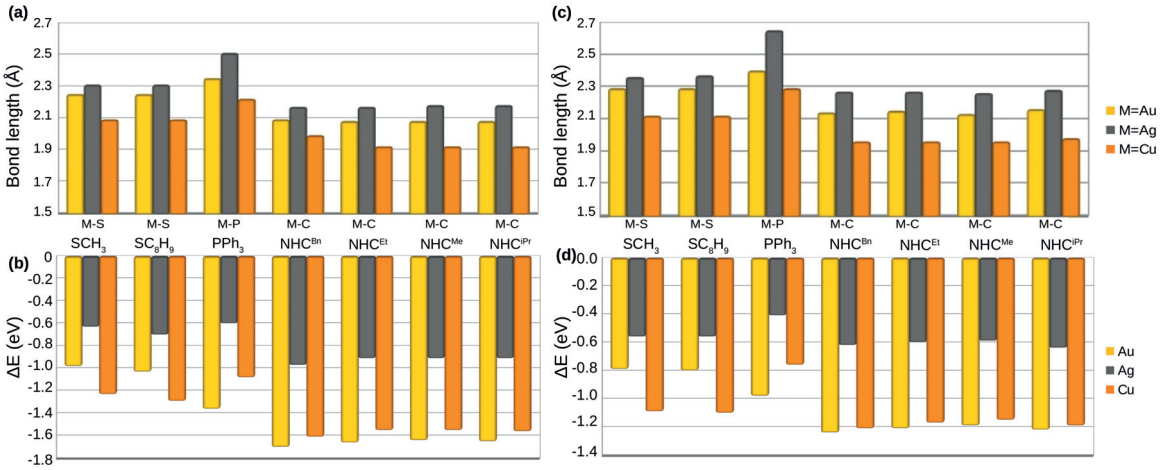

FIGURE 3.2 The M-L bond lengths (Å) and binding energies (eV) of the M-L complexes calculated with PBE in (a)-(b) and with BEEF-vdW in (c)-(d).

Additionally, d-states in Ag and Au atoms also interact with p-states of carbon atoms, resulting in additional bonding states at lower energy levels, such as the HOMO-1 and HOMO-2 states (labeled as 2 and 3). The σ-type bonding feature has been identified in M-NHC this means that the bonding between the metal atoms and C-atoms in these complexes is primarily due to the overlap of the atomic orbitals of metals and ligands, resulting in a strong covalent bond. The σ-type bonding feature is often associated with the stability of the complexes. Study on the frontier molecular orbitals associated with the bonding of coinage metals and SCH_3 has revealed that the M-SCH_3 complexes exhibit the σ-type bonding for their HOMO-1 states, as well as π-type bonding resulting from the coupling of d-states of the coinage metals and p-states of the sulfur atoms in lower energy states. This is in contrast to the σ-type bonding that has been observed in M-PPh_3 bonds. Moreover, Cu has been observed to have the shortest bond length when bonded to various ligands, this can be also attributed to its frontier atomic electron states being near the Fermi level.

Bader charge analysis for PBE-optimized M-L complexes indicates that the coinage metals exhibit different electron affinities when bonding to NHC ligands as compared to thiolates and PPh_3. The metal atoms transfer electrons to thiolates while withdrawing them from PPh_3 and NHC ligands. The examination of different NHC groups revealed that the size of R groups in NHCs, whether R is CH_3, C_2H_5, C_3H_7, or $CH_2C_6H_5$, does not significantly impact the electron affinity of coinage metals this conclusion is consistent with the findings for thiolate ligands, which indicate that the size of R groups has no significant impact on the electron donation behavior of metals however sulfur in SC_8H_9 has higher electronegativity comparing to SCH_3.

To explore larger systems, I focus my attention on protected metal nanoclusters as $[M_{13}L_6Br_6]^-$ (L= PPh_3, NHC^{Me}, NHC^{Et}, NHC^{iPr}, NHC^{Bn}, and M= Cu, Ag, Au).

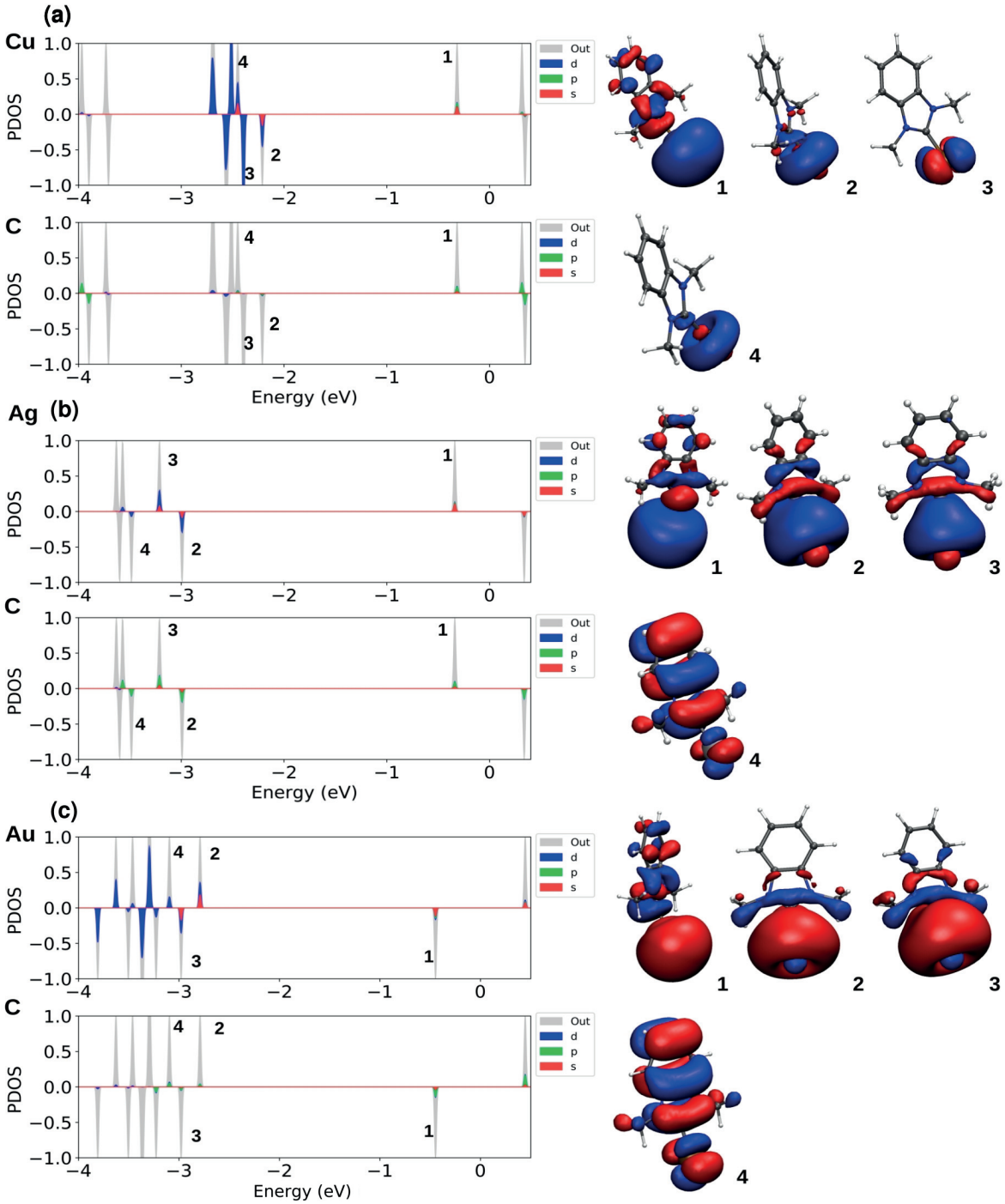

FIGURE 3.3 The occupied molecular orbitals, labeled with labeled from 1 to 4 denoting states from HOMO-2 to LUMO, and the projected density of states for three systems: (a) Cu-NHC^{Me} (b) Ag-NHC^{Me} and (c) Au-NHC^{Me}. The HOMO-LUMO gap is presented for each system, centered around zero and with values of 1.48 eV, 1.49 eV, and 1.41 eV for systems a to c, respectively.

TABLE 3.1 PBE and BEEF-vdW calculated binding energy per ligand (eV) and average M-L bond length (Å) for $[M_{13}L_6Br_6]^-$ clusters (L= PPh_3, NHC^{Me}, NHC^{Et}, NHC^{iPr}, NHC^{Bn}, and M= Cu, Ag, Au).

	PBE		BEEF-vdW	
M-L	ΔE	M-L Bond length	ΔE	M-L Bond length
$[Cu_{13}(PPh_3)_6Br_6]^-$	-0.75	2.34	-1.13	2.36
$[Ag_{13}(PPh_3)_6Br_6]^-$	-0.75	2.50	-1.04	2.55
$[Au_{13}(PPh_3)_6Br_6]^-$	-1.57	2.35	-1.41	2.39
$[Cu_{13}(NHC^{Me})_6Br_6]^-$	-1.67	2.00	-1.62	2.00
$[Ag_{13}(NHC^{Me})_6Br_6]^-$	-1.34	2.14	-1.21	2.21
$[Au_{13}(NHC^{Me})_6Br_6]^-$	-2.21	2.12	-1.58	2.09
$[Cu_{13}(NHC^{Et})_6Br_6]^-$	-1.59	1.96	-	-
$[Ag_{13}(NHC^{Et})_6Br_6]^-$	-1.32	2.16	-	-
$[Au_{13}(NHC^{Et})_6Br_6]^-$	-2.18	2.13	-	-
$[Cu_{13}(NHC^{iPr})_6Br_6]^-$	-1.51	1.96	-	-
$[Ag_{13}(NHC^{iPr})_6Br_6]^-$	-1.33	2.17	-	-
$[Au_{13}(NHC^{iPr})_6Br_6]^-$	-2.18	2.07	-	-
$[Cu_{13}(NHC^{Bn})_6Br_6]^-$	-1.52	1.97	-	-
$[Ag_{13}(NHC^{Bn})_6Br_6]^-$	-1.22	2.16	-	-
$[Au_{13}(NHC^{Bn})_6Br_6]^-$	-2.04	2.06	-	-

To do this, I utilized the experimental work carried out by Shen et al [106] in 2020 in which they synthesized anionic icosahedral gold clusters $[Au_{13}NHC_6Br_6]^-$ using three different types of NHCs. However, to the best of our knowledge, crystallized clusters in the form of $[M_{13}NHC_6Br_6]^-$ for M=Cu and Ag have not yet been identified.

Therefore, $[Au_{13}NHC_6Br_6]^-$ (NHC-1 = 1,3-diisopropylbenzimidazolin-2-ylidene) served as the starting point for the analysis, and the cluster by substituting various ligand groups and metal atoms was subsequently modified. The geometrical properties of $[M_{13}L_6Br_6]^-$ clusters (L= PPh_3, NHC^{Me}, NHC^{Et}, NHC^{iPr}, NHC^{Bn}, and M= Cu, Ag, Au) along with the electronic properties with a focus on the M-L bonds in coinage metal clusters protected by PPh_3 and NHC^{Me} ligands have been studied. As shown in table 3.1, the average M-L bond lengths for metal clusters estimated using both PBE and BEEF-vdW (the van der Waals interactions have just been investigated for the clusters protected by PPh_3 and NHC^{Me}) followed the same sequence as seen in M-L bond lengths for complexes, with Ag-L > Au-L > Cu-L.

The binding energy per ligand in gold clusters has been determined to be the highest among copper and silver clusters. On the other hand, copper clusters display the second-highest binding energy, and have the shortest average M-L bond lengths. Cu clusters protected by NHCs were found to be suitable candidates

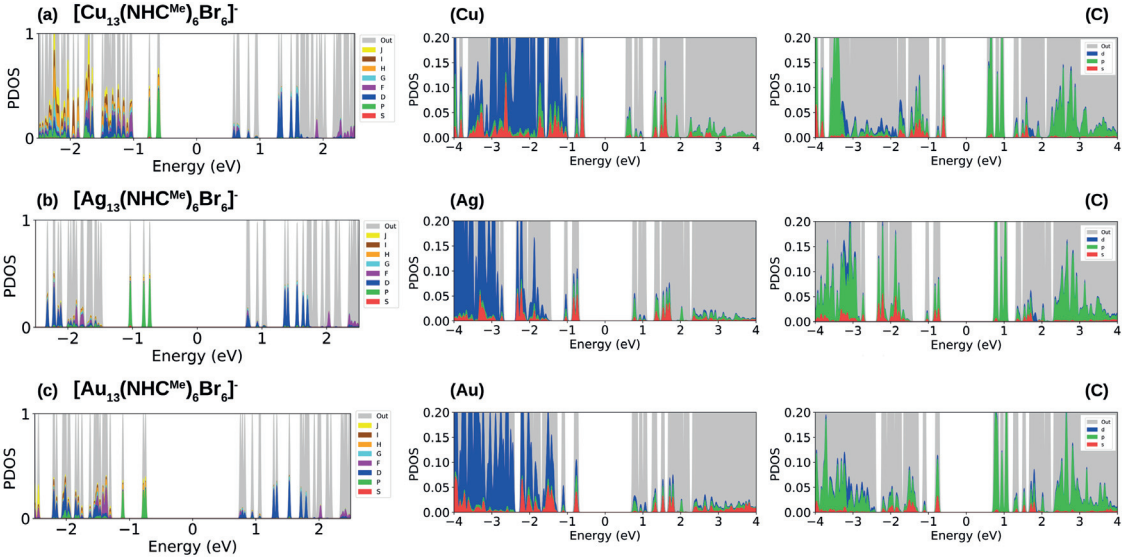

FIGURE 3.4 Projected density of states for (a) $[Cu_{13}(NHC^{Me})_6Br_6]^-$, (b) $[Ag_{13}(NHC^{Me})_6Br_6]^-$, (c) $[Au_{13}(NHC^{Me})_6Br_6]^-$. The leftmost panels show the projection to spherical harmonics functions centered at the center of mass of the cluster (i.e. revealing superatom orbital symmetries) while the two rightmost panels are for the atom-centered projections for Au- and C-atoms separately (i.e. revealing atom orbital symmetries).

exhibiting superior properties compared to silver, albeit not as outstanding as gold. In the case of BEEF-vdW, however, the energies of the NHC-protected clusters are almost isoenergetic, with copper clusters exhibiting a slight advantage over gold clusters.

An investigation into the impact of various ligands on the average bond distance in copper clusters showed that the average value fluctuated between 1.96 Å and 2.00 Å. However, a more pronounced effect was observed on the average M-L bond distance in silver and gold clusters. The study indicated that the choice of ligand had a greater impact on the average bond distance in silver and gold clusters compared to copper clusters. Additionally, the study found that the strength and nature of the bonds between the central metal and peripheral metals in the clusters remained relatively constant, regardless of the type of ligand used.

The Kohn-Sham electron wavefunctions were projected onto spherical harmonics centered at the center of mass of the clusters in order to conduct a Ylm-analysis to reveal the symmetry of electron states for metal clusters protected by NHC^{Me}. As illustrated in figure 3.4, the symmetry of the frontier orbitals of the studied clusters possesses P-symmetry, which is in agreement with what is expected for 8-electron superatoms. This conclusion is further reinforced by the visualized molecular orbitals, which serve to validate the results obtained from the analysis.

In figure 3.4, the atom-based PDOS figures are provided for each NHC^{Me} protected

cluster, with the metal and carbon atoms labeled accordingly. The findings confirm the strength of the bonds between metal and ligand for each cluster as seen also for the simple M-L complexes (Cu > Au > Ag) by illustrating the location of the d-band edge for metal atoms as well as the position of the p-band for the C atoms. For clusters protected by PPh_3, atom-based PDOS yielded the same findings. This set of analyses confirms that the same bonding features that were previously verified for simple M-L complexes similarly influence the binding properties of more complex systems such as clusters.

The Bader analysis for the charge distribution of metal atoms in clusters shows that the charge behavior of these atoms is similar to that of M-L complexes, which are positively charged. However, the gold atoms in $[Au_{13}(PPh_3)_6Br_6]^-$ have a slightly negative charge compared to copper and silver atoms. The phosphorous and carbon atoms in PPh_3 and NHC ligands are positively charged, with phosphorous being more positively charged than carbon.

3.2 Carbene protected Au nanoclusters

3.2.1 $[Au_{10}(NHC)_6Br_3]^+$: a 6-electron superatom cluster

A superatom cluster refers to a collection of atoms that possess a closed-shell electronic configuration, and thus demonstrate behavior comparable to an individual atom. The emergence of superatomic properties in a cluster stems from the interactions between and characteristics of its constituent atoms, resulting in collective behavior of electrons. The seminal work of Knight et al. [107] led to the observation of a plethora of sodium clusters in a gas phase, with an abundance of 2, 8, 20, 40, 58, and 92 atoms, which coincided with the electron shell closings and specific valence electron counts. This finding was highly reminiscent of noble gas atoms, known for their chemical inertness and stability. The stability of superatomic clusters depends on their size and structures exhibiting electronic properties similar to those of individual atoms in the periodic table [108, 109]. As observed for sodium clusters, superatom orbitals follow the *Aufbau* rule, which governs the sequence of electron state occupation [107]. The model developed for metal clusters assumes that the valence electrons are delocalized over the entire cluster. This delocalization results in the valence electrons experiencing a spherically symmetric square well potential in which the order of occupation is given by the series $1S^2 \mid 1P^6 \mid 1D^{10} \mid 2S^2\ 1F^{14} \mid 2P^6\ 1G^{18} \mid 2D^{10}\ 3S^2\ 1H^{22}$, ... corresponding to electron counts of 2, 8, 18, (20), 34, (40), 58, 92, 138, ..., respectively [110]. Where capital letters indicate the angular-momentum characters for the superatom states which are representative of their atomic counterparts. The numbers enclosed in parentheses signify weaker magic numbers that are not as stable as the main ones [110].

These early observations paved the way for the development of the superatom concept, which has since been extended to ligand-protected metal clusters [17, 111]. The incorporation of ligands results in covalent bonding between metal and ligand that can lead to a reduced number of delocalized electrons depending on the ligand type. This happens especially with electrophilic ligands like halides and thiolates. Conversely, ligands like phosphines or NHCs have no effect on electron delocalization.

In 2008, the electron counting rule was introduced as a unified model for ligand-protected nanoclusters [8]. The superatom electron count for the ligand-protected Au nanoclusters with the overall charge of z, represented as $(L_sAu_NX_M)^z$, where, L_s indicates the presence of weak ligands that have no significant influence on the number of delocalized electrons, and X_M denotes the existence of electron-withdrawing ligands such as halides or thiolates.

Therefore, the superatom electron count, n* for ligand protected metal clusters is:

$$n^* = N\nu_A - M - z \tag{3.1}$$

where N is the number of metal atoms, ν_A is the effective metal valence (ν_A =1 for gold atom), M is the number of electron-withdrawing ligands, and z is the overall charge of the cluster. For instance, using equation 3.1, the superatom electron count for the previously studied cluster $[Au_{13}(NHC)_6Br_6]^-$ in section 3.1 is calculated as n* = (13 x 1) - 6 + 1 = 8, corresponding to the electron configuration of $1S^2\ 1P^6$, signifying an 8-electron superatom. Furthermore, as depicted in figure 3.4 (c), the symmetry of the frontier orbitals (HOMO-1 and HOMO-2) in the Au_13 cluster exhibits P-symmetry, as expected for 8-electron superatoms.

The following presents the outcomes of a comprehensive DFT investigation conducted on $[Au_{10}(^{MesCH2}Bimy)_6Br_3]^+$ (Bimy = bipyrimidine) ($[Au_{10}\ (NHC)_6Br_3]^+$) cluster protected by NHC and halide ligands. The study was a part of the research presented in the publication [PII]. The superatomic electron count for this cluster, using equation 3.1, is calculated as n* = (10 × 1) - 3 - 1 = 6, corresponding to a 6-electron superatom and the electron configuration of $1S^2\ 1P^4$. To gain an important understanding of the electronic structures of this cluster I employed a well-studied computational approach explained in section 2.4.3, using equation 2.24 which involves projecting electron wave functions onto spherical harmonics [111, 8, 112, 113, 114, 115, 116, 117]. This analysis is discussed later in this section.

The experimental investigation has revealed that the incorporation of different halides, namely chlorine, bromine, and iodine, significantly influences the stability of the cluster, ultimately leading to transformations over time. Results demonstrated that the incorporation of bromide induces the transformation of Au_{10} clusters into biicosahedral Au_{25} clusters [48] at ambient temperature. In contrast, the cluster containing iodine underwent a transformation into Au_{25} clusters even in the absence of external heat.

In order to validate the experimental observations, the DFT calculations for the $[Au_{10}(NHC)_6Br_3]^+$ cluster were carried out to provide insight into its electronic and optical absorption properties. The analysis started with optimizing the experimental crystal structure using PBE which is shown in figure 3.5. The results indicate that while the calculations accurately predict the overall symmetry of the cluster, the lengths of the Au-Br, Au-C, and Au-Au bonds were slightly overestimated but no bond breaking was observed.

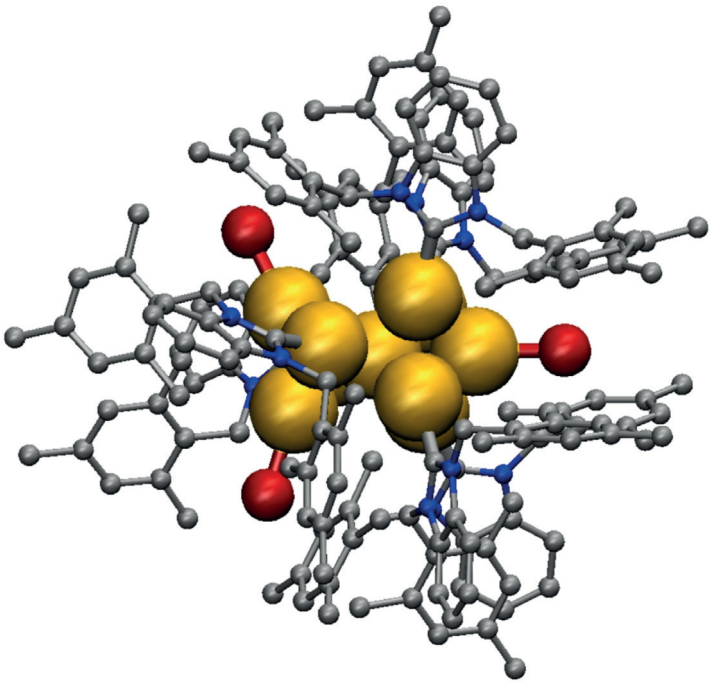

FIGURE 3.5 PBE optimized structure of the crystal structure. The color code for the different atoms is as follows: Au (yellow), Br (red), C (grey), and N (blue). Reprinted with permission from Paul A. Lummis, Kimberly M. Osten, Tetyana I. Levchenko, Maryam Sabooni Asre Hazer, Sami Malola, Bryan Owens-Baird, Alex J. Veinot, Emily L. Albright, Gabriele Schatte, Shinjiro Takano, Kirill Kovnir, Kevin G. Stamplecoskie, Tatsuya Tsukuda, Hannu Häkkinen, Masakazu Nambo, and Cathleen M. Crudden. NHC-Stabilized Au_{10} Nanoclusters and Their Conversion to Au_{25} Nanoclusters. JACS Au, 2(4), pp.875-885, **2022**. Copyright 2022 American Chemical Society

The electronic density of states was investigated by comparing the PDOS obtained by employing PBE and GLLB-SC, as illustrated in figure 3.6 (a) and (b), respectively. The finding suggests that both functionals successfully predict the symmetry of the frontier orbitals, with P-symmetry for the HOMO and HOMO-1 orbitals as expected for the 6-electron superatom, and D-symmetry for the LUMO orbital. Figure 3.7 (a) and (b) validate the symmetry of HOMO and LUMO orbitals by visualizing their corresponding molecular orbitals. In the case of the Au_{10} cluster, the observed major gap at the 6-electron configuration compared to the 8-electron spherical systems can be attributed to its non-spherical geometry. The Au_{10} cluster exhibits an oblate shape, which disturbs the symmetry of the potential well for delocalized electrons in one direction. This disturbance affects the degeneracy of the electronic states, causing the P-symmetric state which is perpendicular to the flat Au-disc to go higher in energy.

By comparing PBE and GLLB-SC, it was found that GLLB-SC provides a more accurate and realistic value for the HOMO-LUMO gap as compared to the experi-

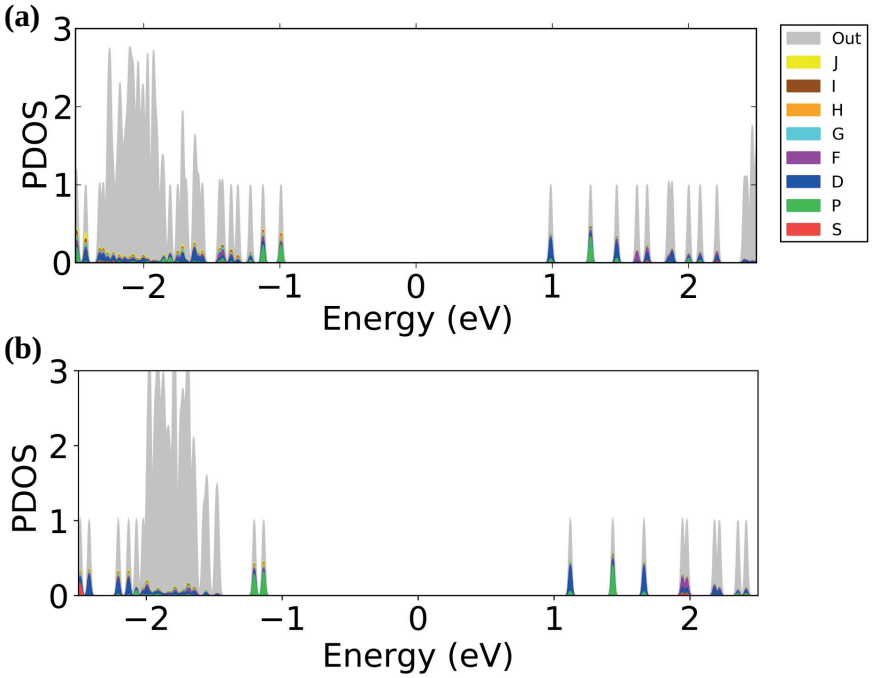

FIGURE 3.6 PBE and GLLB-SC calculated projected density of electron states to spherical harmonics functions centered at the center of mass of the cluster in (a) and (b), respectively. Coloring denotes different angular momenta. Reprinted with permission from Paul A. Lummis, Kimberly M. Osten, Tetyana I. Levchenko, Maryam Sabooni Asre Hazer, Sami Malola, Bryan Owens-Baird, Alex J. Veinot, Emily L. Albright, Gabriele Schatte, Shinjiro Takano, Kirill Kovnir, Kevin G. Stamplecoskie, Tatsuya Tsukuda, Hannu Häkkinen, Masakazu Nambo, and Cathleen M. Crudden. NHC-Stabilized Au_{10} Nanoclusters and Their Conversion to Au_{25} Nanoclusters. JACS Au, 2(4), pp.875-885, **2022**. Copyright 2022 American Chemical Society

mental data with a significant difference of 2.26 eV compared to 1.98 eV calculated by PBE, thus, the GLLB-SC was chosen to carry out the rest of analysis.

Bader charge analysis reported in table 3.2 reveals that in the Au-NHC bonds on the surface of the cluster, NHCs donate electrons of around 0.45 e/ligand and while the central Au atom is slightly withdrawing electrons from the surrounded Au atoms, the gold atoms bonded to ligand groups remain close to neutral. Moreover, as expected bromines withdraw electrons by 0.49 e/Br.

Using LR-TDDFT as explained in section 2.1.2, figure 3.8 illustrates the optical spectrum calculated for $[Au_{10}(NHC)_6Br_3]^+$. The oscillator strengths are represented as blue lines, and the red and green curves represent the Gaussian broadened optical absorption spectra and the experimental optical absorption spectra, respectively. The experimental optical band gap is around 550 nm (2.25 eV), which agrees with the calculated HOMO-LUMO gap (2.26 eV). All the calculated optical absorption peaks were evaluated in DTCM.

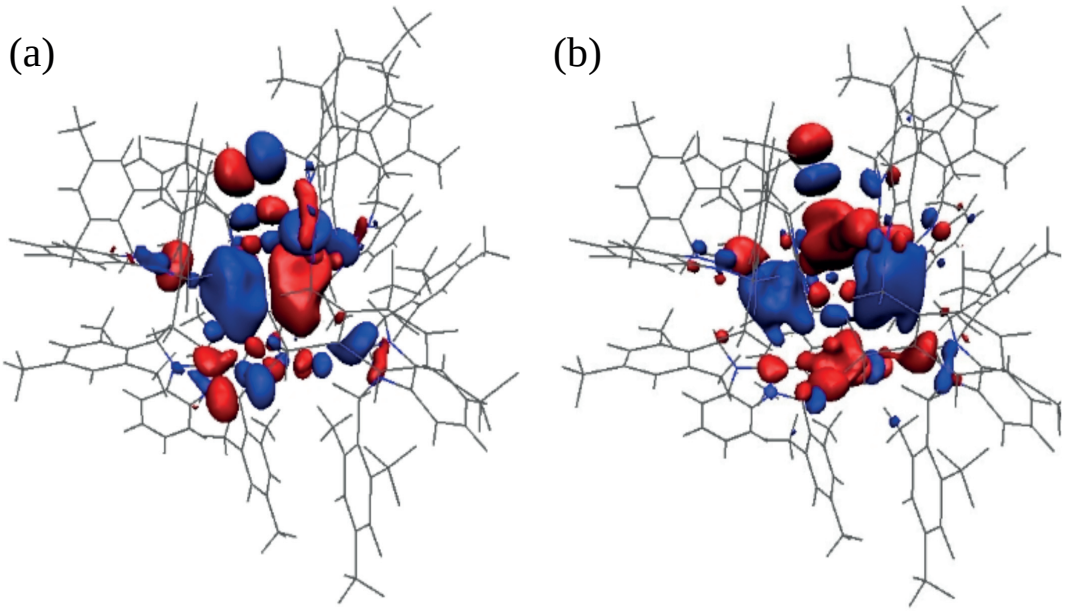

FIGURE 3.7 Visualisation of frontier orbitals for (a) HOMO and (b) LUMO states of cluster $[Au_{10}(NHC)_6Br_3]^+$. Reprinted with permission from Paul A. Lummis, Kimberly M. Osten, Tetyana I. Levchenko, Maryam Sabooni Asre Hazer, Sami Malola, Bryan Owens-Baird, Alex J. Veinot, Emily L. Albright, Gabriele Schatte, Shinjiro Takano, Kirill Kovnir, Kevin G. Stamplecoskie, Tatsuya Tsukuda, Hannu Häkkinen, Masakazu Nambo, and Cathleen M. Crudden. NHC-Stabilized Au_{10} Nanoclusters and Their Conversion to Au_{25} Nanoclusters. JACS Au, 2(4), pp.875-885, **2022**. Copyright 2022 American Chemical Society

TABLE 3.2 Atomic charges of the cluster $[Au_{10}(NHC)_6Br_3]^+$ calculated from Bader charge analysis for gold atoms and ligand groups using GLLB-SC.

Atom group	N	Total Q (e)	Q/N (e)
Central ***Au***	1	-0.084	-0.084
Au-Br	3	-0.086	-0.028
Au-C	6	-0.067	-0.011
Br	3	-1.465	-0.488
NHC	6	+2.703	+0.45

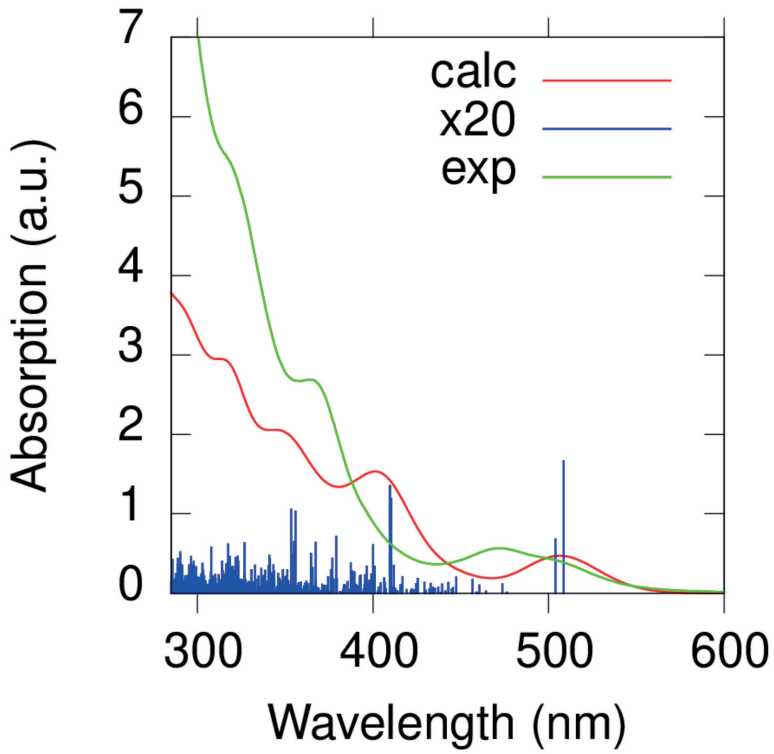

FIGURE 3.8 Calculated (red) and experimental (green) UVvis spectra of the cluster $[Au_{10}(NHC)_6Br_3]^+$. The calculated spectrum is folded from the individual excitations shown as a blue stick spectrum. Reprinted with permission from Paul A. Lummis, Kimberly M. Osten, Tetyana I. Levchenko, Maryam Sabooni Asre Hazer, Sami Malola, Bryan Owens-Baird, Alex J. Veinot, Emily L. Albright, Gabriele Schatte, Shinjiro Takano, Kirill Kovnir, Kevin G. Stamplecoskie, Tatsuya Tsukuda, Hannu Häkkinen, Masakazu Nambo, and Cathleen M. Crudden. NHC-Stabilized Au_{10} Nanoclusters and Their Conversion to Au_{25} Nanoclusters. JACS Au, 2(4), pp.875-885, **2022**. Copyright 2022 American Chemical Society

To understand the origin of the peaks, DTCM provides the contributions of various electron-hole (e-h) transitions as seen in figures 3.9 (a-d) for the first through fourth peaks. In this series of maps, the positive and negative effects on the transition dipole moment are depicted in red and blue, respectively. The atom-based PDOS for a chosen radius is computed individually for Au, Br, C, and N and plotted with the bottom panel indicating the occupied states, and the right panel displaying the unoccupied states. The grey region is all that is left out from the analysis cutoff regions for selected atoms or the ones that are not fitted to the s,p, and d atomic orbitals. Figure 3.9 (a) displays a first peak with a distinct gold-gold character, suggesting electron transition from HOMO to LUMO. However, the impact of electron transitions from ligand to gold is more pronounced at higher peak energies, as illustrated in the second to fourth peaks (figure 3.9 (b) and (c), respectively). In particular, electron transitions from HOMO and HOMO-1 to LUMO+2 (gold-gold transitions) occur at the second peak (figure 3.9 (b)), along

with electron transitions from lower energy states (most of which have ligand character) to unoccupied states (ligand-to-gold transitions).

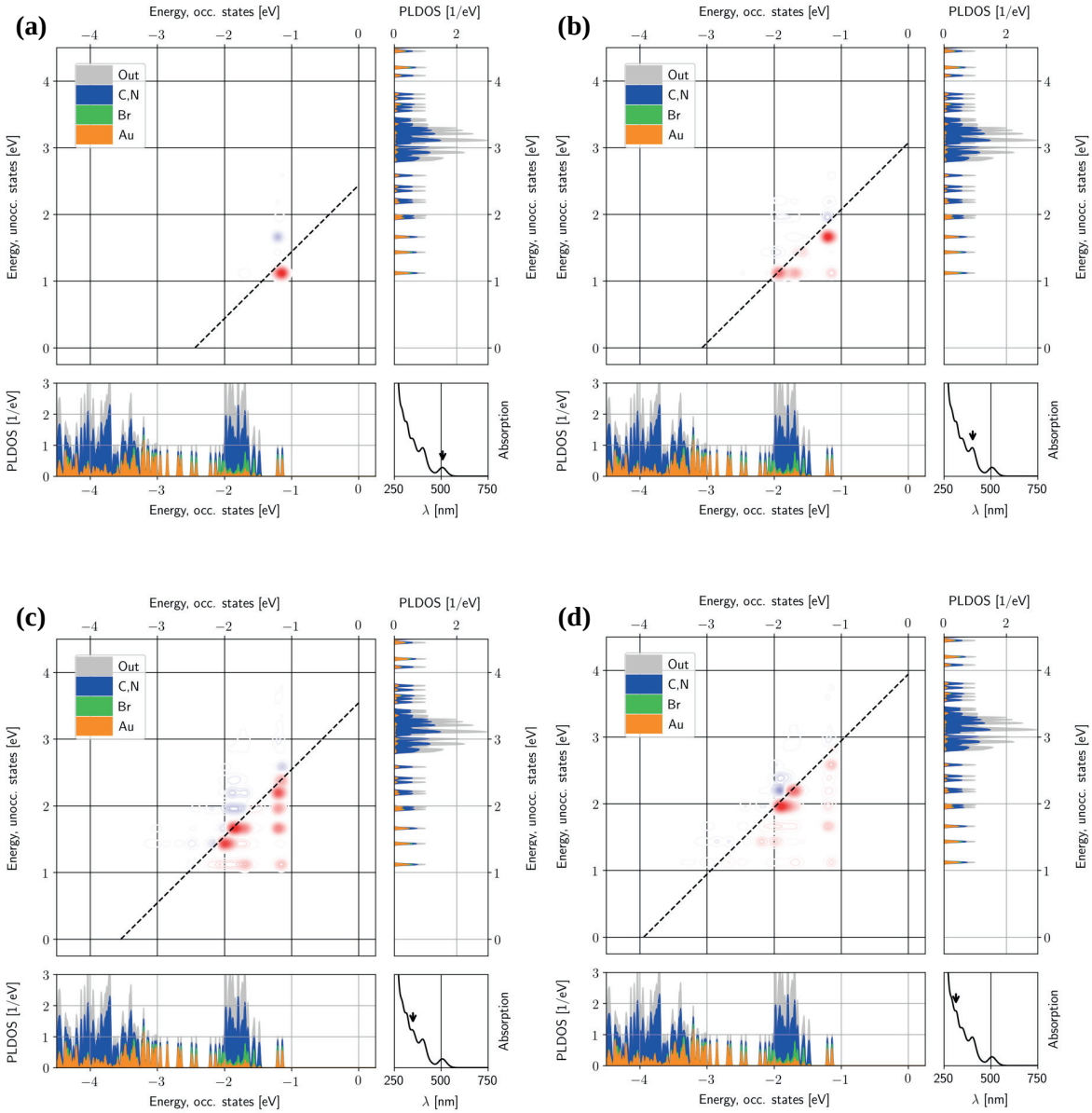

FIGURE 3.9 DTCM analysis for the four selected absorption peaks of the calculated UV-vis spectrum of the cluster $[Au_{10}(NHC)_6Br_3]^+$ shown in panels (a)-(d). The bottom left panel depicts occupied electron states, whereas the vertical panel on the right depicts unoccupied states. The density of states is projected on individual atoms and coloring denotes the localization of the states to different atomic groups. The red and blue regions in the maps represent the constructive and destructive contributions of electron-hole transitions to the overall transition dipole, respectively. The difference in hole-electron orbital energy matches the peak energy at the dashed line. Reprinted with permission from Paul A. Lummis, Kimberly M. Osten, Tetyana I. Levchenko, Maryam Sabooni Asre Hazer, Sami Malola, Bryan Owens-Baird, Alex J. Veinot, Emily L. Albright, Gabriele Schatte, Shinjiro Takano, Kirill Kovnir, Kevin G. Stamplecoskie, Tatsuya Tsukuda, Hannu Häkkinen, Masakazu Nambo, and Cathleen M. Crudden. NHC-Stabilized Au_{10} Nanoclusters and Their Conversion to Au_{25} Nanoclusters. JACS Au, 2(4), pp.875-885, **2022**. Copyright 2022 American Chemical Society

3.3 Mixed NHC-thiolate protected Au cluster

3.3.1 The $[Au_6(NHC\text{-}S)_4]^{2+}$

In contrast to Au superatom clusters which are predominantly composed of an Au(0) core possessing a specific number of valence electrons in a closed-shell electronic configuration, coordination clusters are comprised of Au atoms with 1+ oxidation state [118, 103, 119, 120, 121]. The $[Au_6(NHC\text{-}S)_4]^{2+}$ (NHC= (^{iPr}Bnlm-C_2H_4-(μ_3-S)) cluster presented in [PIII], was found to be a non-superatom, as its superatom electron count is 0 ($n^* = 6 \times 1 - 4 - 2 = 0$).

A bidentate, mono-anionic mixed NHC-sulfide ligand was used to stabilize Au_6 in Paper [PIII]. NHCs have been employed to stabilize metal nanoparticles due to their strong binding affinity towards metals as well as thiolates which have been used as protecting ligands in nanoparticles because of their high coordination capabilities. These successful studies have led to the idea of combining these two binding moieties in a unit ligand to benefit from their bonding properties. According to another study [122], it was demonstrated that a mixed-ligand strategy can be employed to synthesize stable metal clusters utilizing weakly coordinating ligands, such as $SbPh_3$ in $[Au_{13}(SbPh_3)_8Cl_4]^{2+}$.

$[Au_6(NHC\text{-}S)_4]^{2+}$ reported in [PIII] is composed of an anti-prismatic central Au_6 core protected by four NHC-thiolate ligand groups. To study the physicochemical properties of the mentioned nanocluster, first, the experimental crystal structure was optimized using PBE as shown in figure 3.10 which led to no fundamental changes to the structure. However, the Au-Au distances were overestimated by 2-4% compared to the crystal structure, which is typical for the PBE.

To evaluate the electronic properties, a comparison was conducted between the PBE and the GLLB-SC. The results revealed a significant HOMO-LUMO energy gap for both functionals (PBE: 3.22 eV and GLLB-SC: 3.55 eV), which leads to absorption in the UV region. The GLLB-SC absorption spectrum displayed the closest resemblance to the experimental data. As a result, the GLLB-SC was chosen for further electronic property calculations.

The calculated optical absorption spectrum as shown in figure 3.11 in the red curve, indicates three peaks. The first of which at around 328 nm agrees well with the first experimental peak shown in the green curve, while the following two absorption peaks are slightly blue-shifted compared to the experimental peaks. Moreover, one computed high energy peak is located around 250 nm, possibly matching with the measured peak at shorter wavelengths, not visible in the presented range.

PDOS shown in figure 3.12 illustrates the symmetry of the states based on gold

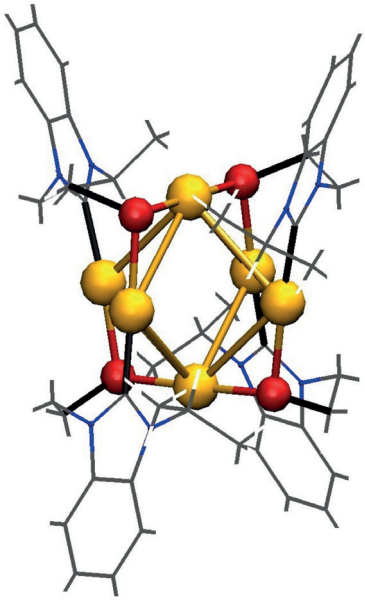

FIGURE 3.10 PBE-optimized structure of the crystal structure for $[Au_6(NHC\text{-}S)_4]^{2+}$. The color code for the different atoms is as follows: Au (yellow), S (red), N (blue), C (grey), and H (white). Reprinted with permission from Kirsi Salorinne, Renee W. Y. Man, Paul A. Lummis, Maryam Sabooni Asre Hazer, Sami Malola, Jacky C.-H. Yim, Alex J. Veinot, Wenxia Zhou, Hannu Häkkinen, Masakazu Nambo, and Cathleen M. Crudden. Synthesis and properties of an Au_6 cluster supported by a mixed N-heterocyclic carbene–thiolate ligand. ChemComm 56(45), 6102-5, **2020**. Copyright 2020 Royal Society of Chemistry.

atoms for a given cutoff of 3.5 Å. By employing this particular approach and visualization of HOMO and LUMO orbitals, as depicted in figure 3.12, it becomes apparent that a mixed ligand-metal character is present which indicates the absence of superatomic symmetry within the system.

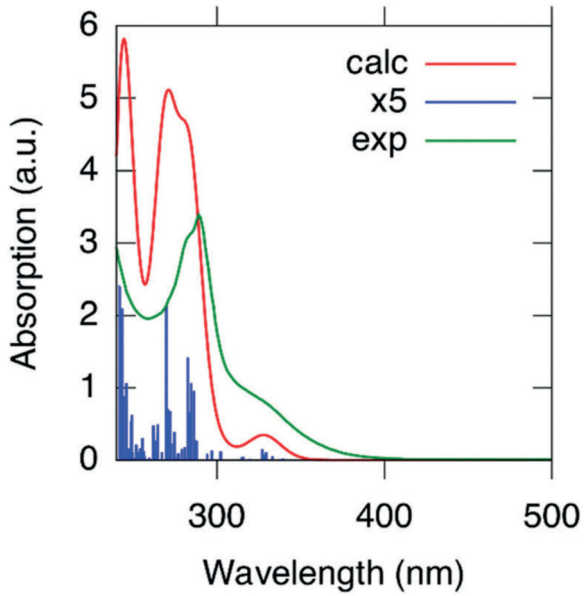

FIGURE 3.11 The calculated (red, GLLB-SC functional) and observed (green) UV-vis optical absorption spectrum of the cluster $[Au_6(NHC\text{-}S)_4]^{2+}$. Using 0.1 eV Gaussian broadening, the computed spectrum is folded from the oscillator strengths (blue lines) of individual transitions. Reprinted with permission from Kirsi Salorinne, Renee W. Y. Man, Paul A. Lummis, Maryam Sabooni Asre Hazer, Sami Malola, Jacky C.-H. Yim, Alex J. Veinot, Wenxia Zhou, Hannu Häkkinen, Masakazu Nambo, and Cathleen M. Crudden. Synthesis and properties of an Au_6 cluster supported by a mixed N-heterocyclic carbene–thiolate ligand. ChemComm 56(45), 6102-5, **2020**. Copyright 2020 Royal Society of Chemistry.

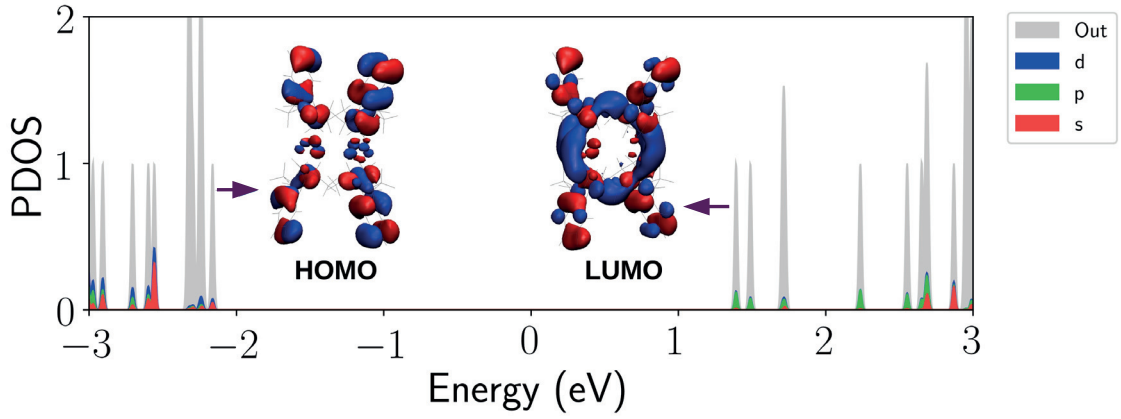

FIGURE 3.12 Projected density of states for Au atoms of the cluster $[Au_6(NHC\text{-}S)_4]^{2+}$. Different colors indicating different symmetries of states. The Kohn-Sham frontier molecular orbitals are depicted for HOMO (left) and LUMO (right). Modified with permission from Kirsi Salorinne, Renee W. Y. Man, Paul A. Lummis, Maryam Sabooni Asre Hazer, Sami Malola, Jacky C.-H. Yim, Alex J. Veinot, Wenxia Zhou, Hannu Häkkinen, Masakazu Nambo, and Cathleen M. Crudden. Synthesis and properties of an Au_6 cluster supported by a mixed N-heterocyclic carbene–thiolate ligand. ChemComm 56(45), 6102-5, **2020**. Copyright 2020 Royal Society of Chemistry.

3.3.2 Isomer dynamics of the Au_6 nanocluster

This section provides an explanation for the findings presented in the paper [PIV]. To do so, I will first raise the question of whether the experimentally synthesized crystalline cluster of $[Au_6(NHC\text{-}S)_4]^{2+}$ [123] can be considered the most stable structure with certainty. To answer this question, DFT-MD simulations can be used to monitor the cluster topologies at various targeted temperatures over a period of time, enabling us to explore the potential isomers for the known crystal structure. Although the crystallization of metal nanoclusters plays a crucial role in understanding the properties of these clusters, it also has the potential to miss important information about the presence of low-energy structural isomers. Depending on the size of the clusters, searching for the isomers can be an expensive task. Luckily, in the case of the above-mentioned small cluster $[Au_6(NHC\text{-}S)_4]^{2+}$, the use of DFT-MD simulations presents an opportunity for cost-effective time iterations which makes it feasible to perform these simulations and can provide valuable insight into the stability of the cluster and can reveal the existence of different isomers.

$[Au_6(NHC\text{-}S)_4]^{2+}$ consists of a central Au_6 core in an anti-prismatic configuration, which is stabilized by four ligand groups of mixed NHC-thiolates. To investigate the potential isomers for this cluster, DFT-MD simulations (see section 2.2) were conducted for the experimentally optimized crystal structure presented in figure 3.13 (a), as previously explained in a published study [123]. The simulations were

carried out at three different temperatures, approximately 145 K, 280 K, and 475 K with the total length of simulation of 20 ps, 10 ps, and 30 ps, respectively. The impact of temperature on the electronic properties of the system during the MD simulations of 2 fs time steps was evaluated.

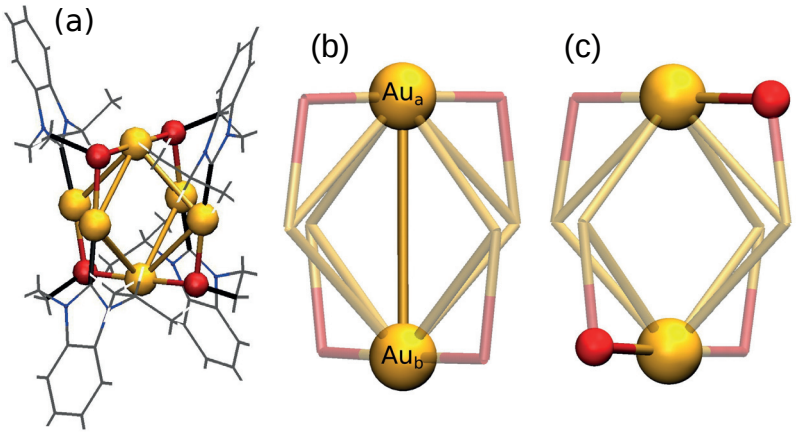

FIGURE 3.13 (a) Optimized crystal structure of $[Au_6(NHC\text{-}S)_4]^{2+}$ using PBE. (b) Distance between Au_a-Au_b (4.74 Å) part of SR-Au-SR linear motif. (c) Dihedral angle of S-Au-Au-S (89.10°). (Au: yellow, S: red, N: blue, C: gray, H: white). Reprinted with permission from Maryam Sabooni Asre Hazer, Sami Malola, and Hannu Häkkinen. Isomer dynamics of the $[Au_6(NHC\text{-}S)_4]^{2+}$ nanocluster. ChemComm, 58(19), 3218-3221, **2022**. Copyright 2022 Royal Society of Chemistry.

In our calculations, the Au_a-Au_b distance (4.74 Å for relaxed crystal structure shown in figure 3.13 (b)) and the dihedral angle of SR-Au-SR (89.10° for the relaxed crystal structure shown in figure 3.13 (c)) are the two main parameters in the cluster $[Au_6(NHC\text{-}S)_4]^{2+}$ to evaluate the degree of structural variations. The total energy variations over time for DFT-MD simulations at three different temperatures (145K, 280K, and 475K) are displayed in figure 3.14 (a), (b), and (c). Seven snapshot structures as shown in the figure were selected based on their proximity to the lowest local energy. As shown in table 3.3, after optimizing the chosen structures, the selected isomers were found to be more stable than the crystal structure (0.19-0.42 eV per cluster). According to the table 3.3, the most stable configuration was determined to be isomer number 2 found at 145 K. Table 3.3 displays the findings of a geometrical comparison between the selected configurations and the crystal structure. The results illustrate that the structures undergo significant changes over time, with a tendency to become more compact and twisted without any bond breaking.

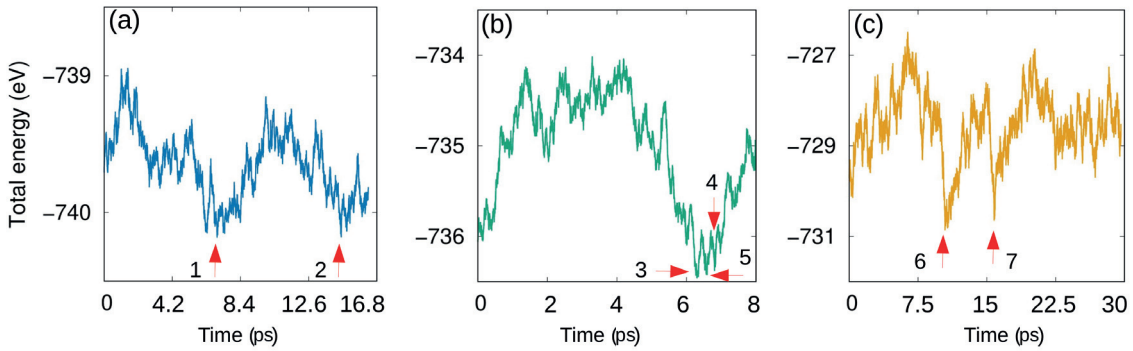

FIGURE 3.14 DFT-MD total energy as a function of time for three different runs in (a) 145 K, (b) 280 K, and (c) 475 K. The chosen $[Au_6(NHC\text{-}S)_4]^{2+}$ isomers are denoted with labels 1-7. Reprinted with permission from Maryam Sabooni Asre Hazer, Sami Malola, and Hannu Häkkinen. Isomer dynamics of the $[Au_6(NHC\text{-}S)_4]^{2+}$ nanocluster. ChemComm, 58(19), 3218-3221, **2022**. Copyright 2022 Royal Society of Chemistry.

TABLE 3.3 Geometrical and energetic comparison between selected isomers of $[Au_6(NHC\text{-}S)_4]^{2+}$ in varying temperatures as compared to the relaxed crystal structure.

Temperature (K)	Isomer numbers	Dihedral angle (°) of S-Au-Au-S	Au_a-Au_b distance (Å)	Relaxed energy (eV)
-	static crystal structure	89.3	4.74	0
145	1	100.4	3.62	-0.40
145	2	101.6	3.83	-0.42
280	3	103.6	3.60	-0.32
280	4	99.4	3.75	-0.33
280	5	100.4	3.78	-0.35
475	6	94.7	3.83	-0.19
475	7	106.6	3.51	-0.33

Following the geometrical properties, the electronic characteristics at the previously stated temperatures have been studied. Studying the correlation between HOMO-LUMO energy gap values in different Au_a-Au_b distances as shown in figure 3.15 depicts that the most compact configurations have the lowest HOMO-LUMO energy gaps which is universal for all temperatures.

Figure 3.16 illustrates a comparison of the optical absorption spectra computed for the static crystal structure (represented as a yellow curve) and the single particle transitions for 120 snapshot structures derived from the DFT-MD simulation at 145 K. (Check the figures S3 and S4 of publication [PIV] for the comparison of optical absorption spectra between the experimental data and the findings calculated at temperatures of 280 K and 475 K, respectively.) This comparison sheds light on the significance of small structural changes on optical properties, validating our original goal of identifying probable isomers. The variation between the PBE-optimized absorption spectrum for static crystal structure and for the DFT-MD simulations is depicted by two main aspects: (1) the initial peak (I) found in the

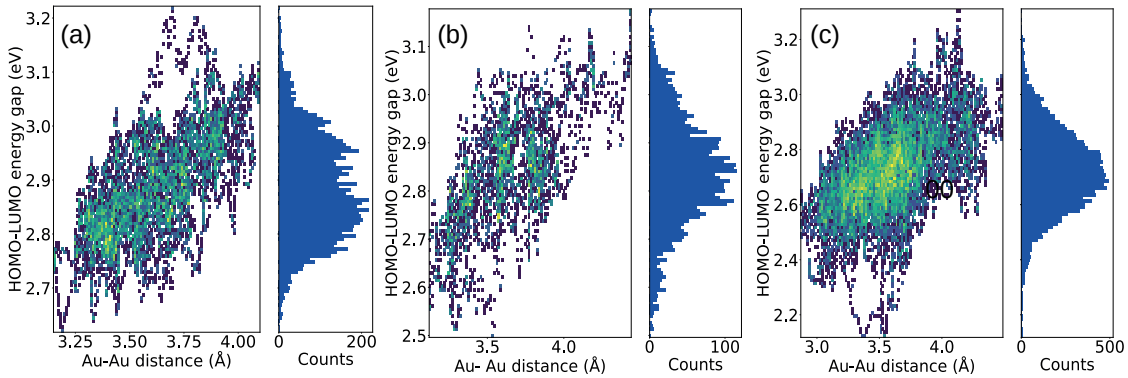

FIGURE 3.15 Heat and distribution maps of HOMO-LUMO gap fluctuation with respect to the Au_a-Au_b distance for $[Au_6(NHC\text{-}S)_4]^{2+}$ cluster at three temperatures: (a) 145 K, (b) 280 K and (c) 475 K. The most densely populated area with similar HOMO-LUMO energy gap values is depicted with lighter colors. Reprinted with permission from Maryam Sabooni Asre Hazer, Sami Malola, and Hannu Häkkinen. Isomer dynamics of the $[Au_6(NHC\text{-}S)_4]^{2+}$ nanocluster. ChemComm, 58(19), 3218-3221, **2022**. Copyright 2022 Royal Society of Chemistry.

DFT-MD simulation is missing from the absorption spectrum of single crystal structure, and (2) the peaks (a), (b), and (c) in the single crystal structure are blue-shifted compared to the peaks in the DFT-MD simulations which are observed at around 350 nm (II), 310 nm (III), and 285 nm (IV). However, the peaks at 290 nm (d) and 285 nm (IV) show a comparable match.

The DTCMs for these peaks shown in Figure 3.17 illustrate the contributions of several electron-hole transitions. To analyze the optical absorption peaks for dynamic structures, a configuration that has the most similarity in peak positions to the combined absorption spectrum of all 120 dynamic configurations was selected as a representative system.

The comparison of the first two peaks of the selected dynamic structure (figure 3.17 (a) and (b)) to the first absorption peak of the PBE-relaxed crystal structure (figure 3.17 (c)) shows that the electron transitions in the first peak of the PBE-optimized structure are a combination of HOMO to LUMO+1 and HOMO-2 and HOMO-3 to LUMO. The two main electron-hole transitions can also be observed in the first and second peaks of the dynamic structure, where the first peak shows a clear HOMO to LUMO+1 transition along with transitions from lower occupied states

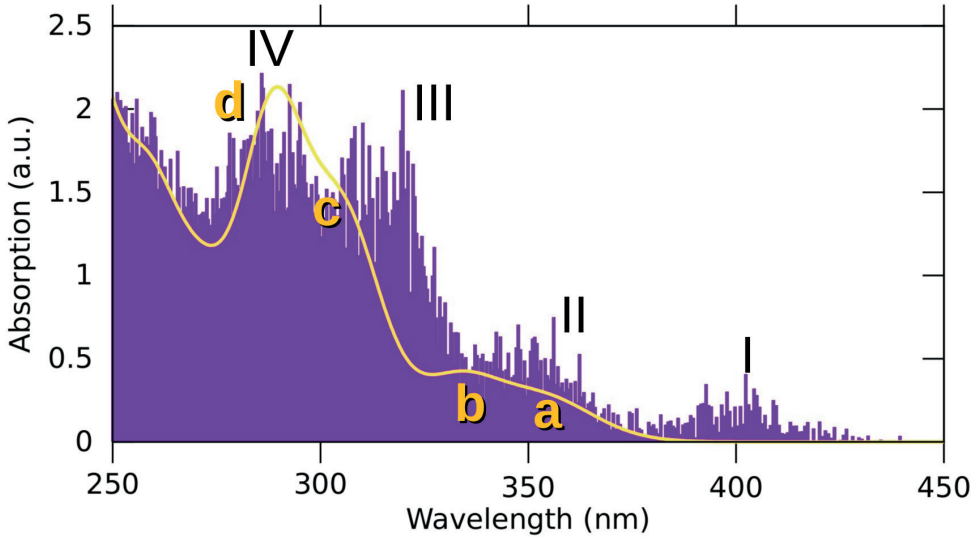

FIGURE 3.16 Optical absorption spectra of the single crystal structure (represented by a yellow curve) and dynamic structures of $[Au_6(NHC\text{-}S)_4]^{2+}$ cluster (represented by purple lines) obtained by combining 120 snapshot structures taken at every 65 steps. The dynamic structures' spectrum is represented as a stick spectrum, which includes all single particle transitions and their oscillator strengths from the 120 structures that are grouped into energy bins. The observed peaks of the stick spectrum are labeled with I-IV. Meanwhile, the single crystal structure's spectrum is broadened by 0.1 eV Gaussians, and the peaks are labeled with a-d. Reprinted with permission from Maryam Sabooni Asre Hazer, Sami Malola, and Hannu Häkkinen. Isomer dynamics of the $[Au_6(NHC\text{-}S)_4]^{2+}$ nanocluster. ChemComm, 58(19), 3218-3221, **2022**. Copyright 2022 Royal Society of Chemistry.

to LUMO+1. Our findings reveal that the higher energy peaks exhibit a greater number of transitions and display more collective behavior compared to the lower energy peaks (figures S6 (a) and (b) and S7 (a-c) of publication [PIV] provide a comprehensive look at the e-h transitions of the higher energy peaks).

The splitting of the first crystal structure peak into two distinct peaks in the finite temperature can be explained by looking at the time evolution of the energy levels for occupied and unoccupied states as shown in figure 3.18 (a) and (b), respectively. This figure indicates that the HOMO state has a significant fluctuation in energy, with a variation of 0.5 eV at 145 K. This fluctuation causes the HOMO state to separate from the group of lower-lying states over time. On the other hand, the energy levels of other states also show changes, but these fluctuations are much smaller compared to the HOMO.

Eventually, in order to perform a final validation of the observed isomerism, an additional MD simulation was performed by mimicking the crystal structure conditions. As shown in figure 3.19 (a) MD simulations started with the lowest-energy gas phase isomer number 2 surrounded by counterions (10 PF_6^-) and solvent

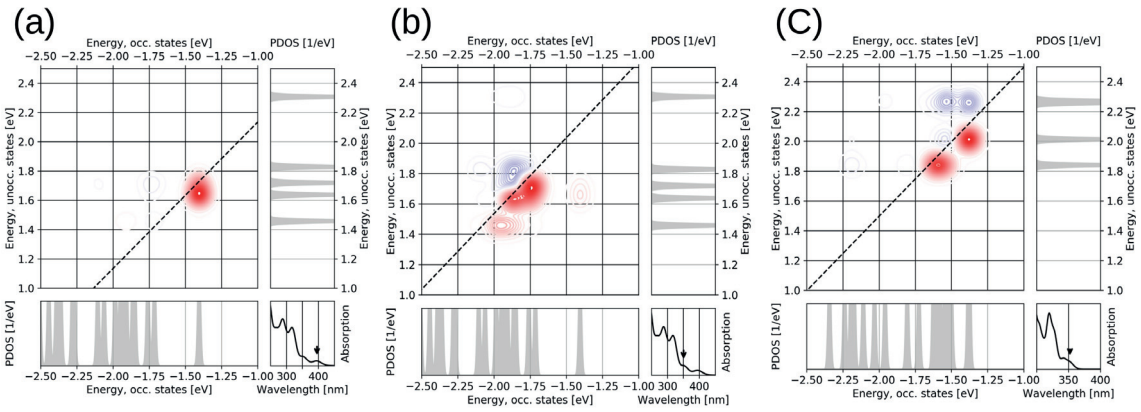

FIGURE 3.17 Comparison between DTCM of the lower energy peaks of the representative dynamic structure of $[Au_6(NHC\text{-}S)_4]^{2+}$ in a)-b) and of the relaxed crystal structure in c). The strengthening and screening contributions of the chosen absorption peak are shown in red and blue, respectively. The absorption peak is labeled in the spectrum in the lower right panel. The occupied electron states are displayed in the bottom left subplot, while the unoccupied electron states are portrayed in the right vertical subplot. Reprinted with permission from Maryam Sabooni Asre Hazer, Sami Malola, and Hannu Häkkinen. Isomer dynamics of the $[Au_6(NHC\text{-}S)_4]^{2+}$ nanocluster. ChemComm, 58(19), 3218-3221, **2022**. Copyright 2022 Royal Society of Chemistry.

molecules (2 EtOH) resembling the arrangement of the original crystal structure, as described ref. [123]. The results showed that the cluster spontaneously reverted to the crystal structure conformation. The analysis revealed a significant increase in the Au_a-Au_b distance (as shown in figure 3.19 (c)), fluctuating around 4.6 Å. Concurrently, the S-Au-Au-S dihedral angle decreased (as shown in figure 3.19 (b)), oscillating around 85°. Notably, the crystal structure conformation was absent from the structural phase spaces generated by the MD simulations for the isolated cluster. Moreover, the MD simulation incorporating the surrounding counterions and molecules provides direct evidence that the crystal packing influences the precise structure of the cluster. This is just one unique example among a potentially vast array of isomeric structures that may exist in the sample in the solution. It is important to note that the structure observed in the crystal is likely optimized for packing and maximizing interactions, which may not necessarily be representative of the solution-phase behavior.

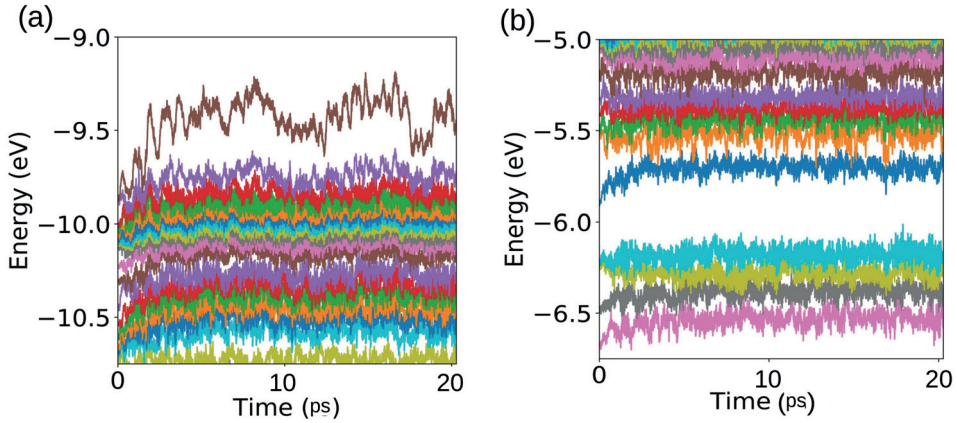

FIGURE 3.18 The energy fluctuations of the (a) occupied states and (b) unoccupied states as a function of time at 145 K (different states are represented in various colors). Reprinted with permission from Maryam Sabooni Asre Hazer, Sami Malola, and Hannu Häkkinen. Isomer dynamics of the $[Au_6(NHC\text{-}S)_4]^{2+}$ nanocluster. ChemComm, 58(19), 3218-3221, **2022**. Copyright 2022 Royal Society of Chemistry.

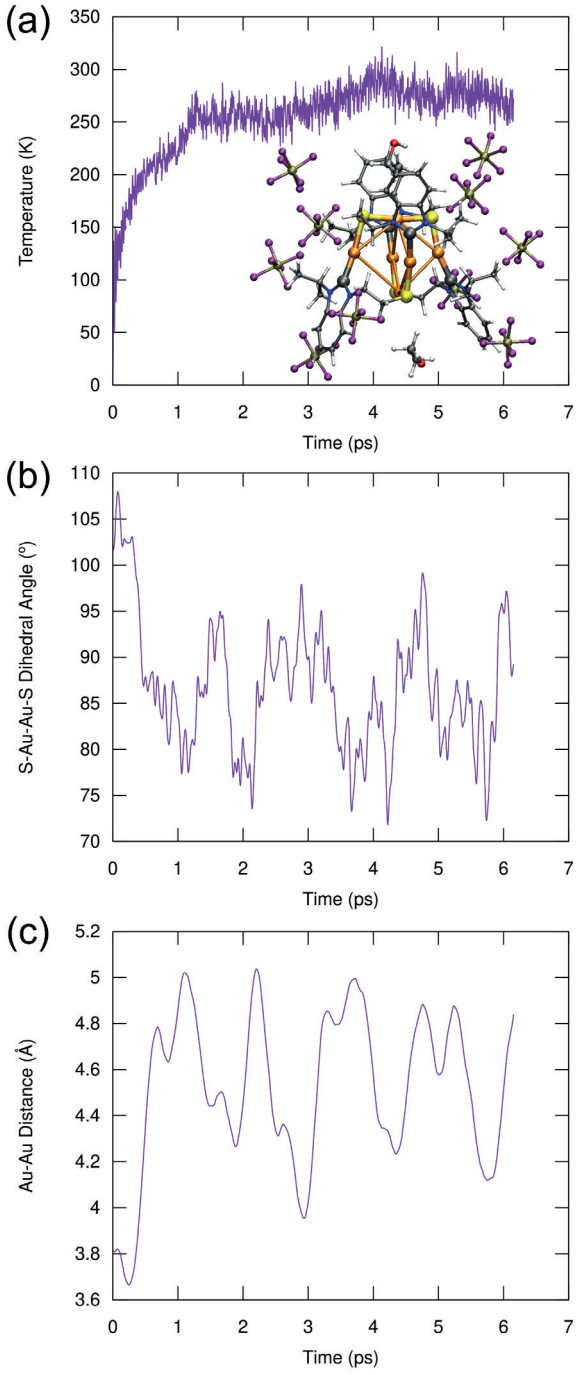

FIGURE 3.19 The behavior of (a) temperature, (b) dihedral angle of S-Au-Au-S and (c) distance between Au atoms as a function of time during MD-simulation at 269K for the most stable gas phase isomer of Au_6 cluster with 10 counterions ($PF6^-$) and 2 molecules of EtOH, their positions being comparable arrangement seen in the crystal structure. Reprinted with permission from Maryam Sabooni Asre Hazer, Sami Malola, and Hannu Häkkinen. Isomer dynamics of the $[Au_6(NHC\text{-}S)_4]^{2+}$ nanocluster. ChemComm, 58(19), 3218-3221, **2022**. Copyright 2022 Royal Society of Chemistry.

4 CONCLUSIONS AND OUTLOOK

In this thesis, I showed the difference in the bonding nature of phosphine, thiolates, and NHCs to group-11 metal atoms in M-L complexes and metal clusters, concluding that NHC ligands have superior bonding stability compared to the other two. I also discussed the electronic structures and optical properties of two distinct ligand-protected gold nanoclusters. Furthermore, an investigation of isomerization for a relatively small-size Au nanocluster was undertaken using DFT-based MD simulations at varying temperatures, yielding novel insights.

The manuscript [PI] presents compelling evidence indicating that NHCs exhibit superior bonding strength with metals when compared to thiolates and PPh_3. This is attributed to the tendency of NHCs to form σ-type bonds, which are inherently stronger than π-type bonds. While both NHCs and phosphorous-containing ligands form σ-type bonds, it is noted that PPh_3 exhibits lower binding energies to metals. Additionally, the charge transfer behavior between atoms engaged in M-L bonding remains unaffected by the diverse side groups present in NHCs. Our findings align with those reported previously emphasizing the remarkable bond stability of NHCs compared to thiolates [59] and PPh_3 [47] ligands.

The publication [PII], provides a comprehensive analysis of the electronic structure and optical properties of $[Au_{10}(NHC)_6Br_3]^+$. I demonstrated that Au_{10} is a 6-electron superatom cluster, explaining the hypothesis that Au_{10} converts to Au_{25} due to increased metallicity, from 6 to 16 electrons [48]. The calculations showed a good agreement between the calculated and experimental absorption spectra and explained that the origin of the absorption peaks is due to gold-to-gold transitions at lower and ligand-to-gold transitions at higher energies.

In article [PIII], the evidence of the successful stabilization of Au_6 using a bidentate mixed NHC-thiolate ligand is provided. My study on the $[Au_6(NHC\text{-}S)_4]^{2+}$ nanocluster indicated the absence of a well-defined superatomic symmetry for

the frontier orbitals, with a significantly large HOMO-LUMO energy gap. The calculated UV-vis optical absorption spectra demonstrated a good agreement with the corresponding experimental data. Analysis of the peaks revealed a strong ligand-to-metal character for the first two peaks, however, the higher energy peak illustrated the metal-to-metal contribution.

In the paper [PIV], the DFT-based MD simulations at three different temperatures revealed the isomerism of the relatively small gold nanocluster $[Au_6(NHC\text{-}S)_4]^{2+}$. The findings revealed the presence of at least seven isomers at varying temperatures and suggest that the transition between these isomers is reversible without bond breakage. The optical and electronic properties of the nanocluster were shown to be dependent on the isomer configurations which highlights the importance of understanding isomerism. Furthermore, I discussed that the crystallized structure is not necessarily the lowest energy isomer in the gas phase or vice versa. These observations prompt the need for further investigation into how the presence of isomers affects the processes of crystallization and catalytic activity of nanoclusters under different conditions.

This thesis highlighted the significant role of computational methods in gaining a comprehensive understanding of the experimentally observed properties of gold nanoclusters together with the discovery of novel isomers with distinct properties. The findings presented herein point out that it is realistic to observe isomerism in protected metal nanoclusters in ambient conditions. Furthermore, it is important to realize that isomers exert a notable influence on the behavior and properties of the nanoclusters like reactivity which may be distinguishable in solution and crystal phases. This may lead to their use as new catalytic materials. In addition, a thorough examination of diverse isomers can potentially lead to the discovery of other novel applications. However, employing conventional computational methods to characterize isomers under varying reaction conditions can be challenging and time-consuming.

In my opinion, by expanding the boundaries of conventional computational tools with machine learning methods, new insights, and discoveries can be unveiled that can shape the future of nanoscience. In recent years, we have witnessed that machine learning algorithms analyzed and interpreted vast amounts of data on the behavior of nanomaterials. This method has been successful in predicting new materials in addition to providing efficient force fields for atomic interactions that approach quantum mechanical accuracy [124, 125, 126, 127, 128].

To overcome the limitations of studying nanoclusters, there is a growing trend in the field toward the integration of machine learning and MD simulations. By using machine learning, researchers can rapidly study the structural features and key properties that govern the behavior of nanoclusters, enabling them to efficiently screen a vast number of potential candidates for further investigation.

Additionally, MD simulations can provide a detailed understanding of the behavior of nanoclusters under different reaction conditions, allowing researchers to optimize the synthesis conditions and tune the properties of nanoclusters to meet specific application requirements. This would lead to the development of a robust framework that integrates computational and experimental approaches to accelerate the discovery of new materials and applications.

REFERENCES

[1] A. Junk and F. Riess. *Am. J. Phys.*, **74**, 825 (2006).

[2] *Press release for the 1986 Nobel Prize in physics* (1986).

[3] B. Yin and Z. Luo. *Coord. Chem. Rev.*, **429**, 213643 (2021).

[4] J.-H. Huang, X.-Y. Dong, Y.-J. Wang and S.-Q. Zang. *Coord. Chem. Rev.*, **470**, 214729 (2022).

[5] H. Si, T. Shu, X. Du, L. Su and X. Zhang. *Biosensors*, **12**, 511 (2022).

[6] R. Sardar, A. M. Funston, P. Mulvaney and R. W. Murray. *Langmuir*, **25**, 13840 (2009).

[7] V. Yarzhemsky, E. Murav'Ev, M. Kazaryan and Y. A. Dyakov. *Inorg. Mater.*, **48**, 1075 (2012).

[8] M. Walter, J. Akola, O. Lopez-Acevedo, P. D. Jadzinsky, G. Calero, C. J. Ackerson, R. L. Whetten, H. Grönbeck and H. Häkkinen. *PNAS*, **105**, 9157 (2008).

[9] R. Jin. *Nanoscale*, **7**, 1549 (2015).

[10] H. Yu, B. Rao, W. Jiang, S. Yang and M. Zhu. *Coord. Chem. Rev.*, **378**, 595 (2019).

[11] C. M. Aikens. *J. Phys. Chem. A .*, **113**, 10811 (2009).

[12] S. Kukreti, M. Kaushik *et al. Talanta*, **234**, 122623 (2021).

[13] S. Qian, Z. Wang, Z. Zuo, X. Wang, Q. Wang and X. Yuan. *Coord. Chem. Rev.*, **451**, 214268 (2022).

[14] Y. Yu, Z. Luo, D. M. Chevrier, D. T. Leong, P. Zhang, D.-e. Jiang and J. Xie. *J. Am. Chem. Soc.*, **136**, 1246 (2014).

[15] S. Knoppe, O. A. Wong, S. Malola, H. Hakkinen, T. Burgi, T. Verbiest and C. J. Ackerson. *J. Am. Chem. Soc.*, **136**, 4129 (2014).

[16] L. Liao, S. Zhuang, C. Yao, N. Yan, J. Chen, C. Wang, N. Xia, X. Liu, M.-B. Li, L. Li *et al. J. Am. Chem. Soc.*, **138**, 10425 (2016).

[17] T. Tsukuda and H. Häkkinen. *Protected metal clusters: from fundamentals to applications*. Elsevier (2015).

[18] S. Hossain, D. Hirayama, A. Ikeda, M. Ishimi, S. Funaki, A. Samanta, T. Kawawaki and Y. Negishi. *Aggregate*, page e255 (2022).

[19] R. H. Adnan, J. M. L. Madridejos, A. S. Alotabi, G. F. Metha and G. G. Andersson. *Adv. Sci.*, **9**, 2105692 (2022).

[20] S. R. Thomas and A. Casini. *J. Organomet. Chem.*, **938**, 121743 (2021).

[21] P. Maity, S. Xie, M. Yamauchi and T. Tsukuda. *Nanoscale*, **4**, 4027 (2012).

[22] H. Shen, G. Tian, Z. Xu, L. Wang, Q. Wu, Y. Zhang, B. K. Teo and N. Zheng. *Coord. Chem. Rev.*, **458**, 214425 (2022).

[23] Y. Negishi. *Phys. Chem. Chem. Phys.*, **24**, 7569 (2022).

[24] X.-K. Wan, S.-F. Yuan, Q. Tang, D.-e. Jiang and Q.-M. Wang. *Angew. Chem. Int. Ed.*, **54**, 5977 (2015).

[25] S. Li, W. Tian and Y. Liu. *Nanoscale*, **13**, 16847 (2021).

[26] R. R. Nasaruddin, T. Chen, N. Yan and J. Xie. *Coord. Chem. Rev.*, **368**, 60 (2018).

[27] L. Naldini, F. Cariati, G. Simonetta and L. Malatesta. *Chem. Commun. (London)*, pages 647–648 (1966).

[28] L. Malatesta, L. Naldini, G. Simonetta and F. Cariati. *Chem. Commun. (London)*, pages 212–213 (1965).

[29] F. Cariati and L. Naldini. *Inorganica Chim. Acta*, **5**, 172 (1971).

[30] C. E. Briant, B. R. Theobald, J. W. White, L. K. Bell, D. M. P. Mingos and A. J. Welch. *J. Chem. Soc., Chem. commun.*, pages 201–202 (1981).

[31] X.-K. Wan, Z.-W. Lin and Q.-M. Wang. *J. Am. Chem. Soc.*, **134**, 14750 (2012).

[32] H. Qian, W. T. Eckenhoff, M. E. Bier, T. Pintauer and R. Jin. *Inorg. Chem.*, **50**, 10735 (2011).

[33] L. C. McKenzie, T. O. Zaikova and J. E. Hutchison. *J. Am. Chem. Soc.*, **136**, 13426 (2014).

[34] P. D. Jadzinsky, G. Calero, C. J. Ackerson, D. A. Bushnell and R. D. Kornberg. *science*, **318**, 430 (2007).

[35] H. Häkkinen. *Nat. Chem.*, **4**, 443 (2012).

[36] M. W. Heaven, A. Dass, P. S. White, K. M. Holt and R. W. Murray. *J. Am. Chem. Soc.*, **130**, 3754 (2008).

[37] H. Qian, W. T. Eckenhoff, Y. Zhu, T. Pintauer and R. Jin. *J. Am. Chem. Soc.*, **132**, 8280 (2010).

[38] N. Yan, N. Xia, L. Liao, M. Zhu, F. Jin, R. Jin and Z. Wu. *Sci. Adv.*, **4**, eaat7259 (2018).

[39] Y. Song, S. Wang, J. Zhang, X. Kang, S. Chen, P. Li, H. Sheng and M. Zhu. *J. Am. Chem. Soc.*, **136**, 2963 (2014).

[40] W. Kurashige, S. Yamazoe, M. Yamaguchi, K. Nishido, K. Nobusada, T. Tsukuda and Y. Negishi. *The J. Phys. Chem. Lett.*, **5**, 2072 (2014).

[41] M. M. Nigra, A. J. Yeh, A. Okrut, A. G. DiPasquale, S. W. Yeh, A. Solovyov and A. Katz. *Dalton Trans.*, **42**, 12762 (2013).

[42] A. Muñoz-Castro. *Inorg. Chem. Frontiers*, **6**, 2349 (2019).

[43] M. R. Narouz, S. Takano, P. A. Lummis, T. I. Levchenko, A. Nazemi, S. Kaappa, S. Malola, G. Yousefalizadeh, L. A. Calhoun, K. G. Stamplecoskie *et al. J. Am. Chem. Soc.*, **141**, 14997 (2019).

[44] Q. Wu, R. Peng, F. Gong, Y. Luo, H. Zhang and Q. Cui. *Colloids and Surfaces A: Physicochemical and Engineering Aspects*, **645**, 128934 (2022). ISSN 0927-7757. doi:https://doi.org/10.1016/j.colsurfa.2022.128934. URL https://www.sciencedirect.com/science/article/pii/S0927775722006896.

[45] G. Kaur, R. L. Thimes, J. P. Camden and D. M. Jenkins. *Chem. Commun.* (2022).

[46] T. J. Robilotto, J. Bacsa, T. G. Gray and J. P. Sadighi. *Angew. Chem. Int. Ed.*, **51**, 12077 (2012).

[47] M. R. Narouz, K. M. Osten, P. J. Unsworth, R. W. Man, K. Salorinne, S. Takano, R. Tomihara, S. Kaappa, S. Malola, C.-T. Dinh *et al. Nat. Chem.*, **11**, 419 (2019).

[48] H. Shen, G. Deng, S. Kaappa, T. Tan, Y.-Z. Han, S. Malola, S.-C. Lin, B. K. Teo, H. Häkkinen and N. Zheng. *Angew. Chem.*, **131**, 17895 (2019).

[49] M. Rambukwella, L. Sementa, A. Fortunelli and A. Dass. *J. Phys. Chem. C*, **121**, 14929 (2017).

[50] A. Ghosh, D. Ghosh, E. Khatun, P. Chakraborty and T. Pradeep. *Nanoscale*, **9**, 1068 (2017).

[51] K. Krishnadas, A. Baksi, A. Ghosh, G. Natarajan, A. Som and T. Pradeep. *Acc. Chem. Res.*, **50**, 1988 (2017).

[52] S.-S. Chen, P. Wang, S. Takamizawa, T.-a. Okamura, M. Chen and W.-Y. Sun. *Dalton Trans.*, **43**, 6012 (2014).

[53] K. M. Jensen, P. Juhas, M. A. Tofanelli, C. L. Heinecke, G. Vaughan, C. J. Ackerson and S. J. Billinge. *Nat. Commun.*, **7**, 1 (2016).

[54] X. Kang and M. Zhu. *Chem. Mater.*, **33**, 39 (2020).

[55] X. Sun, P. Wang, L. Xiong and Y. Pei. *Chem. Phys. Lett.*, **704**, 68 (2018).

[56] W. W. Xu, X. C. Zeng and Y. Gao. *Nanoscale*, **10**, 9476 (2018).

[57] R. Juarez-Mosqueda, S. Malola and H. Häkkinen. *Eur. Phys. J. D*, **73**, 1 (2019).

[58] M. F. Matus, S. Malola, E. K. Bonilla, B. M. Barngrover, C. M. Aikens and H. Häkkinen. *Chem. Commun.*, **56**, 8087 (2020).

[59] C. M. Crudden, J. H. Horton, I. I. Ebralidze, O. V. Zenkina, A. B. McLean, B. Drevniok, Z. She, H.-B. Kraatz, N. J. Mosey, T. Seki *et al. Nat. Chem.*, **6**, 409 (2014).

[60] P. Hohenberg and W. Kohn. *Phys. Rev.*, **136**, B864 (1964).

[61] W. Kohn and L. J. Sham. *Phys. Rev.*, **140**, A1133 (1965).

[62] J. P. Perdew, K. Burke and M. Ernzerhof. *Phys. Rev. Lett.*., **77**, 3865 (1996). doi:10.1103/PhysRevLett.77.3865. URL https://link.aps.org/doi/10.1103/PhysRevLett.77.386.

[63] M. Kuisma, J. Ojanen, J. Enkovaara and T. T. Rantala. *Phys. Rev. B*, **82**, 115106 (2010). doi:10.1103/PhysRevB.82.115106. URL https://link.aps.org/doi/10.1103/PhysRevB.82.115106.

[64] J. Wellendorff, K. T. Lundgaard, A. Møgelhøj, V. Petzold, D. D. Landis, J. K. Nørskov, T. Bligaard and K. W. Jacobsen. *Phys. Rev. B*, **85**, 235149 (2012).

[65] M. Kuisma, J. Ojanen, J. Enkovaara and T. T. Rantala. *Phys. Rev. B*, **82**, 115106 (2010).

[66] O. Gritsenko, R. van Leeuwen, E. van Lenthe and E. J. Baerends. *Phys. Rev. A*, **51**, 1944 (1995).

[67] J. P. Perdew, A. Ruzsinszky, G. I. Csonka, O. A. Vydrov, G. E. Scuseria, L. A. Constantin, X. Zhou and K. Burke. *Phys. Rev. Lett.*, **100**, 136406 (2008).

[68] F. Tran, S. Ehsan and P. Blaha. *Phys. Rev. Mater.*, **2**, 023802 (2018).

[69] J. P. Perdew and Y. Wang. *Phys. Rev. B*, **45**, 13244 (1992).

[70] L. E. M. Steinkasserer, S. Suhr and B. Paulus. *Phys. Rev. B*, **94**, 125444 (2016).

[71] K. Lee, É. D. Murray, L. Kong, B. I. Lundqvist and D. C. Langreth. *Phys. Rev. B*, **82**, 081101 (2010).

[72] E. Runge and E. K. U. Gross. *Phys. Rev. Lett..*, **52**, 997 (1984). doi:10.1103/PhysRevLett.52.997. URL https://link.aps.org/doi/10.1103/PhysRevLett.52.997.

[73] M. E. Casida. In *Recent Advances In Density Functional Methods: (Part I)*, pages 155–192. World Scientific (1995).

[74] M. E. Casida. *Theor. Comput. Chem.*, **4**, 391 (1996).

[75] F. Jensen. *Introduction to computational chemistry*. John wiley & sons (2017).

[76] C. J. Cramer. *Essentials of computational chemistry: theories and models*. John Wiley & Sons (2013).

[77] Z. Ma and P. G. Ranjith. *Fuel*, **255**, 115644 (2019).

[78] *GPAW Web page*. URL https://wiki.fysik.dtu.dk/gpaw/index.html.

[79] J. Enkovaara, C. Rostgaard, J. J. Mortensen, J. Chen, M. Dułak, L. Ferrighi, J. Gavnholt, C. Glinsvad, V. Haikola, H. Hansen *et al. J. Phys. Condens. Matter*, **22**, 253202 (2010).

[80] P. E. Blöchl. *Phys. Rev. B*, **50**, 17953 (1994).

[81] *ASE Web page*. URL https://wiki.fysik.dtu.dk/ase/about.html#about.

[82] R. Bader. *Press.: Oxford* (1990).

[83] *Bader Charge Analysis web page*. URL https://theory.cm.utexas.edu/henkelman/code/bader/.

[84] W. Tang, E. Sanville and G. Henkelman. *J. Phys. Condens. Matter*, **21**, 084204 (2009).

[85] G. Henkelman, A. Arnaldsson and H. Jónsson. *Comput. Mater. Sci.*, **36**, 354 (2006).

[86] S. Malola, L. Lehtovaara, J. Enkovaara and H. Hakkinen. *Acs Nano*, **7**, 10263 (2013).

[87] X. Andrade, S. Botti, M. A. Marques and A. Rubio. *J. Chem. Phys.*, **126**, 184106 (2007).

[88] V. Kellö and A. J. Sadlej. *Chem. Phys.*, **103**, 2991 (1995).

[89] O. Kostko, N. Morgner, M. Astruc Hoffmann and B. Von Issendorff. *Eur. Phys. J. D*, **34**, 133 (2005).

[90] M. De Santis, S. Rampino, L. Storchi, L. Belpassi and F. Tarantelli. *Inorg. Chem.*, **58**, 11716 (2019).

[91] R. H. Hertwig, W. Koch, D. Schröder, H. Schwarz, J. Hrušák and P. Schwerdtfeger. *J. Phys. Chem.*, **100**, 12253 (1996).

[92] A. Muñoz-Castro and H. R. Dias. *J. Comput. Chem.* (2022).

[93] C. Poggel and G. Frenking. *Chem. Eur. J.*, **24**, 11675 (2018).

[94] D. Roy, A. Pal and T. Pal. *RSC Adv.*, **12**, 12116 (2022).

[95] A. Muñoz-Castro. *Phys. Chem. Chem. Phys.*, **21**, 13022 (2019).

[96] J. Wei, J.-F. Halet, S. Kahlal, J.-Y. Saillard and A. Muñoz-Castro. *Inorg. Chem.*, **59**, 15240 (2020).

[97] N. N. Greenwood and A. Earnshaw. *Chemistry of the Elements*. Elsevier (2012).

[98] P. Pyykkö. In *Advances in quantum chemistry*, vol. 11, pages 353–409. Elsevier (1978).

[99] P. Pyykko. *Chem. Rev.*, **88**, 563 (1988).

[100] P. Pyykkö. *Annu. Rev. Phys. Chem.*, **63**, 45 (2012).

[101] M. Jansen. *Chem. Soc. Rev.*, **37**, 1826 (2008).

[102] P. Pyykkö. *Angew. Chem. Int. Ed.*, **43**, 4412 (2004).

[103] P. Pyykkö. *Chem. Soc. Rev.*, **37**, 1967 (2008).

[104] A. Das, U. Das and A. K. Das. *Coord. Chem. Rev.*, **479**, 215000 (2023).

[105] A. Muñoz-Castro, D. M. Carey and R. Arratia-Perez. *Polyhedron*, **197**, 115020 (2021).

[106] H. Shen, S. Xiang, Z. Xu, C. Liu, X. Li, C. Sun, S. Lin, B. K. Teo and N. Zheng. *Nano Res.*, **13**, 1908 (2020).

[107] W. Knight, K. Clemenger, W. A. de Heer, W. A. Saunders, M. Chou and M. L. Cohen. *Phys. Rev. Lett.*, **52**, 2141 (1984).

[108] S. Khanna and P. Jena. *Phys. Rev. B*, **51**, 13705 (1995).

[109] S. Khanna and P. Jena. *Chem. Phys. Lett.*, **219**, 479 (1994).

[110] W. A. De Heer. *Rev. Mod. Phys.*, **65**, 611 (1993).

[111] H. Häkkinen. *Chem. Soc. Rev.*, **37**, 1847 (2008).

[112] A. Fernando, K. D. M. Weerawardene, N. V. Karimova and C. M. Aikens. *Chem. Rev.*, **115**, 6112 (2015).

[113] B. Yoon, P. Koskinen, B. Huber, O. Kostko, B. von Issendorff, H. Häkkinen, M. Moseler and U. Landman. *ChemPhysChem*, **8**, 157 (2007).

[114] D. Schebarchov and N. Gaston. *Phys. Chem. Chem. Phys.*, **13**, 21109 (2011).

[115] S. Malola, S. Kaappa and H. Hakkinen. *J. Phys. Chem. C*, **123**, 20655 (2019).

[116] H. Shen, Z. Xu, M. S. A. Hazer, Q. Wu, J. Peng, R. Qin, S. Malola, B. K. Teo, H. Häkkinen and N. Zheng. *Angew. Chem.*, **133**, 3796 (2021).

[117] H. Shen, Q. Wu, M. S. A. Hazer, X. Tang, Y.-Z. Han, R. Qin, C. Ma, S. Malola, B. K. Teo, H. Häkkinen *et al. Chem*, **8**, 2380 (2022).

[118] P. Pyykkö. *Chem. Rev.*, **97**, 597 (1997).

[119] H. Schmidbaur and A. Schier. *Chem. Soc. Rev.*, **37**, 1931 (2008).

[120] H. Schmidbaur and A. Schier. *Chem. Soc. Rev.*, **41**, 370 (2012).

[121] Y. Ma, S. Bian, Y. Shi, X. Fan and X. Kong. *ACS omega*, **4**, 650 (2019).

[122] J. B. Patty, S. Havenridge, D. Tietje-Mckinney, M. A. Siegler, K. K. Singh, R. Hajy Hosseini, M. Ghabin, C. M. Aikens and A. Das. *J. Am. Chem. Soc.*, **144**, 478 (2021).

[123] K. Salorinne, R. W. Man, P. A. Lummis, M. S. A. Hazer, S. Malola, J. C.-H. Yim, A. J. Veinot, W. Zhou, H. Häkkinen, M. Nambo *et al. Chem. Commun.*, **56**, 6102 (2020).

[124] A. Pihlajamaki, J. Hamalainen, J. Linja, P. Nieminen, S. Malola, T. Karkkainen and H. Hakkinen. *J. Phys. Chem. A .*, **124**, 4827 (2020).

[125] J. Li, T. Chen, K. Lim, L. Chen, S. A. Khan, J. Xie and X. Wang. *Adv. Intell. Syst.*, **1**, 1900029 (2019).

[126] C. Zeni, K. Rossi, A. Glielmo and F. Baletto. *Advances in Physics: X*, **4**, 1654919 (2019).

[127] D. E. Jones, H. Ghandehari and J. C. Facelli. *Comput Methods Programs Biomed*, **132**, 93 (2016).

[128] M. F. Matus and H. Häkkinen. *Nat. Rev. Mater.*, pages 1–18 (2023).

ORIGINAL PAPERS

PI

METAL-LIGAND BOND IN COMPLEXES AND CLUSTERS OF CU, AG, AND AU, WITH THIOLATES, PHOSPHINES, AND N-HETEROCYCLIC CARBENES

by

Maryam Sabooni Asre Hazer, Sami Malola and Hannu Hakkinen

Unsubmitted manuscript

Request a copy from author.

PII

NHC-STABILIZED AU_{10} NANOCLUSTERS AND THEIR CONVERSION TO AU_{25} NANOCLUSTERS

by

Paul A. Lummis, Kimberly M. Osten, Tetyana I. Levchenko, **Maryam Sabooni Asre Hazer**, Sami Malola, Bryan Owens-Baird, Alex J. Veinot, Emily L. Albright, Gabriele Schatte, Shinjiro Takano, Kirill Kovnir, Kevin G. Stamplecoskie, Tatsuya Tsukuda, Hannu Hakkinen, Masakazu Nambo, and Cathleen M. Crudden (2022)

J. Am. Chem. Soc. Au, **2(4)**, 875-885

https://doi.org/10.1021/jacsau.2c00004

JACS Au
AN OPEN ACCESS JOURNAL OF THE AMERICAN CHEMICAL SOCIETY

pubs.acs.org/jacsau Article

NHC-Stabilized Au_{10} Nanoclusters and Their Conversion to Au_{25} Nanoclusters

Paul A. Lummis,[▽] Kimberly M. Osten,[▽] Tetyana I. Levchenko,[▽] Maryam Sabooni Asre Hazer, Sami Malola, Bryan Owens-Baird, Alex J. Veinot, Emily L. Albright, Gabriele Schatte, Shinjiro Takano, Kirill Kovnir,* Kevin G. Stamplecoskie,* Tatsuya Tsukuda,* Hannu Häkkinen,* Masakazu Nambo,* and Cathleen M. Crudden*

Cite This: *JACS Au* 2022, 2, 875–885 Read Online

ACCESS | Metrics & More | Article Recommendations | Supporting Information

ABSTRACT: Herein, we describe the synthesis of a toroidal Au_{10} cluster stabilized by *N*-heterocyclic carbene and halide ligands *via* reduction of the corresponding NHC−Au−X complexes (X = Cl, Br, I). The significant effect of the halide ligands on the formation, stability, and further conversions of these clusters is presented. While solutions of the chloride derivatives of Au_{10} show no change even upon heating, the bromide derivative readily undergoes conversion to form a biicosahedral Au_{25} cluster at room temperature. For the iodide derivative, the formation of a significant amount of Au_{25} was observed even upon the reduction of NHC−Au−I. The isolated bromide derivative of the Au_{25} cluster displays a relatively high (*ca.* 15%) photoluminescence quantum yield, attributed to the high rigidity of the cluster, which is enforced by multiple CH−π interactions within the molecular structure. Density functional theory computations are used to characterize the electronic structure and optical absorption of the Au_{10} cluster. ^{13}C-Labeling is employed to assist with characterization of the products and to observe their conversions by NMR spectroscopy.

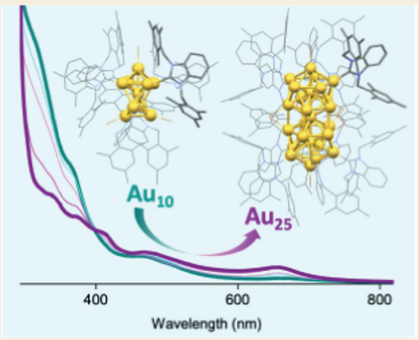

KEYWORDS: *gold, N-heterocyclic carbenes, metal nanoclusters, nanocluster interconversion, density functional theory calculations, NMR analysis, ^{13}C-labeling, photoluminescence*

INTRODUCTION

N-Heterocyclic carbenes (NHCs) are widely employed ligands in transition-metal and main-group chemistry[1−3] and have recently attracted interest in materials chemistry,[4] providing robust monolayers on planar gold surfaces[5−8] and nanoparticles.[9−15] Known NHC-stabilized gold nanoclusters are predominantly smaller Au_{11} or Au_{13} species,[16−20] however, Au_{23} and Au_{44} cores have also been reported for mixed-ligand systems.[21,22] Despite the high prevalence of Au_{25} cores in thiolate-stabilized clusters, there is only one example of this cluster size for NHC-stabilized systems.[23]

Our group recently reported that the reduction of NHC−Au−X complexes resulted in a series of icosahedral Au_{13} clusters (Figure 1) when benzylic groups on the NHC nitrogens of substituted benzimidazole were employed.[17] Although a range of benzylic substituents was tolerated, increasing the steric size of the substituents led to a decrease in the yield of the target Au_{13} clusters, and the formation of polydisperse cluster mixtures. It was surprising then that the use of an NHC ligand with even more sterically hindered 2,4,6-trimethylbenzyl (from here on, $MesCH_2$) wingtip groups gave well-defined cluster species, specifically an Au_{10} cluster with a toroidal core. Subsequent conversion of Au_{10} to a biicosahedral Au_{25} cluster strongly depends on the nature of the halide employed.

Herein, we document the synthesis of these Au_{10} and Au_{25} clusters and provide evidence that small, isolable clusters are precursors to the formation of larger clusters. The extreme effect that seemingly innocent counterions have on the conversion of Au_{10} to Au_{25} is also described, along with the effect of the solvent. The use of ^{13}C labeling on the carbene carbon provides unprecedented insight into the transformation.

RESULTS AND DISCUSSION

Synthesis and Characterization of Au_{10} Nanoclusters

Molecular gold complexes ^{MesCH2}BimyAuX **2a−c** (X = Cl, Br, I) were synthesized from the corresponding benzimidazolium

Received: January 3, 2022
Revised: February 15, 2022
Accepted: March 4, 2022
Published: April 6, 2022

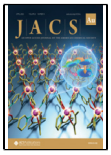

https://doi.org/10.1021/jacsau.2c00004
JACS Au 2022, 2, 875−885

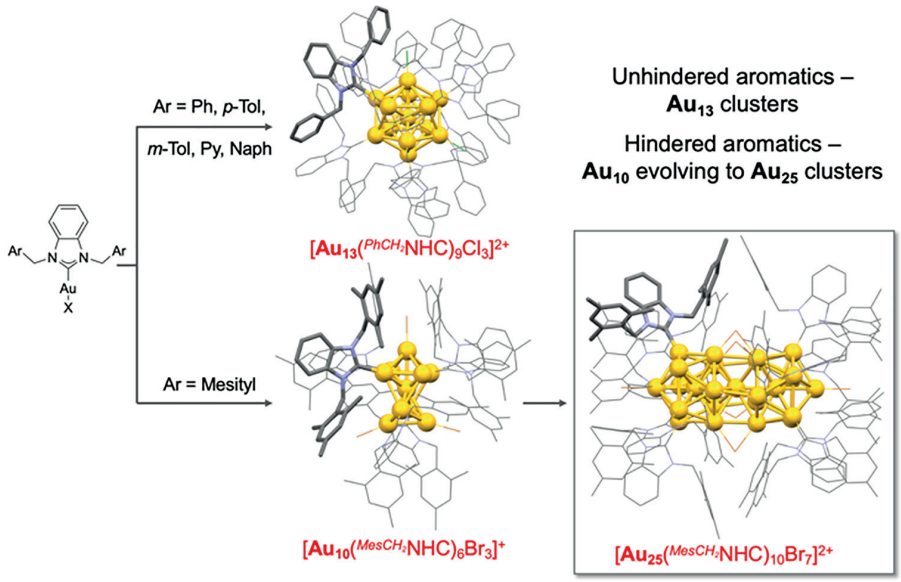

Figure 1. Synthesis of NHC-stabilized Au nanoclusters by direct reduction of NHC−Au−X complexes.

salts **1a−b** *via* established procedures[24,25] (see the SI for details). The reduction of these complexes was carried out with $NaBH_4$ at room temperature (Figure 2A). In all cases, UV−vis absorbance spectroscopy revealed the presence of cluster species with absorbance profiles notably different from previously reported Au_{13} clusters.[17] For instance, in the case of **2b** (X = Br), the reaction mixture after 12−20 h at room temperature shows distinct absorbance bands at ∼320, 368, and 470 nm (Figure S2). Analysis of the crude reaction mixture by electrospray ionization mass spectrometry (ESI-MS; Figure S3) identified the major cluster species to be $[Au_{10}(^{MesCH2}Bimy)_6Br_3]^+$ ($[\mathbf{3b}]^+$). The reaction times for the formation of Au_{10} clusters as well as the composition of the crude reaction mixtures depended on the halide employed but all ^{MesCH2}BimyAuX precursors produced $[Au_{10}(^{MesCH2}Bimy)_6X_3]X$ clusters (**3a**, X = Cl; **3b**, X = Br; **3c**, X = I). *In situ* monitoring of the reduction of **2b** by UV−vis absorbance spectroscopy at short reaction times (<6 h) showed intermediate gold species with absorbance bands at ∼325, 424, and 532 nm (Figures S11 and 12). Due to their transient nature, these species could not be unequivocally identified by ESI-MS and NMR spectroscopy (Figures S13 and 14). At longer reaction times, these intermediate species converted to [**3b**]Br.

Clusters [**3a**]Cl and [**3b**]Br were purified by column chromatography, recrystallization, and anion exchange with NH_4PF_6 (see the SI for details). ESI-MS of [**3b**][PF_6] shows a dominant molecular ion peak at 4504.9 m/z corresponding to $[Au_{10}(^{MesCH2}Bimy)_6Br_3]^+$ (Figure 2B). Good agreement was observed between the experimental and theoretical isotope distribution patterns. A minor peak at 4460.0 m/z was also observed in the cluster region; this peak was attributed to exchange species $[Au_{10}(^{MesCH2}Bimy)_6Br_2Cl]^+$, most likely formed by halide exchange during ionization. UV−vis absorbance profiles of purified clusters [**3a**][PF_6] (Figure S67) and [**3b**][PF_6] (Figure 2C) are largely the same, although the exact band positions and intensities were found to be dependent on the halide. Halogen effects on optical properties are consistent with previous observations with phosphine-stabilized Au nanoclusters;[26] however, a dramatic difference in the reactivity of gold clusters depending on the halide present has not been previously reported, to the best of our knowledge. In our experiments, iodide cluster [**3c**]I proved to be difficult to isolate in high purity due to its facile conversion to other clusters (*vide infra*), and [**3c**]I was therefore only partially characterized (Figures S6−8 and S15).

X-ray quality single crystals of the triflate salt [**3b**][OTf] were characterized by single-crystal X-ray crystallography. The solid-state structure (Figure 3) reveals a toroidal Au_{10} core similar to $[Au_{10}(PCy_2Ph)_6Cl_3][NO_3]$ reported by Mingos et al.[27] but $[\mathbf{3b}]^+$ has a different arrangement of halide ligands. Cluster $[\mathbf{3b}]^+$ has pseudo C_{2V} symmetry, with two $Au_3(NHC)_3$ rings capping either side of a planar Au_4Br_3 core. The Au−Au distances range from 2.6271(9) Å to 2.936(1) Å, with the average radial Au−Au bonds being shorter than the average peripheral Au−Au separations (2.700 and 2.832 Å, respectively; see Table S7 for summarized data). Au−C bond lengths are between 2.026(9) Å and 2.041(9) Å (average 2.034 Å; Table S7), which is slightly shorter compared with Au−C_{NHC} bond lengths in previously reported NHC-stabilized gold nanoclusters.[17−20,23]

The cluster core of $[\mathbf{3b}]^+$ is relatively more open than in previously reported NHC-stabilized gold nanoclusters: unlike Au_{13} and Au_{11}, $[\mathbf{3b}]^+$ does not have any inner gold sites. Moreover, the gold atom at the central site of $[\mathbf{3b}]^+$ is not bonded to NHC or halide ligands, which makes $[\mathbf{3b}]^+$ potentially more reactive.

Synthesis and Characterization of Au_{25} Nanoclusters

Although [**3b**]Br is sufficiently stable to survive column chromatography, its solutions in ethanol change color over time, which prompted us to investigate whether a new cluster was being formed. As expected, the UV−vis absorbance spectra reflect this change, most notably through the appearance of a new band at 658 nm (Figure S16). ESI-MS analysis identified $[Au_{25}(^{MesCH2}Bimy)_{10}Br_7]^{2+}$ ($[\mathbf{4b}]^{2+}$) as the new cluster species. This formulation is similar to an Au_{25} cluster stabilized by ^{iPr}Bimy NHCs reported by Zheng et al.,[23] in which five

https://doi.org/10.1021/jacsau.2c00004
JACS Au 2022, 2, 875−885

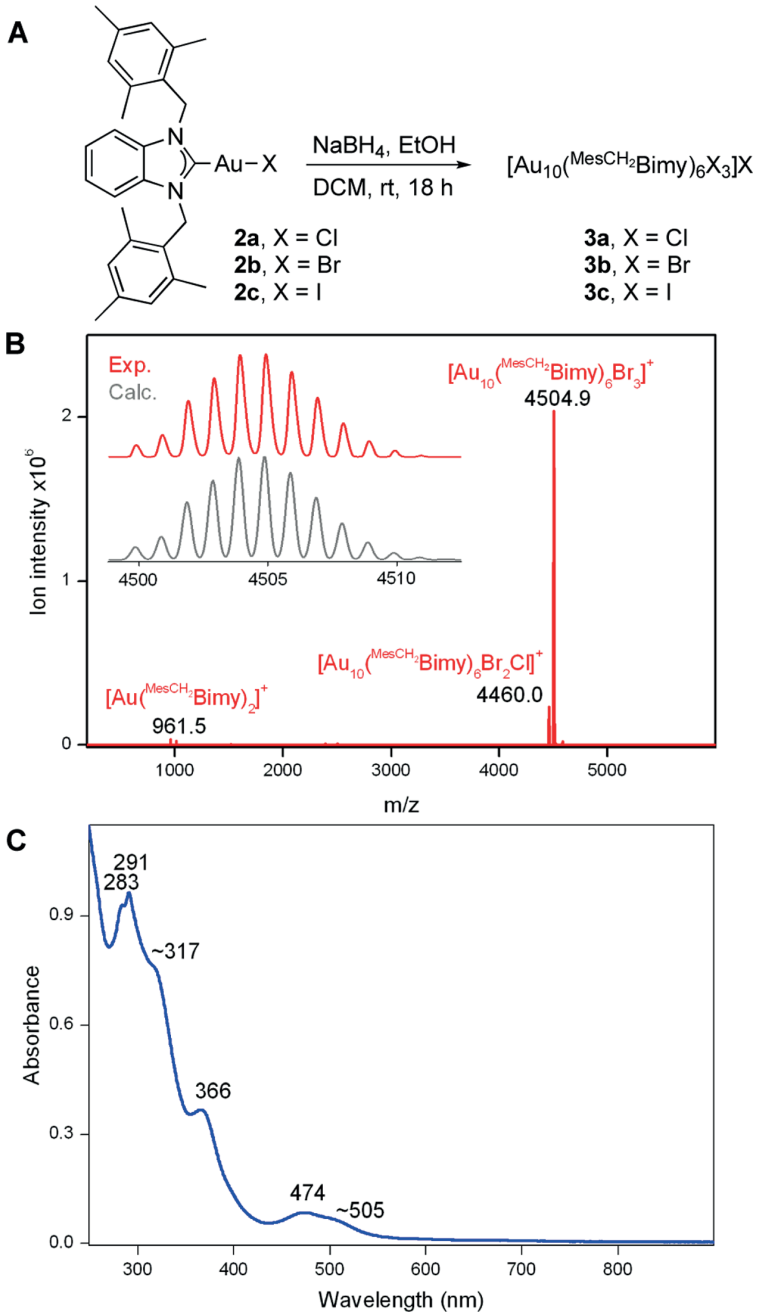

Figure 2. (A) Preparation of Au_{10} clusters **3a−c**; (B) ESI-MS of [**3b**][PF_6]; and (C) UV−vis absorbance spectrum of [**3b**][PF_6] in dichloromethane.

bridging bromide ligands link two Au_{13} icosahedra with a shared central atom. In Zheng's report, the Au_{25} cluster was the result of prolonged treatment of a molecular gold precursor without the observation of intermediate cluster species.

Purification of cluster [**4b**]$^{2+}$ could be achieved by anion exchange with NH_4PF_6 followed by column chromatography (see the SI for details). In the ESI-MS of [**4b**][PF_6]$_2$ (Figure 4B), the dominant molecular ion peak at 4654.5 m/z shows good agreement with the theoretical isotope distribution pattern of $[Au_{25}(^{MesCH2}Bimy)_{10}Br_7]^{2+}$. Trace amounts of $[Au_{25}(^{MesCH2}Bimy)_{10}Br_6Cl]^{2+}$ (see the small peak at 4632.1 on Figure 4B) were also observed, consistent with Br/Cl exchange.[28] The main UV−vis absorbance bands of [**4b**]-[PF_6]$_2$ were found at 325, 338, 377, 413, 467 (with a shoulder at ∼510), and 658 nm (Figure 4C).

Though the conversion of one metal nanoclusters to another is common, reports on such transformations involving biicosahedral M_{25} nanoclusters are scarce. A few publications describe the preparation of phosphine/thiolate or phosphine/halide stabilized biicosahedral M_{25} nanoclusters by conversion from other species, such as a mixture of gold nanoparticles,[29−32] spherical M_{25} clusters,[33] and smaller Au_{11}

https://doi.org/10.1021/jacsau.2c00004
JACS Au 2022, 2, 875−885

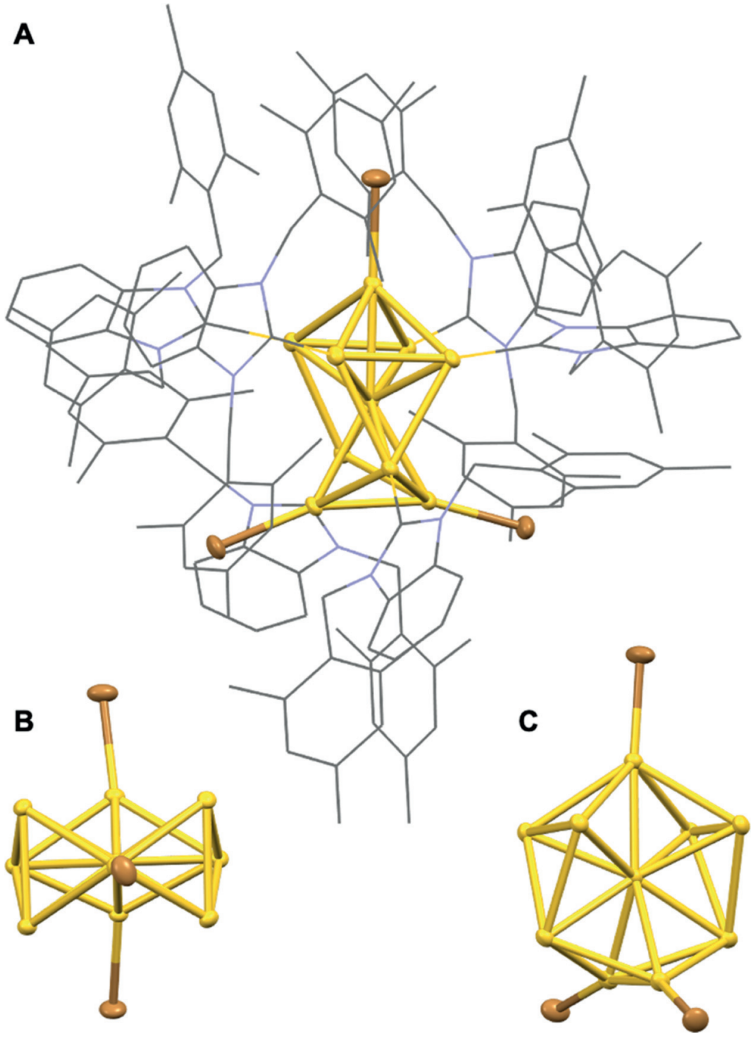

Figure 3. (A) Molecular structure of [**3b**][OTf] with thermal ellipsoids drawn at the 50% probability level. Hydrogen atoms and anions have been omitted, and NHCs are shown as a wireframe for increased clarity. (B, C) Alternative view of the $[\mathbf{3b}]^+$ core with bromide ligands only. Color key: Yellow = Au, Orange = Br, Gray = C, Blue = N.

nanoclusters.[34] In all of these cases, there was a specific trigger for the transformations of the metal core, for example, the addition of different ligands.[31,32] Seemingly triggerless conversion of otherwise stable Au_{10} into biicosahedral Au_{25} is unprecedented. This prompted us to look into details of the Au_{10} to Au_{25} conversion.

Kinetics of Au_{10} to Au_{25} Conversion in Solution

To probe the conversion of Au_{10} to Au_{25} clusters, we leveraged the differences in the UV−vis absorbance spectra of the two species to monitor reaction progress over time. Specifically, we tracked the increase in the absorbance of the Au_{25} characteristic band at 658 nm (Figure 5). It was found that the conversion of [**3b**]Br is solvent dependent, occurring readily in protic or mildly acidic solvents such as alcohols (methanol, ethanol) or chloroform, but not in other solvents examined such as dichloromethane or tetrahydrofuran (THF) (Figure S16). The conversion rate for [**3b**]Br depends on its concentration, temperature, and the nature of the solvent. At room temperature in alcohol solvents, over a week is required to reach an appreciable concentration of Au_{25}, while the same conversion takes only 2 days at 55 °C in methanol. The conversion is the fastest in chloroform at 55 °C, taking only hours (Figure 5).[35] Unfortunately, in chloroform, this conversion is accompanied by the formation of unidentifiable byproducts, which complicated attempts at quantitative kinetic experiments.

To confirm the results obtained by UV−vis absorbance spectroscopy and gain insight into the mechanism of Au_{25} formation, conversion of [**3b**]Br was also monitored by ESI-MS and NMR spectroscopy (Figures S19−S21). Similar trends were also observed using these techniques. In particular, the conversion was faster in chloroform compared to methanol, as monitored by NMR spectroscopy (Figures S20−S21). Note that no intermediate cluster species were observed by ESI-MS while monitoring the conversion of Au_{10} to Au_{25} (Figure S19), and therefore, greater detail concerning the mechanism for this conversion could not be obtained using this method.

The nature of the outer sphere anion also has a significant effect on the rate of conversion. Cluster [**3b**][PF_6] shows only partial conversion after 20 h at 60 °C in methanol,[36] while

https://doi.org/10.1021/jacsau.2c00004
JACS Au 2022, 2, 875−885

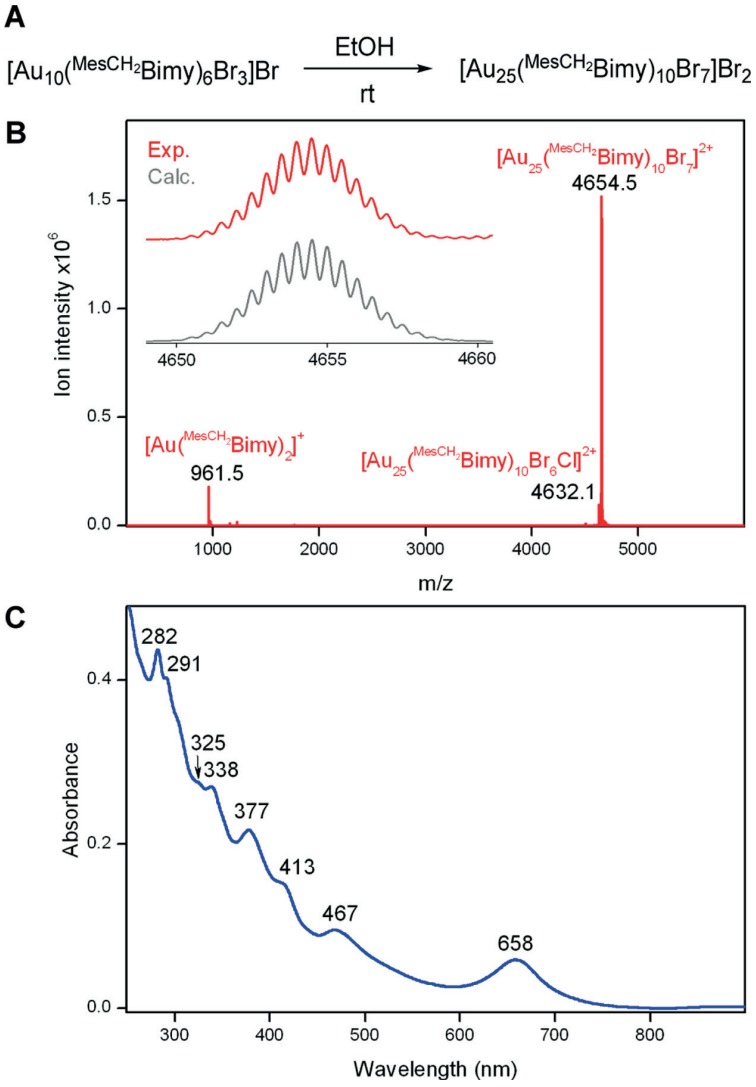

Figure 4. (A) Preparation of Au_{25} cluster [**4b**]Br_2; (B) ESI-MS of [**4b**][PF_6]$_2$; and (C) UV−vis absorbance spectrum of [**4b**][PF_6]$_2$ in dichloromethane.

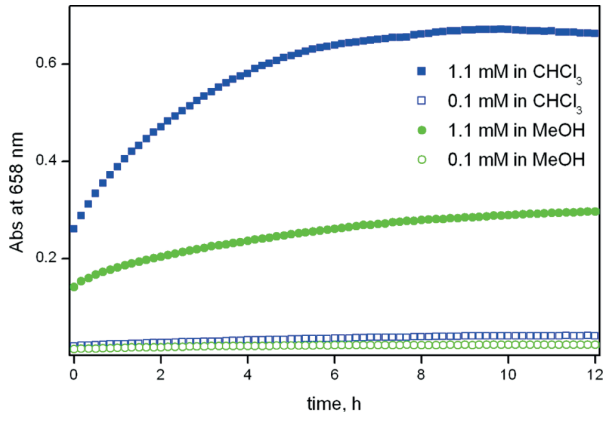

Figure 5. Conversion of [**3b**]Br in chloroform (blue) and methanol (green) at 55 °C, monitored *in situ* by the change in absorbance at 658 nm over time.

under the same conditions [**3b**]Br converts significantly to Au_{25}, as observed by UV−vis absorbance and NMR spectroscopy, and ESI-MS (Figures S17−21). Inner sphere halides also have a significant effect. For example, the Au_{10} cluster with chloride ligands [**3a**]Cl showed no evidence of conversion to Au_{25} even after several weeks in ethanol at room temperature or with heating at 60 °C in methanol. By contrast, the bromide derivative [**3b**]Br is readily converted to Au_{25} clusters [**4b**]$^{2+}$ in specific solvents, and iodide cluster [**3c**]I gave significant amounts of Au_{25} clusters [**4c**]$^{2+}$ even during the reduction of **2c** (Figure S15). Attempts to isolate pure samples of [**3c**]I *via* the established methods for [**3b**]Br also led to the isolation of a significant amount of [**4c**]$^{2+}$ without the need for further conversion, although instability of [**4c**]$^{2+}$ prevented full purification and characterization (Figures S6−8). These results demonstrate the pivotal role not only of the outer sphere counterions but also of the ligated halide ligands in cluster conversion from Au_{10} to Au_{25} and the overall stability of the clusters. Our observations agree with the previous reports that

https://doi.org/10.1021/jacsau.2c00004
JACS Au 2022, 2, 875−885

halides can affect the growth and conversions of metal nanoclusters.[37−39]

Structural Characterization of Au_{25} Clusters in the Solid State

In an early attempt to isolate pure Au_{25} cluster $[\mathbf{4b}]^{2+}$ for structural characterization, [**3b**]Br was dissolved in ethanol and kept at room temperature for 7 days. Purification by dialysis and anion exchange with $K[B(C_6F_5)_4]$ led to the isolation of crystals of a closely related cluster $[Au_{25}(^{MesCH2}Bimy)_{10}Br_8][B(C_6F_5)_4]$ ($[\mathbf{5b}]^+$, Figure 6). This cluster closely resembles

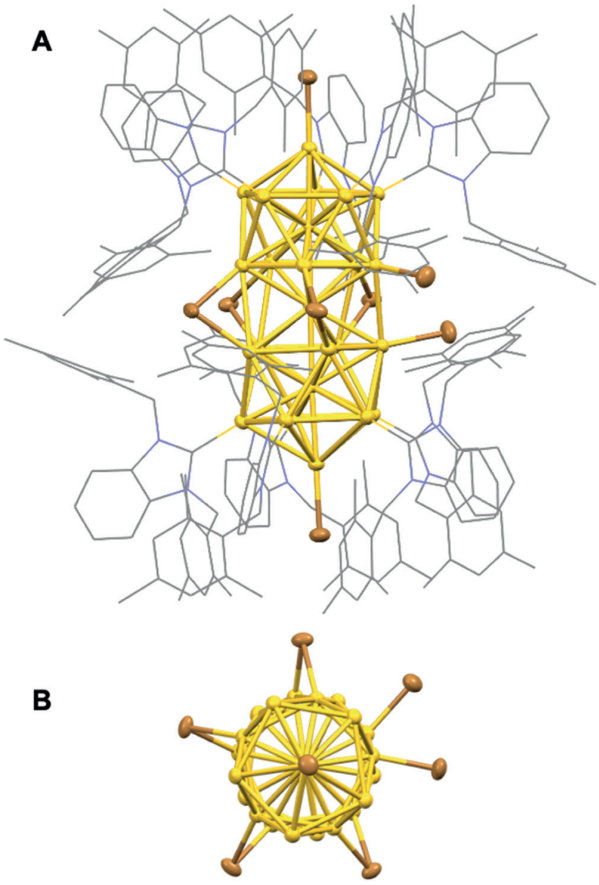

Figure 6. (A) Molecular structure of $[\mathbf{5b}][B(C_6F_5)_4]$ with thermal ellipsoids drawn at the 50% probability level. Hydrogen atoms and anions have been omitted, and NHCs are shown as a wireframe for increased clarity. (B) Alternative view of the $[\mathbf{5b}]^+$ core with bromide ligands only. Color key: Yellow = Au, Orange = Br, Gray = C, Blue = N.

$\mathbf{4b}^{2+}$ with the exception of having an additional inner sphere bromide ligand and therefore only a +1 charge. The parent mass peak for $[\mathbf{5b}]^+$ could not be observed by ESI-MS, with the sample showing only a peak for $[\mathbf{4b}]^{2+}$, likely due to the facile loss of one bromide ligand on the core during ionization.

X-Ray crystallographic analysis indicated that $[\mathbf{5b}]^+$ features a twisted biicosahedral structure where the two central Au_5 pentagons making up the core of the structure are in a partially staggered orientation. The structure also features four bridging and two terminal bromide ligands connecting the two central Au_5 pentagons, instead of the expected symmetric five bridging bromide ligands (Figures 6B and S63). The Au−Br bond distances at the waist sites are in the range of 2.5316(8) Å—2.5794(7) Å for the doubly bridging bromides and 2.455(1) Å—2.4609(9) Å for the terminal ones. The latter distances are slightly shorter compared with the terminal Au−Br bond distances at the vertex sites (2.4706(9) Å—2.4718(9) Å; see Table S8 for summarized data). The co-existence of different (*i.e.*, bridging and terminal) metal-halide connection modes at the waist sites of biicosahedral nanoclusters is extremely rare; it was reported only once for related phosphine/ halide-ligated AgAu bimetallic M_{25} clusters by Huang et al.[40]

Subsequently, we established an optimized procedure for the isolation and purification of the Au_{25} cluster, specifically, the conversion of [**3b**]Br in methanol at 60 °C, followed by anion exchange of the crude mixture with excess NH_4PF_6 and purification by column chromatography (see details in the SI). We note that the anion exchange was used here to facilitate purification, though later we discovered that anions may also play role in transformations between $[\mathbf{5b}]^+$ and $[\mathbf{4b}]^{2+}$ (*vide infra*). We were successful in growing crystals of $[\mathbf{4b}][B(C_6F_5)_4]_2$ from Au_{25} clusters isolated *via* this route, after anion exchange with the borate anion. The solid-state structure (Figure 7) shows the expected Au_{25} core structure with five symmetric bridging bromide ligands and not six as for $[\mathbf{5b}]^+$.

The two central Au_5 pentagons are slightly twisted from an eclipsed orientation, although less than that in $[\mathbf{5b}]^+$, most likely due to the steric constraints of the bulky mesityl substituents. Structures with five bridging halides and different degrees of rotation of the vertex-sharing icosahedra had been reported for related phosphine/halide-ligated heterometallic M_{25} nanoclusters[41−44] and, more recently, for an NHC/halide-ligated Au_{25} nanocluster.[23] In particular, $[Au_{25}(^{iPr}Bimy)_{10}Br_7]^{2+}$ (bearing significantly less bulky *i*Pr wingtip groups as compared with $MesCH_2$ in $[\mathbf{4b}]^{2+}$) was reported to have an eclipsed configuration of two icosahedra;[23] this nanocluster conforms to idealized D_{5h} symmetry with somewhat shorter icosahedron−icosahedron separations than in $[\mathbf{4b}]^{2+}$ (see Table S8). Of note, the asymmetric unit contains two molecules of $[\mathbf{4b}]^{2+}$ and three $[B(C_6F_5)_4]^-$ counterions. The fourth counterion was not resolved; this $[B(C_6F_5)_4]^-$ counterion is likely significantly disordered due to the large solvent accessible void in the unit cell (see Figure S65).

The fact that the Au_{10} cluster with chloride ligands [**3a**]Cl showed no conversion to Au_{25} (while [**3b**]Br and [**3c**]I convert readily) may be explained both by the steric environment imposed by the bulky mesityl-substituted NHC ligand, as well as steric and electronic factors introduced by the smaller chloride ligands. Though multiple examples of phosphine, thiolate, or NHC-protected gold clusters with halides as co-ligands have been reported, chlorides are commonly found terminally bound to gold, and clusters with Au−Cl bridging bonds are extremely rare.[45,46]

Structural Characterization of Au_{10} and Au_{25} Clusters in Solution by NMR Spectroscopy

To further probe the reactivity and structures of $[\mathbf{3b}]^+$ and $[\mathbf{4b}]^{2+}/[\mathbf{5b}]^+$ in solution,^{13}C(2)-labeled benzimidazolium salt **1b*** was synthesized and used to prepare the corresponding ^{13}C-labeled gold complex **2b*** and cluster $[\mathbf{3b^*}]X$ (see the SI for details). The $^{13}C\{^1H\}$ NMR spectrum of labeled $[\mathbf{3b^*}]X$ (X = Br or PF_6) has two carbene peaks at 200.7 and 214.9 ppm in a 2:1 ratio, respectively, as expected from the two different ligand environments predicted from the solid-state structure of the Au_{10} clusters (Figure 8A; see Figure S45 for full-spectrum

https://doi.org/10.1021/jacsau.2c00004
JACS Au 2022, 2, 875−885

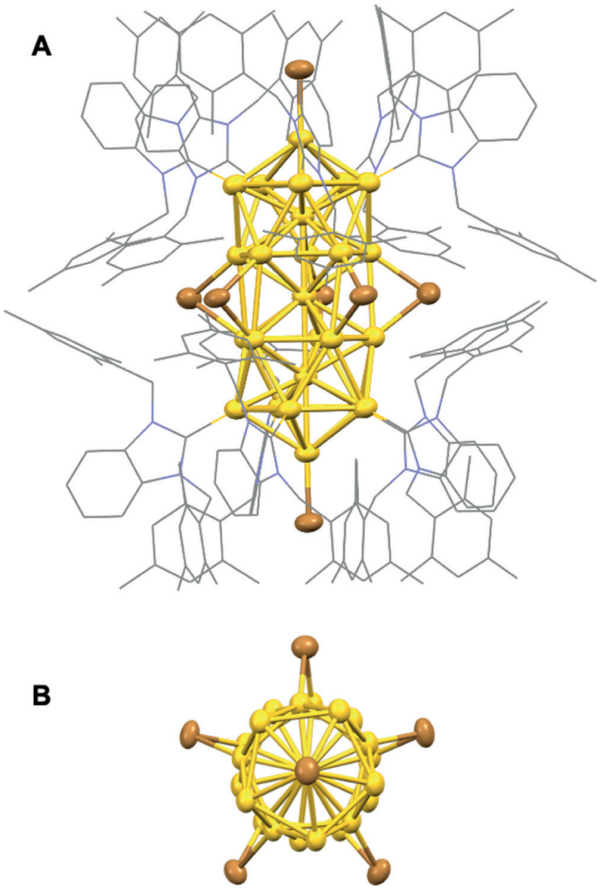

Figure 7. (A) Molecular structure of [**4b**][$B(C_6F_5)_4$]$_2$ with thermal ellipsoids drawn at the 50% probability level. Hydrogen atoms and anions have been omitted, and NHCs are shown as a wireframe for increased clarity. The asymmetric unit has two cluster molecules; only one is shown for clarity. (B) Alternative view of the [**4b**]$^{2+}$ core with bromide ligands only. Color key: Yellow = Au, Orange = Br, Gray = C, Blue = N.

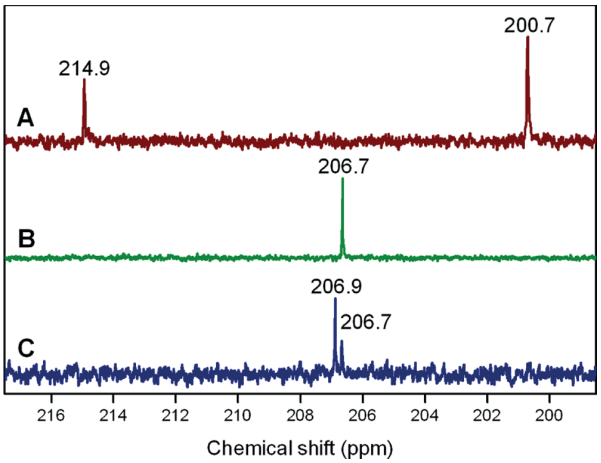

Figure 8. $^{13}C\{^1H\}$ NMR spectra (600 MHz, CD_2Cl_2) of (A) ^{13}C-labeled [**3b***][PF_6]; (B) column-purified [**4b***][PF_6]$_2$, and (C) crude reaction mixture from conversion of [**3b***]Br in MeOH at 60 °C for 4 days.

and Figure S56 for assignment). The ^1H NMR spectrum of [**3b***]X (Figure S44) is also in agreement with this structure and is consistent with the nonlabeled cluster (Figure S40), showing only minor broadening of the benzylic proton peaks, in contrast to the diastereotopic benzylic proton peaks observed in the spectra of related Au_{13} clusters.[17]

Conversion of [**3b***]Br in methanol or $CHCl_3$ at 60 °C, followed by exchange with NH_4PF_6 and purification by column chromatography led to the isolation of a major cluster species with only one carbene peak in the $^{13}C\{^1H\}$ NMR spectrum at 206.7 ppm (Figures 8B and S47). The ^1H NMR spectrum (Figure S46) is consistent with the NMR spectrum of the isolated crystals of [**4b**][$B(C_6F_5)_4$]$_2$ as well as nonlabeled Au_{25} clusters isolated by NH_4PF_6 exchange and column chromatography, and shows a single, albeit asymmetric, ligand environment, due to the fixed arrangement of the ligands across the cluster (see Figures S57 and S58 for assignment). For example, six distinct methyl resonances can be found for the mesityl groups (Figure S46). Due to the expected symmetry of the ten ligands in cluster [**4b**]$^{2+}$, as well as the consistency of the NMR and other spectroscopic data with the crystals isolated for [**4b**][$B(C_6F_5)_4$]$_2$ we assign this species as [**4b***][PF_6]$_2$ (see the SI for full characterization data).

To obtain more insight into the conversion of Au_{10} to Au_{25}, and the possible distinction between clusters [**4b**]$^{2+}$ and [**5b**]$^+$ in solution, we monitored the conversion of [**3b***]X under various conditions by NMR spectroscopy. In crude samples, we can indeed confirm the presence of two major sets of cluster ligand peaks by ^1H NMR spectroscopy, in addition to the expected gold complex byproducts (^{MesCH2}Bimy)AuX and [(^{MesCH2}Bimy)$_2$Au]X. In particular, a second set of six methyl resonances distinct from those confirmed to be [**4b**]$^{2+}$ is evident in the reaction mixtures before anion exchange and purification (Figure S22), along with a second carbene signal in the $^{13}C\{^1H\}$ NMR spectra of ^{13}C-labeled samples at 206.9 ppm (Figures 8C and S23). It also appears that this species is either converted to [**4b**]$^{2+}$ or decomposed during anion exchange and/or column purification.

Interestingly, the ^1H NMR spectrum of a pure sample of [**4b**][PF_6]$_2$ in the presence of excess tetrabutylammonium bromide showed mostly this second set of signals in dichloromethane-*d2* (see Figures S22 and 23), suggesting that it exists in this form in the presence of excess bromide ions. Although the asymmetry of the solid-state structure of [**5b**]$^+$ would suggest the presence of multiple carbene signals for this cluster, similar phosphine ligated AgAu bimetallic M_{25} clusters with six bridging halides have been found to exhibit only a single ligand environment in solution by NMR spectroscopy.[47] It is difficult to confirm the assignment of this species as [**5b**]$^+$, as the parent mass peak cannot be observed by ESI-MS likely due to facile loss of one bromide ligand on the core during ionization, and unfortunately the crystal yield of [**5b**][$B(C_6F_5)_4$] was not high enough for detailed NMR studies. However, these NMR studies confirm that multiple cluster species, likely the two Au_{25} clusters characterized in the solid-state, are generated from the conversion of Au_{10}, with [**4b**]X_2 appearing to be the dominant structure isolated after purification in most cases.

Theoretical Calculations

The electronic structure of [**3b**]$^+$ was investigated by density functional theory (DFT) using experimental coordinates as a starting point (see the SI for technical details of the DFT

https://doi.org/10.1021/jacsau.2c00004
JACS Au 2022, 2, 875−885

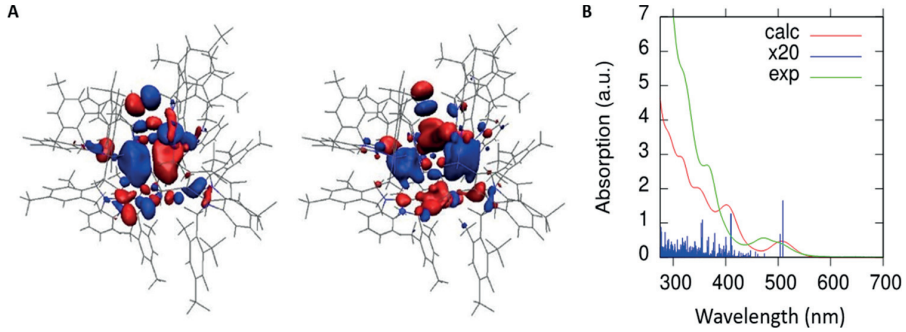

Figure 9. (A) HOMO (left) and LUMO (right) orbitals of $[\mathbf{3b}]^+$ and (B) calculated (red) and measured (green) UV−vis spectrum of $[\mathbf{3b}]^+$.

calculations and analysis). We used the real-space GPAW code[48] and optimized the structure with the Perdew−Burke−Ernzerhof (PBE)[49] exchange−correlation (xc) functional to describe the electron−electron interactions. The PBE-optimized structure of $[\mathbf{3b}]^+$ in the gas phase is shown in Figure S74 and compared to the crystal structure in Table S9. We see that the gas-phase model overestimates the Au−Au bonds by 2−5%, Au−Br bonds by 2%, and Au−C bonds by 2% while keeping the overall symmetry unchanged.

This behavior is similar to what we have found previously for NHC-stabilized Au clusters,[16,17,23] and we consider it an acceptable compromise between numerical efficiency and accuracy. We note that the use of the gas-phase model for $[\mathbf{3b}]^+$ itself may account partially for the small structural discrepancies between the experiment and theory, regardless of the used xc functional, due to omission of effects from counterions and crystal packing.

To study the symmetry of the frontier orbitals and the magnitude of the HOMO−LUMO energy gap, we also employed the GLLB-SC xc functional, which was originally developed to improve the band gap of semiconductor materials.[50] Figure S75 compares the electronic density of states calculated both from the PBE functional and the GLLB-SC functional for the PBE-optimized cluster structure. Both functionals yield similar symmetries for the frontier orbitals, with the HOMO and HOMO−1 orbitals being of $T1_u$ (spherical P-symmetry), as expected for a cluster with 6 "superatom" electrons,[51] while the LUMO orbital has an e_g (D) symmetry (Figures 9A and S76). GLLB-SC yields a significantly larger energy gap as compared to PBE (2.26 and 1.98 eV, respectively). The larger gap is consistent with the measured optical band gap as discussed later. For this reason, we performed further analyzes of the electronic structure and optical properties using the GLLB-SC functional.

Bader charge analysis (Table S10) reveals that the central Au atom in the cluster is slightly negatively charged, while the Au atoms in contact with the ligands are close to neutral. Bromines are clearly electron-withdrawing ligands (−0.49 e per Br), as expected, and the NHC ligands act as weak electron donors (0.45 e per ligand) to balance the total charge to +1.

The calculated UV−vis absorbance spectrum of the gas-phase model of $[\mathbf{3b}]^+$ is compared to the experimental data recorded in dichloromethane (Figure 9B). The first experimental absorption peak observed at around 505 nm as well as the experimental optical band gap at around 550 nm (2.25 eV) are reproduced well by the theory. The computations predict two distinct optical absorptions at the band edge (see the blue sticks in Figure 9B) that are likely to split to a larger degree in terms of energy at finite temperature due to atom dynamics. This explains the broader asymmetric first feature (two merging peaks) observed in the experiment. The third and fourth peaks (at 366 and 317 nm, respectively) in the experimental spectrum are reproduced well by the theory. We analyzed the four peaks in the computed spectrum by decomposing them to single electron−single hole excitations with dipole contributions. The so-called dipole transition contribution maps (DTCM) showing these decompositions (Figures S77−S81) indicate that the lowest-energy peak has a clear gold−gold character, having electrons removed from HOMO and HOMO−1 orbitals and placing them to the LUMO orbital. The second absorption peak has a mixed character by including gold−gold transitions from HOMO/HOMO−1 to LUMO+2 as well as ligand-to-gold transitions. The weight of ligand-to-gold transitions increase as the peak energy increases for the third and fourth absorbance peaks.

The electronic structure of phosphine/thiolate or NHC-protected biicosahedral Au_{25} clusters was previously rationalized[23,52] as a "dimer" of two closed-shell superatoms. Clusters $[\mathbf{4b}]^{2+}$ and $[\mathbf{5b}]^+$ described herein, likely possess similar electronic configurations, and therefore detailed calculations were not carried out on these systems.

Photoluminescence Studies

Given the high PLQY (*ca.* 16%) observed for our previously reported NHC-stabilized Au_{13} clusters,[17] an investigation into the emission properties of both Au_{10} and Au_{25} clusters was undertaken. Excitation and emission spectra of $[\mathbf{3b}]^+$ and $[\mathbf{4b}]^{2+}$ were acquired, as well as fluorescence excitation−emission matrix (EEM) data (see the SI for details). Photoluminescence from $[\mathbf{4b}]^{2+}$ was found to be significantly brighter as compared with $[\mathbf{3b}]^+$ (Figure 10, inset). Emission maxima were observed at ∼795 and 785 nm for $[\mathbf{3b}]^+$ and $[\mathbf{4b}]^{2+}$, respectively (Figure 10). The excitation spectrum of $[\mathbf{4b}]^{2+}$ matches very well with its absorbance spectrum (Figure S69); the position and profile of the emission band are independent of the excitation wavelength. Both these observations confirm the absence of emissive impurities in the cluster sample. Of note, the presence of O_2 does not decrease or quench the emission, suggesting that no triplet state is involved in the emission.

The observed optical band gap is 550 nm for $[\mathbf{3b}]^+$ (2.25 eV), demonstrating the high stability of this cluster. This matches well with the computed value as discussed above. The PLQY was determined by the comparative method using zinc phthalocyanine as a standard (Figures S72 and S73). Cluster $[\mathbf{3b}]^+$ was shown to have a PLQY of *ca.* 0.9%, which is of the order expected for Au nanoclusters. The Au_{25} cluster $[\mathbf{4b}]^{2+}$

https://doi.org/10.1021/jacsau.2c00004
JACS Au 2022, 2, 875−885

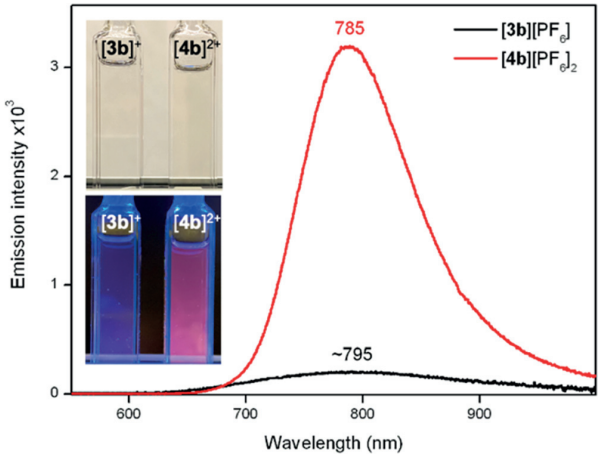

Figure 10. Emission spectra (excited at 336 nm) of deoxygenated solutions of [**3b**][PF_6] (black) and [**4b**][PF_6]$_2$ (red) in dichloromethane. The concentration of solutions was adjusted so the absorbance at 336 nm matches. Inset: photographs of the corresponding samples under visible (top) and UV (bottom) light.

showed a dramatically increased PLQY of 15%, which is significantly higher than that observed for most Au clusters. As was suggested previously,[17,18] the rigidity imparted upon the cluster through inter-ligand CH−π and π−π interactions most likely enhances the emission by restricting the nonradiative decay pathways of the excited state, and in the case of $[\mathbf{4b}]^{2+}$, the two fused Au_{13} icosahedra of the core are also further rigidified by bridging bromide ligands. However, relating the cluster structure to photophysical properties is challenging because PLQY measurements are carried out in solution, while detailed structural characterization is performed in the solid-state. Efforts to study photoluminescence properties in the solid-state are ongoing in our laboratories.

CONCLUSIONS

In conclusion, we have described a series of new NHC-stabilized $[Au_{10}(^{MesCH2}Bimy)_6X_3]^+$ clusters $[\mathbf{3a-c}]^+$ (X = Cl, Br, I) with a novel core architecture. The use of the bulky bis(2,4,6-trimethylbenzyl)benzimidazolium-2-ylidene ligand is important to drive cluster formation away from the more common Au_{13} clusters. Cluster $[\mathbf{3b}]^+$ undergoes a solvent- and counterion-dependent conversion into larger Au_{25} clusters, with both $[Au_{25}(^{MesCH2}Bimy)_{10}Br_8]^+$ and $[Au_{25}(^{MesCH2}Bimy)_{10}Br_7]^{2+}$ observed experimentally in the solid state by X-ray crystallography and in solutions by NMR using the clusters bearing ^{13}C-labeled NHC ligands. The nature of the halide is critically important, with chloride-containing Au_{10} clusters showing no propensity to convert to Au_{25}, and iodide-containing clusters more easily converting to Au_{25}.

Theoretical analysis showed that the conversion is connected to the increase of "metallicity" of the cluster from a 6-electron system to an unusual 16-electron system reported previously[23] and the conversion was monitored using ESI-MS and *in situ* NMR spectroscopy, in addition to UV−vis absorbance spectroscopy. While Au_{10} was only weakly emissive, the Au_{25} cluster displayed significantly increased photoluminescence, with the maximum emission wavelength of 785 nm, and PLQY of *ca.* 15%. Work to further tailor the emission of these clusters, understand the mechanism of cluster interconversion, and investigate further properties is underway at this time.

ASSOCIATED CONTENT

Supporting Information

The Supporting Information is available free of charge at https://pubs.acs.org/doi/10.1021/jacsau.2c00004.

Synthetic procedures, characterization data, and experimental results of monitoring the reaction progress using UV−vis absorbance, ESI-MS, and NMR spectroscopies; X-ray crystallographic data for [**3b**][OTf] (CCDC 2127768), [**4b**][$B(C_6F_5)_4]_2$ (CCDC 2127770), and [**5b**][$B(C_6F_5)_4$] (CCDC 2127779) are available free of charge at www.ccdc.cam.ac.uk/structures/ (PDF)

AUTHOR INFORMATION

Corresponding Authors

Kirill Kovnir − *Department of Chemistry, Iowa State University, Ames, Iowa 50011, United States; U.S. Department of Energy, Ames Laboratory, Ames, Iowa 50011, United States;* orcid.org/0000-0003-1152-1912; Email: kovnir@iastate.edu

Kevin G. Stamplecoskie − *Department of Chemistry, Queen's University, Kingston, Ontario K7L 3N6, Canada;* orcid.org/0000-0002-0232-9956; Email: kevin.stamplecoskie@queensu.ca

Tatsuya Tsukuda − *Department of Chemistry, Graduate School of Science, The University of Tokyo, Tokyo 113-0033, Japan;* orcid.org/0000-0002-0190-6379; Email: tsukuda@chem.s.u-tokyo.ac.jp

Hannu Häkkinen − *Departments of Chemistry and Physics, Nanoscience Center, University of Jyväskylä, 40014 Jyväskylä, Finland;* orcid.org/0000-0002-8558-5436; Email: hannu.j.hakkinen@jyu.fi

Masakazu Nambo − *Institute of Transformative Bio-Molecules (WPI-ITbM), Nagoya University Furo, Nagoya 464-8602, Japan;* orcid.org/0000-0003-0153-3178; Email: mnambo@itbm.nagoya-u.ac.jp

Cathleen M. Crudden − *Department of Chemistry, Queen's University, Kingston, Ontario K7L 3N6, Canada; Institute of Transformative Bio-Molecules (WPI-ITbM), Nagoya University Furo, Nagoya 464-8602, Japan;* orcid.org/0000-0003-2154-8107; Email: cruddenc@chem.queensu.ca

Authors

Paul A. Lummis − *Department of Chemistry, Queen's University, Kingston, Ontario K7L 3N6, Canada;* orcid.org/0000-0002-9212-3678

Kimberly M. Osten − *Institute of Transformative Bio-Molecules (WPI-ITbM), Nagoya University Furo, Nagoya 464-8602, Japan*

Tetyana I. Levchenko − *Department of Chemistry, Queen's University, Kingston, Ontario K7L 3N6, Canada*

Maryam Sabooni Asre Hazer − *Departments of Chemistry and Physics, Nanoscience Center, University of Jyväskylä, 40014 Jyväskylä, Finland*

Sami Malola − *Departments of Chemistry and Physics, Nanoscience Center, University of Jyväskylä, 40014 Jyväskylä, Finland*

Bryan Owens-Baird − *Department of Chemistry, Iowa State University, Ames, Iowa 50011, United States; U.S.*

https://doi.org/10.1021/jacsau.2c00004
JACS Au 2022, 2, 875−885

Department of Energy, Ames Laboratory, Ames, Iowa 50011, United States; orcid.org/0000-0003-3128-5363
Alex J. Veinot − *Department of Chemistry, Queen's University, Kingston, Ontario K7L 3N6, Canada*
Emily L. Albright − *Department of Chemistry, Queen's University, Kingston, Ontario K7L 3N6, Canada*
Gabriele Schatte − *Department of Chemistry, Queen's University, Kingston, Ontario K7L 3N6, Canada*
Shinjiro Takano − *Department of Chemistry, Graduate School of Science, The University of Tokyo, Tokyo 113-0033, Japan;* orcid.org/0000-0001-9262-5283

Complete contact information is available at: https://pubs.acs.org/10.1021/jacsau.2c00004

Author Contributions

[▽]P.A.L., K.M.O., and T.I.L. contributed equally to this work.

Notes

The authors declare no competing financial interest.

■ ACKNOWLEDGMENTS

The Natural Sciences and Engineering Research Council of Canada (NSERC) and the Canada Foundation for Innovation (CFI) are thanked for financial support of this work in terms of operating and equipment grants. K.M.O thanks JSPS for funding through the JSPS International Research Fellow program. T.I.L. thanks NSERC for a postdoctoral fellowship. A.J.V thanks NSERC for a Vanier Scholarship and also the Walter C. Sumner Foundation for a Walter C. Sumner Memorial Fellowship. E.L.A thanks NSERC CREATE-Materials for the Advanced Photonics and Sensing (MAPS) Program. This work was supported by KAKENHI from JSPS (17H03030 and 21H01949 to C.M.C.; 20H00370 to T.T.), JST CREST (JPMJCR20B2 to T. T.), and PRF (59632-ND3 to C.M.C). JSPS and NU are acknowledged for funding of this research through the World Premier International Research Centre Initiative (WPI) Program. K.K. is thankful to the National Science Foundation DMR-2003783 grant for support. The theory work was supported by the Academy of Finland (grants 294217, 319208, and HH's Academy Professorship). The computations were made at the Jyväskylä node of the Finnish Grid and Cloud infrastructure (FGCI). The authors thank Hannah Ramsay for assistance with photoluminescence studies and Dr. Yoshitaka Aramaki for help with X-ray crystal-structure analysis.

■ REFERENCES

(1) Nesterov, V.; Reiter, D.; Bag, P.; Frisch, P.; Holzner, R.; Porzelt, A.; Inoue, S. NHCs in Main Group Chemistry. *Chem. Rev.* **2018**, *118*, 9678−9842.
(2) Marion, N.; Nolan, S. P. N-Heterocyclic Carbenes in Gold Catalysis. *Chem. Soc. Rev.* **2008**, *37*, 1776−1782.
(3) Peris, E. Smart N-Heterocyclic Carbene Ligands in Catalysis. *Chem. Rev.* **2018**, *118*, 9988−10031.
(4) Smith, C. A.; Narouz, M. R.; Lummis, P. A.; Singh, I.; Nazemi, A.; Li, C.-H.; Crudden, C. M. N-Heterocyclic Carbenes in Materials Chemistry. *Chem. Rev.* **2019**, *119*, 4986−5056.
(5) Weidner, T.; Baio, J. E.; Mundstock, A.; Große, C.; Karthäuser, S.; Bruhn, C.; Siemeling, U. NHC-Based Self-Assembled Monolayers on Solid Gold Substrates. *Aust. J. Chem.* **2011**, *64*, 1177−1179.
(6) Zhukhovitskiy, A. V.; Mavros, M. G.; Voorhis, T. V.; Johnson, J. A. Addressable Carbene Anchors for Gold Surfaces. *J. Am. Chem. Soc.* **2013**, *135*, 7418−7421.
(7) Crudden, C. M.; Horton, J. H.; Ebralidze, I. I.; Zenkina, O. V.; McLean, A. B.; Drevniok, B.; She, Z.; Kraatz, H.-B.; Mosey, N. J.; Seki, T.; Keske, E. C.; Leake, J. D.; Rousina-Webb, A.; Wu, G. Ultra Stable Self-Assembled Monolayers of N-Heterocyclic Carbenes on Gold. *Nat. Chem.* **2014**, *6*, 409−414.
(8) (a) Crudden, C. M.; Horton, J. H.; Narouz, M. R.; Li, Z.; Smith, C. A.; Munro, K.; Baddeley, C. J.; Larrea, C. R.; Drevniok, B.; Thanabalasingam, B.; McLean, A. B.; Zenkina, O. V.; Ebralidze, I. I.; She, Z.; Kraatz, H.-B.; Mosey, N. J.; Saunders, L. N.; Yagi, A. Simple Direct Formation of Self-Assembled N-Heterocyclic Carbene Monolayers on Gold and Their Application in Biosensing. *Nat. Commun.* **2016**, *7*, No. 12654. (b) Amirjalayer, S.; Bakker, A.; Freitag, M.; Glorius, F.; Fuchs, H. Cooperation of N-Heterocyclic Carbenes on a Gold Surface. *Angew. Chem. Int. Ed.* **2020**, *59*, 21230−21235.
(9) Vignolle, J.; Tilley, T. D. N-Heterocyclic Carbene-Stabilized Gold Nanoparticles and Their Assembly into 3D Superlattices. *Chem. Commun.* **2009**, 7230−7232.
(10) MacLeod, M. J.; Johnson, J. A. PEGylated N-Heterocyclic Carbene Anchors Designed to Stabilize Gold Nanoparticles in Biologically Relevant Media. *J. Am. Chem. Soc.* **2015**, *137*, 7974−7977.
(11) Ling, X.; Schaeffer, N.; Roland, S.; Pileni, M.-P. Superior Oxygen Stability of N-Heterocyclic Carbene-Coated Au Nanocrystals: Comparison with Dodecanethiol. *Langmuir* **2015**, *31*, 12873−12882.
(12) Narouz, M. R.; Li, C.-H.; Nazemi, A.; Crudden, C. M. Amphiphilic N-Heterocyclic Carbene-Stabilized Gold Nanoparticles and Their Self-Assembly in Polar Solvents. *Langmuir* **2017**, *33*, 14211−14219.
(13) Salorinne, K.; Man, R. W. Y.; Li, C.-H.; Taki, M.; Nambo, M.; Crudden, C. M. Water-Soluble N-Heterocyclic Carbene-Protected Gold Nanoparticles: Size-Controlled Synthesis, Stability, and Optical Properties. *Angew. Chem., Int. Ed.* **2017**, *56*, 6198−6202.
(14) (a) Man, R. W. Y.; Li, C.-H.; MacLean, M. W. A.; Zenkina, O. V.; Zamora, M. T.; Saunders, L. N.; Rousina-Webb, A.; Nambo, M.; Crudden, C. M. Ultrastable Gold Nanoparticles Modified by Bidentate N-Heterocyclic Carbene Ligands. *J. Am. Chem. Soc.* **2018**, *140*, 1576−1579. (b) Asensio, J. M.; Tricard, S.; Coppel, Y.; Andrés, R.; Chaudret, B.; de Jésus, E. Synthesis of Water-Soluble Pallladium Nanoparticles Stabilized by Sulfonate N-Heterocyclic Carbenes. *Chem. Eur. J.* **2017**, *23*, 13435−13444.
(15) MacLeod, M. J.; Goodman, A. J.; Ye, H.-Z.; Nguyen, H. V.-T.; Voorhis, T. V.; Johnson, J. A. Robust Gold Nanorods Stabilized by Bidentate N-Heterocyclic-Carbene−Thiolate Ligands. *Nat. Chem.* **2019**, *11*, 57−63.
(16) Narouz, M. R.; Osten, K. M.; Unsworth, P. J.; Man, R. W. Y.; Salorinne, K.; Takano, S.; Tomihara, R.; Kaappa, S.; Malola, S.; Dinh, C.-T.; Padmos, J. D.; Ayoo, K.; Garrett, P. J.; Nambo, M.; Horton, J. H.; Sargent, E. H.; Häkkinen, H.; Tsukuda, T.; Crudden, C. M. N-Heterocyclic Carbene-Functionalized Magic-Number Gold Nanoclusters. *Nat. Chem.* **2019**, *11*, 419−425.
(17) Narouz, M. R.; Takano, S.; Lummis, P. A.; Levchenko, T. I.; Nazemi, A.; Kaappa, S.; Malola, S.; Yousefalizadeh, G.; Calhoun, L. A.; Stamplecoskie, K. G.; Häkkinen, H.; Tsukuda, T.; Crudden, C. M. Robust, Highly Luminescent Au_{13} Superatoms Protected by N-Heterocyclic Carbenes. *J. Am. Chem. Soc.* **2019**, *141*, 14997−15002.
(18) Shen, H.; Xiang, S.; Xu, Z.; Liu, C.; Li, X.; Sun, C.; Lin, S.; Teo, B. K.; Zheng, N. Superatomic Au_{13} Clusters Ligated by Different N-Heterocyclic Carbenes and Their Ligand-Dependent Catalysis, Photoluminescence, and Proton Sensitivity. *Nano Res.* **2020**, *13*, 1908−1911.
(19) Luo, P.; Bai, S.; Wang, X.; Zhao, J.; Yan, Z.-N.; Han, Y.-F.; Zang, S.-Q.; Mak, T. C. W. Tuning the Magic Sizes and Optical Properties of Atomically Precise Bidentate N-Heterocyclic Carbene-Protected Gold Nanoclusters via Subtle Change of N-Substituents. *Adv. Opt. Mater.* **2021**, *9*, No. 2001936.
(20) Yi, H.; Osten, K. M.; Levchenko, T. I.; Veinot, A. J.; Aramaki, Y.; Ooi, T.; Nambo, M.; Crudden, C. M. Synthesis and Enantioseparation of Chiral Au_{13} Nanoclusters Protected by Bis-N-Heterocyclic Carbene Ligands. *Chem. Sci.* **2021**, *12*, 10436−10440.

(21) Hirano, K.; Takano, S.; Tsukuda, T. Ligand Effects on the Structures of $[Au_{23}L_6(C{\equiv}CPh)_9]^{2+}$ (L = N-Heterocyclic Carbene vs Phosphine) with Au_{17} Superatomic Cores. *J. Phys. Chem. C* **2021**, *125*, 9930−9936.
(22) Shen, H.; Xu, Z.; Hazer, M. S. A.; Wu, Q.; Peng, J.; Qin, R.; Malola, S.; Teo, B. K.; Häkkinen, H.; Zheng, N. Surface Coordination of Multiple Ligands Endows N-Heterocyclic Carbene-Stabilized Gold Nanoclusters with High Robustness and Surface Reactivity. *Angew. Chem., Int. Ed.* **2021**, *60*, 3752−3758.
(23) Shen, H.; Deng, G.; Kaappa, S.; Tan, T.; Han, Y.-Z.; Malola, S.; Lin, S.-C.; Teo, B. K.; Häkkinen, H.; Zheng, N. Highly Robust but Surface-Active: An N-Heterocyclic Carbene-Stabilized Au_{25} Nanocluster. *Angew. Chem.* **2019**, *131*, 17895−17899.
(24) Collado, A.; Gómez-Suárez, A.; Martin, A. R.; Slawin, A. M. Z.; Nolan, S. P. Straightforward Synthesis of [Au(NHC)X] (NHC = N-Heterocyclic Carbene, X = Cl, Br, I) Complexes. *Chem. Commun.* **2013**, *49*, 5541−5543.
(25) Huynh, H. V.; Guo, S.; Wu, W. Detailed Structural, Spectroscopic, and Electrochemical Trends of Halido Mono- and Bis(NHC) Complexes of Au(I) and Au(III). *Organometallics* **2013**, *32*, 4591−4600.
(26) Gao, Z.-H.; Dong, J.; Zhang, Q.-F.; Wang, L.-S. Halogen Effects on the Electronic and Optical Properties of Au_{13} Nanoclusters. *Nanoscale Adv.* **2020**, *2*, 4902−4907.
(27) Briant, C. E.; Hall, K. P.; Wheeler, A. C.; Mingos, D. M. P. Structural Characterisation of $[Au_{10}Cl_3(PCy_2Ph)_6](NO_3)$(Cy = Cyclohexyl) and the Development of a Structural Principle for High Nuclearity Gold Clusters. *J. Chem. Soc. Chem. Commun.* **1984**, *4*, 248−250.
(28) Zheng, K.; Zhang, J.; Zhao, D.; Yang, Y.; Li, Z.; Li, G. Motif-Mediated $Au_{25}(SPh)_5(PPh_3)_{10}X_2$ Nanorods with Conjugated Electron Delocalization. *Nano Res.* **2019**, *12*, 501−507.
(29) Qian, H.; Zhu, M.; Lanni, E.; Zhu, Y.; Bier, M. E.; Jin, R. Conversion of Polydisperse Au Nanoparticles into Monodisperse Au_{25} Nanorods and Nanospheres. *J. Phys. Chem. C* **2009**, *113*, 17599−17603.
(30) Qian, H.; Eckenhoff, W. T.; Bier, M. E.; Pintauer, T.; Jin, R. Crystal Structures of Au_2 Complex and Au_{25} Nanocluster and Mechanistic Insight into the Conversion of Polydisperse Nanoparticles into Monodisperse Au_{25} Nanoclusters. *Inorg. Chem.* **2011**, *50*, 10735−10739.
(31) Lin, J.; Li, W.; Liu, C.; Huang, P.; Zhu, M.; Ge, Q.; Li, G. One-Phase Controlled Synthesis of Au_{25} Nanospheres and Nanorods from 1.3nm Au: PPh_3 Nanoparticles: The Ligand Effects. *Nanoscale* **2015**, *7*, 13663−13670.
(32) Zhu, M.; Li, M.; Yao, C.; Xia, N.; Zhao, Y.; Yan, N.; Liao, L.; Wu, Z. PPh_3: Converts Thiolated Gold Nanoparticles to $[Au_{25}(PPh_3)_{10}(SR)_5Cl_2]^{2+}$. *Acta Phys.-Chim. Sin.* **2018**, *34*, 792−798.
(33) Kang, X.; Xiong, L.; Wang, S.; Yu, H.; Jin, S.; Song, Y.; Chen, T.; Zheng, L.; Pan, C.; Pei, Y.; Zhu, M. Shape-Controlled Synthesis of Trimetallic Nanoclusters: Structure Elucidation and Properties Investigation. *Chem. - Eur. J.* **2016**, *22*, 17145−17150.
(34) Shichibu, Y.; Negishi, Y.; Watanabe, T.; Chaki, N. K.; Kawaguchi, H.; Tsukuda, T. Biicosahedral Gold Clusters $[Au_{25}(PPh_3)_{10}(SC_nH_{2n+1})_5Cl_2]^{2+}$ (n = 2−18): A Stepping Stone to Cluster-Assembled Materials. *J. Phys. Chem. C* **2007**, *111*, 7845−7847.
(35) In chloroform, rapid conversion of Au_{10} clusters starts before the temperature of the solution reaches the value chosen for thermostated kinetic experiments; thus, the higher readings at zero time were observed in chloroform compared with methanol.
(36) For the experiments on Au_{10} conversion in parallel in chloroform and methanol with *in-situ* UV−vis absorbance monitoring, the temperature was set to 55 °C for consistency, since at higher temperatures in chloroform the data quality was affected by the inhomogeneity of near-to-boiling solvent. In all other experiments, conversion of Au_{10} to Au_{25} in methanol was performed at 60 °C to speed up the process.
(37) Zeng, J.-L.; Guan, Z.-J.; Du, Y.; Nan, Z.-A.; Lin, Y.-M.; Wang, Q.-M. Chloride-Promoted Formation of a Bimetallic Nanocluster $Au_{80}Ag_{30}$ and the Total Structure Determination. *J. Am. Chem. Soc.* **2016**, *138*, 7848−7851.
(38) Yuan, X.; Malola, S.; Deng, G.; Chen, F.; Häkkinen, H.; Teo, B. K.; Zheng, L.; Zheng, N. Atomically Precise Alkynyl- and Halide-Protected AuAg Nanoclusters $Au_{78}Ag_{66}(C{\equiv}CPh)_{48}Cl_8$ and $Au_{74}Ag_{60}(C{\equiv}CPh)_{40}Br_{12}$: The Ligation Effects of Halides. *Inorg. Chem.* **2021**, *60*, 3529−3533.
(39) Du, W.; Deng, S.; Chen, S.; Jin, S.; Zhen, Y.; Pei, Y.; Zhu, M. Anisotropic Evolution of Nanoclusters from Ag_{40} to Ag_{45}: Halogen- and Defect-Induced Epitaxial Growth in Nanoclusters. *J. Phys. Chem. Lett.* **2021**, *12*, 6654−6660.
(40) Lin, X.; Tang, J.; Zhang, J.; Yang, Y.; Ren, X.; Liu, C.; Huang, J. The Doping Engineering and Crystal Structure of Rod-like Au_8Ag_{17} Nanoclusters. *J. Chem. Phys.* **2021**, *155*, No. 074301.
(41) Teo, B. K.; Zhang, H. Cluster of Clusters. Structure of a New Cluster $[(p\text{-}Tol_3P)_{10}Au_{13}Ag_{12}Cl_7](SbF_6)_2$ Containing a Nearly Staggered-Eclipsed-Staggered Metal Configuration and Five Doubly-Bridging Ligands. *Inorg. Chem.* **1991**, *30*, 3115−3116.
(42) Teo, B. K.; Zhang, H. Synthesis and Structure of a Neutral Trimetallic Biicosahedral Cluster, $(Ph_3P)_{10}Au_{11}Ag_{12}Pt_2Cl_7$. A Comparative Study of Molecular and Crystal Structures of Vertex-Sharing Biicosahedral Mixed-Metal Nanoclusters. *J. Clust. Sci.* **2001**, *12*, 349−383.
(43) Bootharaju, M. S.; Kozlov, S. M.; Cao, Z.; Harb, M.; Maity, N.; Shkurenko, A.; Parida, M. R.; Hedhili, M. N.; Eddaoudi, M.; Mohammed, O. F.; Bakr, O. M.; Cavallo, L.; Basset, J.-M. Doping-Induced Anisotropic Self-Assembly of Silver Icosahedra in $[Pt_2Ag_{23}Cl_7(PPh_3)_{10}]$ Nanoclusters. *J. Am. Chem. Soc.* **2017**, *139*, 1053−1056.
(44) Kang, X.; Xiang, J.; Lv, Y.; Du, W.; Yu, H.; Wang, S.; Zhu, M. Synthesis and Structure of Self-Assembled $Pd_2Au_{23}(PPh_3)_{10}Br_7$ Nanocluster: Exploiting Factors That Promote Assembly of Icosahedral Nano-Building-Blocks. *Chem. Mater.* **2017**, *29*, 6856−6862.
(45) Yang, S.; Chai, J.; Song, Y.; Kang, X.; Sheng, H.; Chong, H.; Zhu, M. A New Crystal Structure of Au_{36} with a Au_{14} Kernel Cocapped by Thiolate and Chloride. *J. Am. Chem. Soc.* **2015**, *137*, 10033−10035.
(46) Li, J.-J.; Guan, Z.-J.; Yuan, S.-F.; Hu, F.; Wang, Q.-M. Enriching Structural Diversity of Alkynyl-Protected Gold Nanoclusters with Chlorides. *Angew. Chem.* **2021**, *133*, 6773−6777.
(47) Qin, Z.; Zhang, J.; Wan, C.; Liu, S.; Abroshan, H.; Jin, R.; Li, G. Atomically Precise Nanoclusters with Reversible Isomeric Transformation for Rotary Nanomotors. *Nat. Commun.* **2020**, *11*, No. 6019.
(48) Enkovaara, J.; Rostgaard, C.; Mortensen, J. J.; Chen, J.; Dulak, M.; Ferrighi, L.; Gavnholt, J.; Glinsvad, C.; Haikola, V.; Hansen, H. A.; Kristoffersen, H. H.; Kuisma, M.; Larsen, A. H.; Lehtovaara, L.; Ljungberg, M.; Lopez-Acevedo, O.; Moses, P. G.; Ojanen, J.; Olsen, T.; Petzold, V.; Romero, N. A.; Stausholm-Møller, J.; Strange, M.; Tritsaris, G. A.; Vanin, M.; Walter, M.; Hammer, B.; Häkkinen, H.; Madsen, G. K. H.; Nieminen, R. M.; Nørskov, J. K.; Puska, M.; Rantala, T. T.; Schiøtz, J.; Thygesen, K. S.; Jacobsen, K. W. Electronic Structure Calculations with GPAW: A Real-Space Implementation of the Projector Augmented-Wave Method. *J. Phys.: Condens. Matter* **2010**, *22*, No. 253202.
(49) Perdew, J. P.; Burke, K.; Ernzerhof, M. Generalized Gradient Approximation Made Simple. *Phys. Rev. Lett.* **1996**, *77*, 3865−3868.
(50) Kuisma, M.; Ojanen, J.; Enkovaara, J.; Rantala, T. T. Kohn-Sham Potential with Discontinuity for Band Gap Materials. *Phys. Rev. B* **2010**, *82*, No. 115106.
(51) Walter, M.; Akola, J.; Lopez-Acevedo, O.; Jadzinsky, P. D.; Calero, G.; Ackerson, C. J.; Whetten, R. L.; Grönbeck, H.; Häkkinen, H. A Unified View of Ligand-Protected Gold Clusters as Superatom Complexes. *Proc. Natl. Acad. Sci. U.S.A.* **2008**, *105*, 9157−9162.
(52) Goh, J.-Q.; Malola, S.; Häkkinen, H.; Akola, J. Role of the Central Gold Atom in Ligand-Protected Biicosahedral Au_{24} and Au_{25} Clusters. *J. Phys. Chem. C* **2013**, *117*, 22079−22086.

https://doi.org/10.1021/jacsau.2c00004
JACS Au 2022, 2, 875−885

Electronic Supporting Information

NHC-Stabilized Au_{10} Nanoclusters and their Conversion to Au_{25} Nanoclusters

Paul A. Lummis,[a]§ Kimberly M. Osten,[b]§ Tetyana I. Levchenko,[a]§ Maryam Sabooni Asre Hazer,[c] Sami Malola,[c] Bryan Owens-Baird,[d,e] Alex J. Veinot,[a] Emily L. Albright,[a] Gabriele Schatte,[a] Shinjiro Takano,[f] Kirill Kovnir,*[d,e] Kevin G. Stamplecoskie,*[a] Tatsuya Tsukuda,*[f] Hannu Häkkinen,*[c] Masakazu Nambo,*[b] and Cathleen M. Crudden*[a,b]

[a] Department of Chemistry, Queen's University, Chernoff Hall, Kingston, Ontario K7L 3N6, Canada.

[b] Institute of Transformative Bio-Molecules (WPI-ITbM) Nagoya University Furo, Chikusa, Nagoya 464-8602, Japan.

[c] Departments of Chemistry and Physics, Nanoscience Center, University of Jyväskylä, 40014 Jyväskylä, Finland.

[d] Department of Chemistry, Iowa State University, 2415 Osborn Drive, Ames, Iowa 50011, USA.

[e] Ames Laboratory, U.S. Department of Energy, Ames, Iowa 50011, USA.

[f] Department of Chemistry, Graduate School of Science, The University of Tokyo, 7-3-1 Hongo, Bunkyo-ku, Tokyo 113-0033, Japan.

§These authors contributed equally to this work.

*Corresponding authors: kovnir@iastate.edu, kevin.stamplecoskie@queensu.ca, tsukuda@chem.s.u-tokyo.ac.jp, hannu.j.hakkinen@jyu.fi, mnambo@itbm.nagoya-u.ac.jp, cruddenc@chem.queensu.ca.

5 Computational data

5.1 Computational analysis of cluster $[3b]^+$

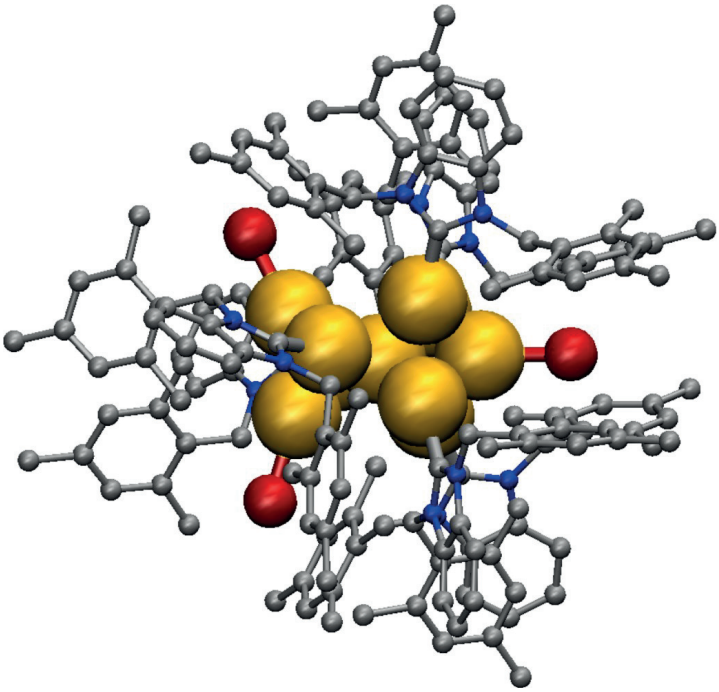

Figure S74. Optimized structure of the gas-phase model of $[\mathbf{3b}]^+$ using the PBE exchange-correlational functional.

Table S9. Experimental and computed (PBE) atom-atom bond lengths in the crystal structure and in the gas-phase model of $[\mathbf{3b}]^+$.

Atom indexing is shown in Figure S58.

Bond	Exp.	Calc.
Au(1)-Au(2)	2.679	2.749
Au(1)-Au(3)	2.730	2.768
Au(1)-Au(4)	2.702	2.790
Au(1)-Au(5)	2.697	2.828
Au(1)-Au(6)	2.738	2.868
Au(1)-Au(7)	2.627	2.676
Au(1)-Au(8)	2.735	2.835
Au(1)-Au(9)	2.687	2.826
Au(1)-Au(10)	2.709	2.799
Au(2)-Au(3)	2.664	2.714
Au(2)-Au(4)	2.883	3.043

Bond	Exp.	Calc.
Au(2)-Au(10)	2.879	2.973
Au(2)-Br(1)	2.416	2.471
Au(3)-Au(4)	2.809	2.945
Au(3)-Au(10)	2.795	2.887
Au(3)-Br(3)	2.420	2.481
Au(4)-Au(5)	2.852	2.933
Au(4)-Au(6)	2.889	2.967
Au(4)-C(82)	2.041	2.092
Au(5)-Au(6)	2.695	2.776
Au(5)-Au(7)	2.848	2.908
Au(5)-C(109)	2.029	2.076

Bond	Exp.	Calc.
Au(6)-Au(7)	2.927	3.015
Au(6)-C(1)	2.042	2.087
Au(7)-Au(8)	2.888	2.959
Au(7)-Au(9)	2.936	2.984
Au(7)-Br(2)	2.427	2.484
Au(8)-Au(9)	2.710	2.745
Au(8)-Au(10)	2.876	2.947
Au(8)-C(136)	2.027	2.063
Au(9)-Au(10)	2.834	2.921
Au(9)-C(28)	2.031	2.068
Au(10)-C(55)	2.032	2.072

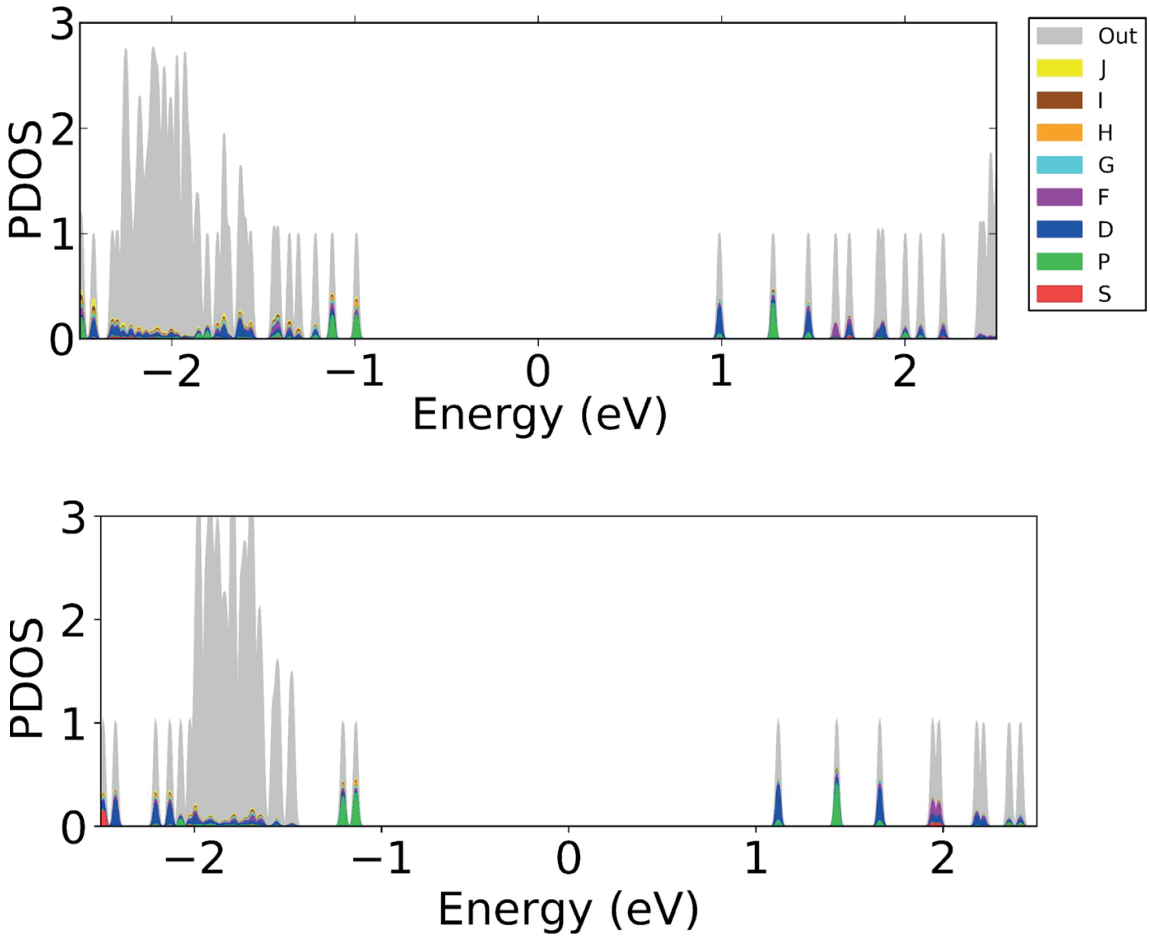

Figure S75. Electronic density of states in the gas-phase model of [**3b**]$^+$ by using the PBE (*top*) and GLLB-SC (*bottom*) xc functional.

Color coding shows the projection of the orbitals into spherical symmetry about the c.o.m of the cluster. The projection is done in a sphere of radius 3.5 Å. The grey area labeled as "out" denotes that part of the electron density that is either outside this radius (in the ligands) or cannot be spanned by the angular momentum components up to J symmetry.

Table S10. Bader charges for gold atoms and ligands in the gas-phase model of [**3b**]$^+$ calculated using the GLLB-SC functional.

Atom group	N	Total Q (e)	Q/N (e)
Au-center	1	-0.084	-0.084
Au-Br	3	-0.086	-0.028
Au-C	6	-0.067	-0.011
Br	3	-1.465	-0.488
NHC	6	2.703	0.45

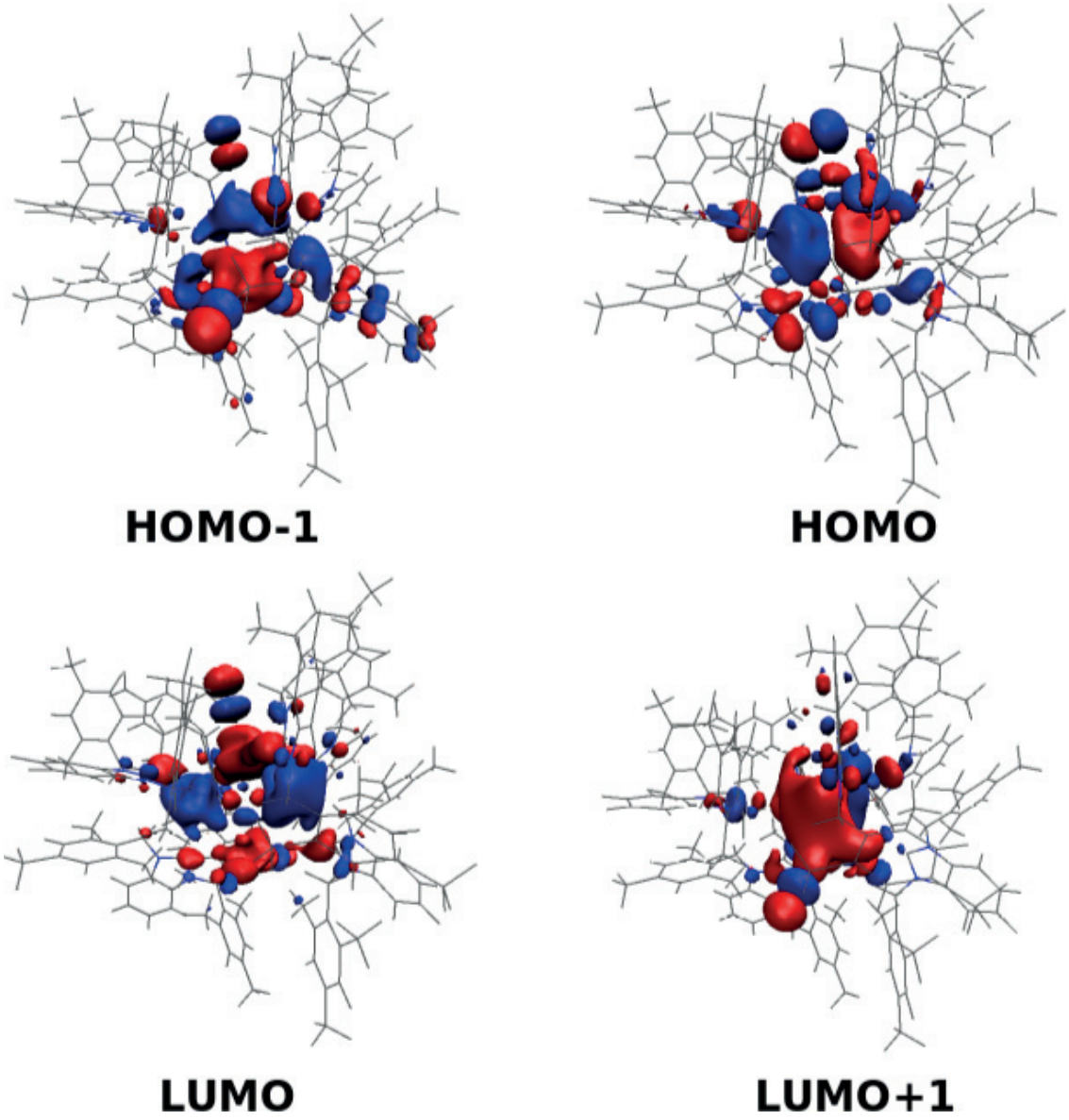

Figure S76. Visualisation of frontier orbitals for [**3b**]$^{+}$.

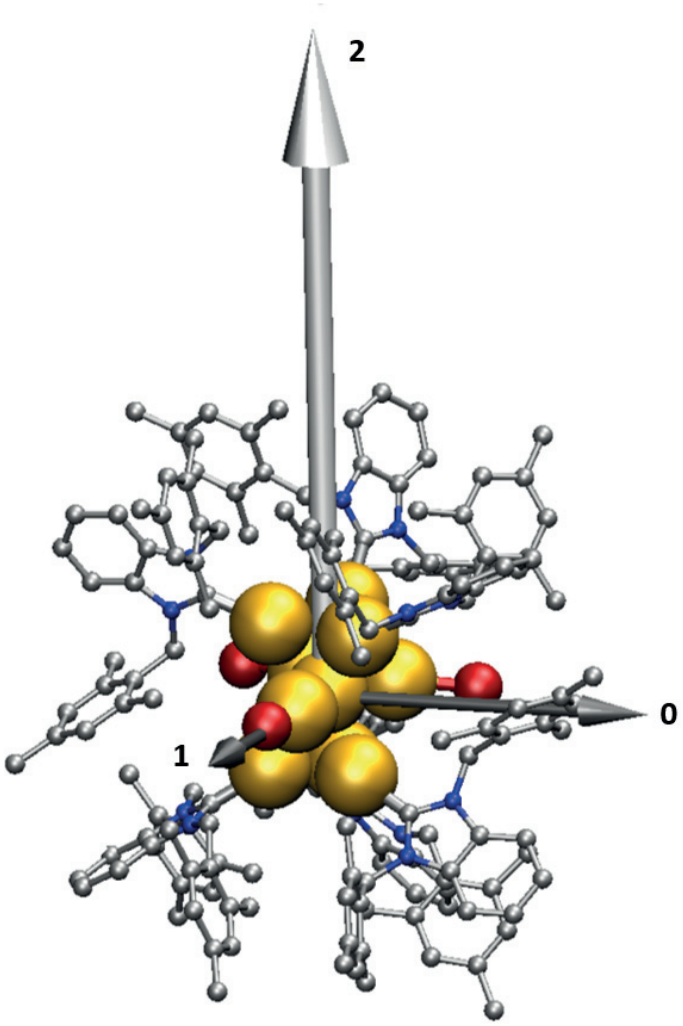

Figure S77. Dipole transition contribution maps (DTCM) analysis for [**3b**]$^{+}$ – Principal axes of moments of inertia.

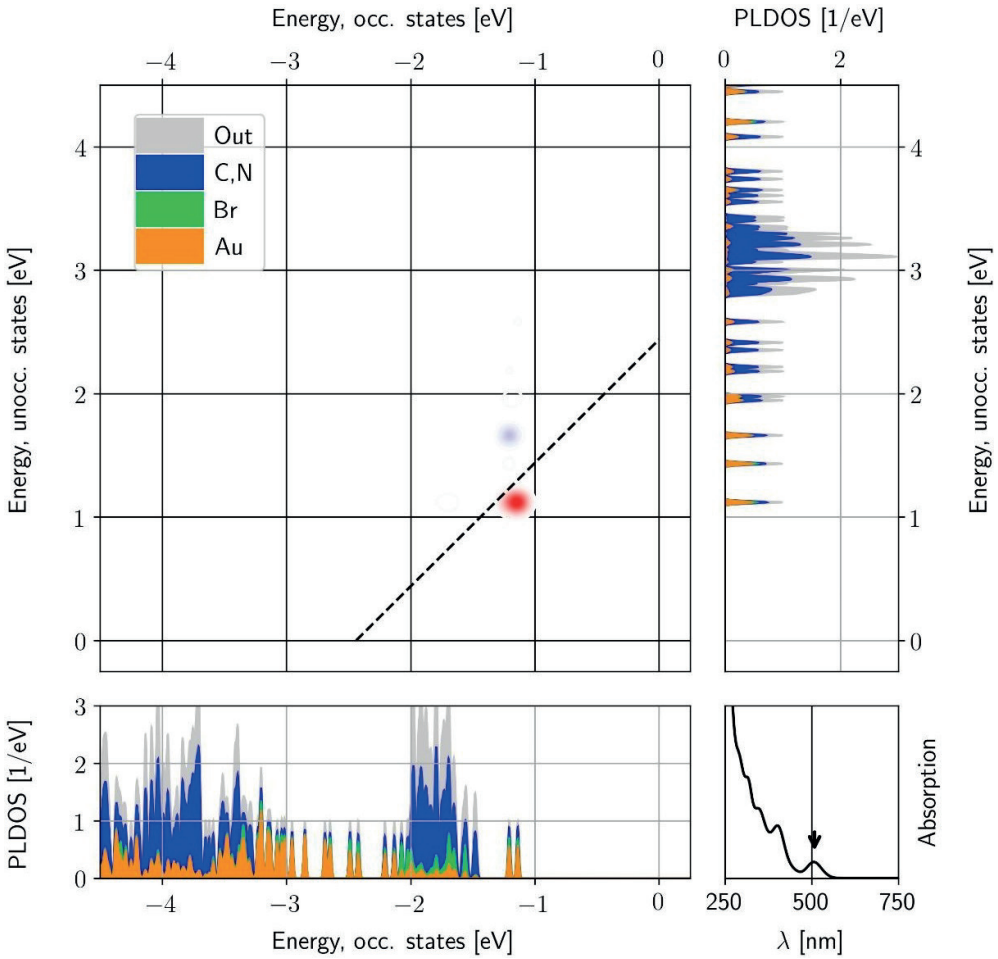

Figure S78. DTCM analysis for the lowest-energy peak (2.44 eV, shown in the bottom right panel) in the UV–vis absorbance spectrum of [**3b**]$^+$.

Bottom left panel shows the occupied electron states and the vertical panel on the right shows the empty states. Red/blue areas in the map denote constructive/destructive contributions of the electron-hole transitions to the total transition dipole. Along the dashed line, the hole-electron orbital energy difference matches the peak energy. The occupied and empty electron states are decomposed by the elemental weights as shown in the color coding.

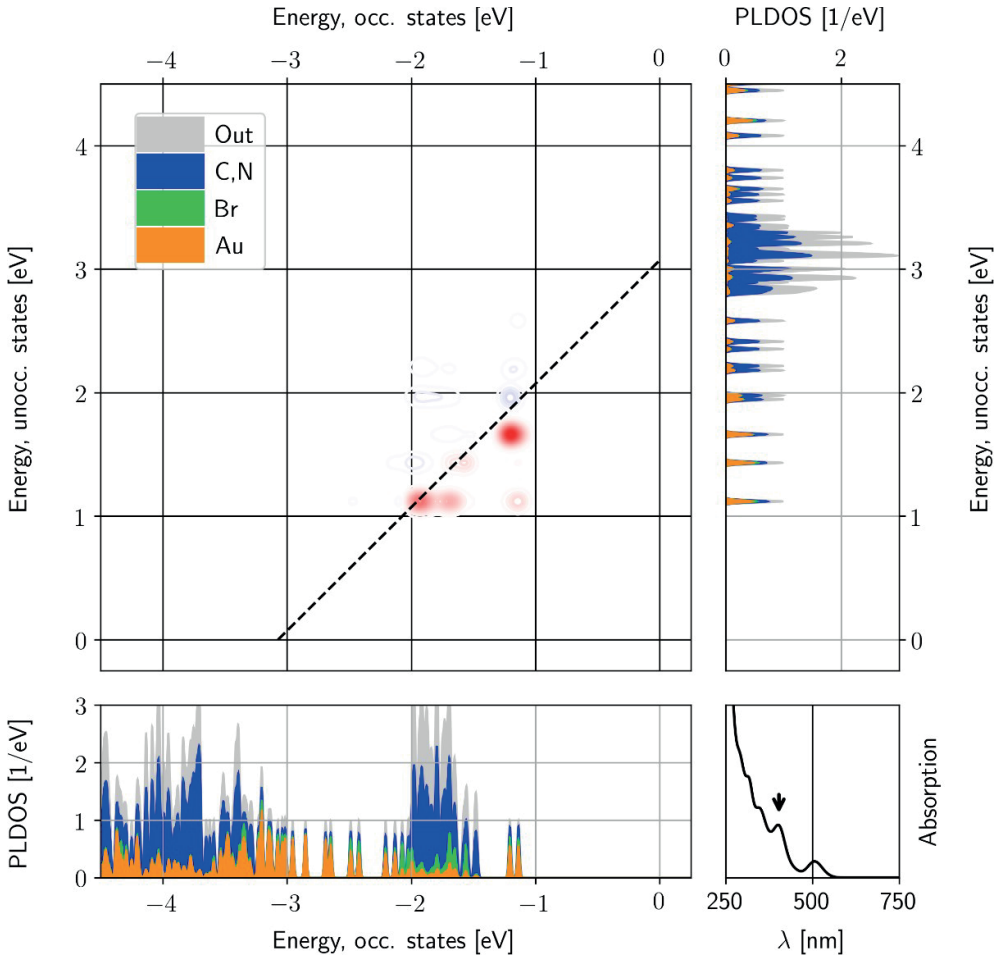

Figure S79. DTCM for peak at E = 3.07 eV.

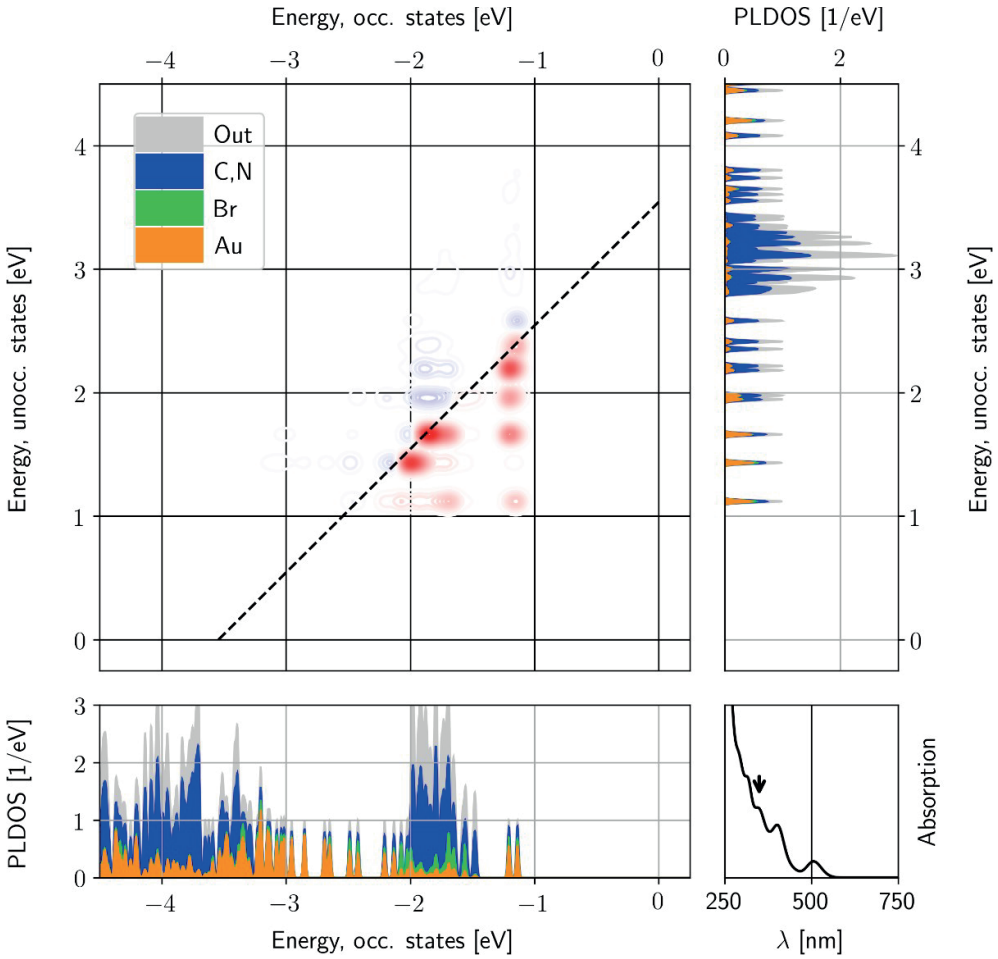

Figure S80. DTCM for peak at E = 3.54 eV.

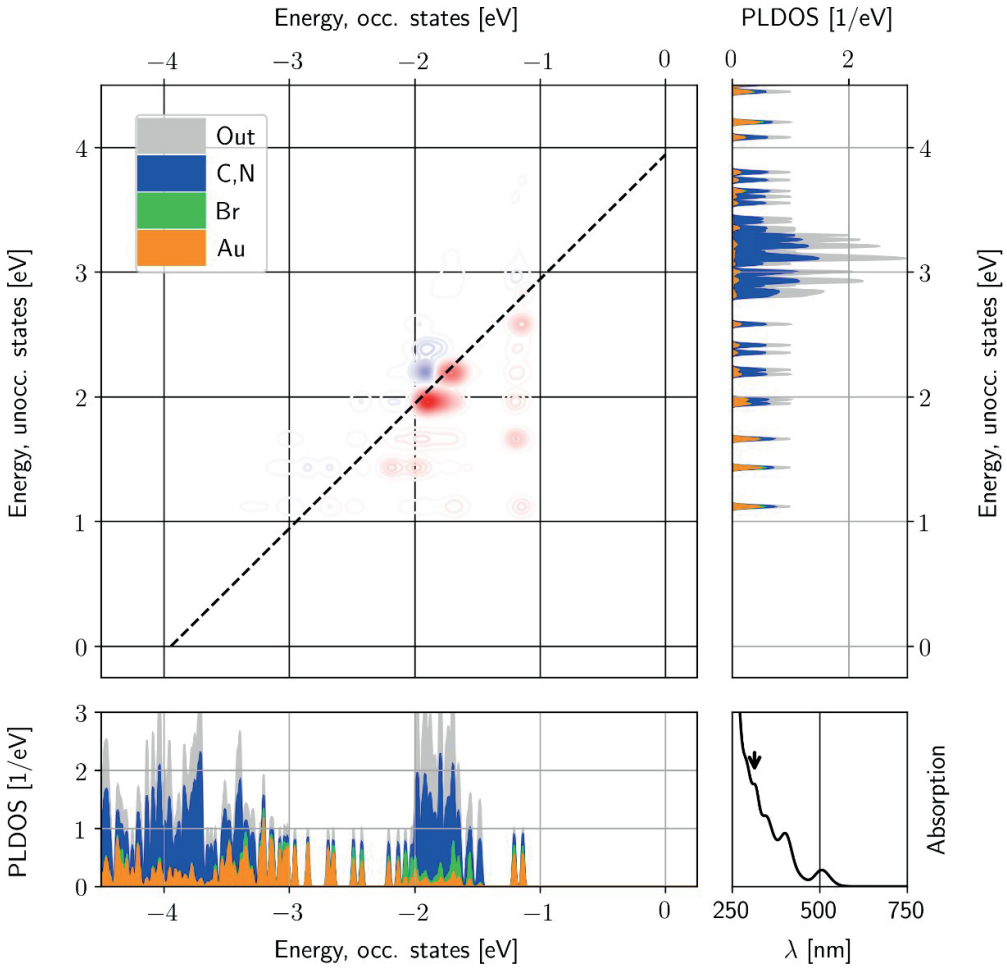

Figure S81. DTCM for peak at E = 3.94 eV.

PIII

SYNTHESIS AND PROPERTIES OF AN AU_6 CLUSTER SUPPORTED BY A MIXED N-HETEROCYCLIC CARBENE–THIOLATE LIGAND

by

Kirsi Salorinne, Renee W. Y. Man, Paul A. Lummis, **Maryam Sabooni Asre Hazer**, Sami Malola, Jacky C.-H. Yim, Alex J. Veinot,Wenxia Zhou, Hannu Hakkinen, Masakazu Nambo, and Cathleen M. Crudden (2020)

Chem. Commun., **56(45)**, 6102-6105

https://doi.org/10.1039/D0CC01482F

ChemComm

COMMUNICATION

View Article Online
View Journal | View Issue

Cite this: *Chem. Commun.*, 2020, **56**, 6102

Received 25th February 2020,
Accepted 6th April 2020

DOI: 10.1039/d0cc01482f

rsc.li/chemcomm

Synthesis and properties of an Au_6 cluster supported by a mixed N-heterocyclic carbene–thiolate ligand†

Kirsi Salorinne,[a] Renee W. Y. Man,[a] Paul A. Lummis,[b] Maryam Sabooni Asre Hazer,[c] Sami Malola,[c] Jacky C.-H. Yim,[a] Alex J. Veinot,[b] Wenxia Zhou,[b] Hannu Häkkinen,*[c] Masakazu Nambo*[a] and Cathleen M. Crudden*[ab]

The preparation of a novel Au_6 cluster bearing a bidentate mixed carbene–thiolate ligand is presented. The length of linker between the central benzimidazole and thiolate has a strong effect on the formation of cluster products, with a C_2 chain giving an Au_6 cluster, while a C_3 chain results in no evidence of cluster formation. Density functional theory analysis predicts a non-metallic cluster with a large HOMO–LUMO (3.2–3.6 eV) and optical gap.

Metal nanoclusters (NCs) are interesting structures that bridge the gap between classical molecular metal complexes, and metal nanoparticles (NPs).[1] Unlike metal NPs, which are aggregates described by average size, metal NCs are atomically precise species with discrete molecular formula.[2,3] Gold is by far the most common metal employed in the preparation of metal NCs,[4] including coordination clusters and superatom clusters.[5] In coordination clusters, all Au atoms are in the 1+ oxidation state. These clusters are held together by a combination of bridging ligands and aurophillic interactions.[6] Superatom clusters are primarily Au(0) core with defined numbers of valence electrons in a closed-shell electronic configuration. The large majority of these clusters are stabilized by thiolate ligands,[7] in addition to other X-type ligands,[3,4,8] and phosphines.[9]

N-Heterocyclic carbenes (NHCs) are emerging as valuable ligands for the protection of metallic materials, including both types of nanocluster.[10–14] In a recent report, Corrigan described an Au_8 cluster (**I**, Chart 1),[15] in which a central Au_4 core is supported by bridging thiolate moieties, and surrounded by 4 additional Au atoms each appended by an N-heterocyclic carbene. Coordination cluster **II**, $[(Im^iPr_2{\cdot}Au)_6(\mu_6\text{-}C)][BF_4]_2$, described by Shionoya *et al.*, has an anti-prismatic $(Au^+)_6$ core with an endohedral carbon that is formally C^{4-} (Chart 1, Im^iPr_2 = 1,3-diisopropylimidazol-2-ylidene).[16] Both of the aforementioned clusters benefit from significantly higher stability than related coinage metal clusters stabilized by phosphines.[17]

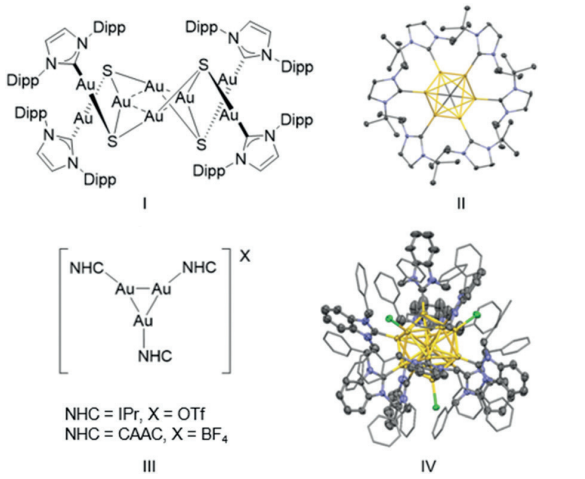

Chart 1 Examples of previously reported NHC-containing gold clusters: $[Au_8(IPr)_4S_4]$ (**I**);[13] $[(^{iPr}ImAu)_6(\mu^6\text{-}C)]^{2+}$ (**II**);[14] $[(NHC)_3Au_3]^+$ (**III**);[15,16] and $[Au_{13}(^{Bn}Bimy)_9Cl_3]^{2+}$ (**IV**).[18]

Recent reports of NHC-stabilized Au superatom clusters have also appeared, including $[Au_3]^+$ clusters reported by Sadighi[18] and Bertrand (**III**, Chart 1).[19] The first NHC-protected superatom clusters with larger cores were reported recently, stabilized by mixtures of NHCs and phosphine ligands,[20] or entirely by NHC ligands[21] (**IV**, Chart 1).[21a] Although NHCs and thiolates form the strongest bonds to gold, there are very few examples of ligands bearing both binding moieties within the same ligand.[22] Since these few examples have proven successful in the protection of nanoparticles[22a] and nanorods,[22b] we began a study of the behaviour of mixed NHC thiolate ligands on gold clusters.

[a] *Institute of Transformative Bio-Molecules (WPI-ITbM), Nagoya University, Chikusa, Nagoya, Aichi 464-8602, Japan. E-mail: mnambo@itbm.nagoya-u.ac.jp*
[b] *Department of Chemistry, Queen's University, Chernoff Hall, Kingston, Ontario, K7L 3N6, Canada. E-mail: cruddenc@chem.queensu.ca*
[c] *Departments of Chemistry and Physics, Nanoscience Centre, University of Jyväskylä, 40014 Jyväskylä, Finland. E-mail: hannu.j.hakkinen@jyu.fi*

† Electronic supplementary information (ESI) available. CCDC 1985364 and 1985367. For ESI and crystallographic data in CIF or other electronic format see DOI: 10.1039/d0cc01482f

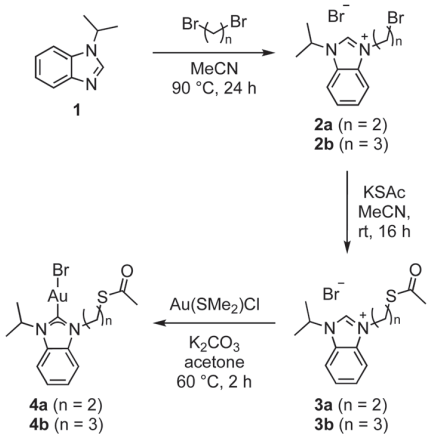

Scheme 1 Synthesis of ligand precursors, and gold complexes **4a** and **4b**.

To prepare the desired ligands, we began with 1-isopropylbenzimidazole (**1**), given our success working with benzimidazole-based NHCs bearing isopropyl wingtips.[11,12] The sulfur-containing wingtip was added by reaction of **1** with a dibromoalkane followed by potassium thioacetate (Scheme 1). For these ligands, C_2 and C_3 linkers were explored to permit greater conformational flexibility than a C_1 yet keep the two metal ligation points close enough for reliable cluster formation.

With the ligand salts in hand, Au(NHC)Br complexes **4a** and **4b** were prepared by reaction of **3a** and **3b** with $Au(SMe_2)Cl$ respectively, in the presence of K_2CO_3 in refluxing acetone to afford the desired complexes in high yields after workup (Scheme 1).[23] In the case of **4a**, crystals of suitable quality for single X-ray diffraction analysis were obtained from a 3 : 1 *n*-hexane : CH_2Cl_2 mixture that was stored at −20 °C overnight. (Fig. 1). This revealed that **4a** exists as a neutral monomeric species, with the pendant sulfur unligated to Au, and the Br atom

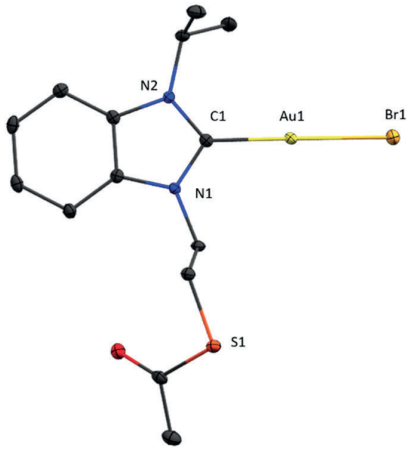

Fig. 1 Molecular structure of **4a**. Hydrogen atoms have been omitted for clarity. Selected bond lengths (Å) and angles (°): Au(1)–Br(1) 2.3986(4), C(1)–Au(1) 1.995(3), N(1)–C(1) 1.353(3), N(2)–C(1) 1.349(4); C(1)–Au(1)–Br(1) 176.52(8).

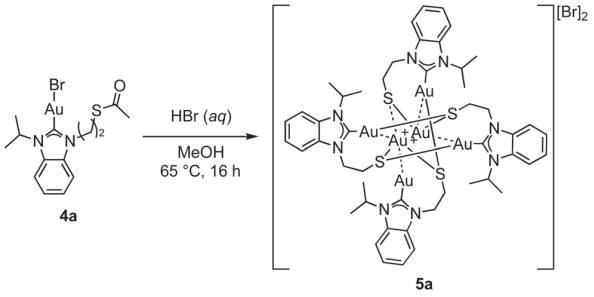

Scheme 2 Synthesis of Au_6 cluster **5a**.

still coordinated to Au, rather than a dimer with sulfur bound to gold and Br^- ion displaced to the outer coordination sphere.

Hydrolysis of **4a** and **4b** to reveal the thiolate was achieved by treating a methanol solution of the adduct with a degassed, aqueous solution of HBr (Scheme 2). This mixture was heated for 16 hours at 65 °C. In the case of **4a**, this produced a colourless powder after workup (**5a**, Scheme 2). Positive mode ESI-MS revealed the presence of a 2+ peak at 1029.0910 AMU, consistent with a product containing a cluster of the formula $[(NHC–S)_4Au_6]^{2+}$. In the hydrolysis of **4b** however, no product containing more than one Au centre was observed, with the bis-NHC cation $[(NHC–SH)_2Au]^+$ the major observed product by ESI-MS, demonstrating the importance of the precise length of the tether separating the NHC from the thiolate.

Cluster **5a** was recrystallized from EtOH/H_2O as colourless blocks following anion exchange with $[NH_4][PF_6]$. The molecular structure revealed a distorted anti-prismatic central Au_6 core, supported by four NHC–thiolate ligands, in good agreement with the product observed *via* ESI-MS analysis. Thus, the cluster cation can be considered to be comprised of two neutral $[(NHC–S)_2Au_2]$ units, with the additional Au^+ centres held in a staple-type bond between these two fragments. This results in a see-saw geometry for each of the non-carbon-bound Au^+ atoms, with S–Au^+–S angles of 177.55(5)°, comparable to the pseudo-linear geometry of the staples observed in other thiolate-protected Au clusters.[7,24] The Au···Au distances (3.426 Å) are significantly longer than those found in **I** (*cf.* 2.9282(3)–3.0548(3) Å),[15] **II** (2.9282(3)–3.0548(3) Å),[16] **III** (2.6438(5)–2.6633(5) Å),[18] or **IV** (2.7488(8)–3.006(1) Å),[21a] which display greater covalent character in their bonding. It can therefore be reasonably assumed that there are no covalent Au···Au interactions within the cluster.

Due to the presence of two Au^+ atoms that are not directly attached to the carbenic carbon of the NHC ligand, we were intrigued at the possibility of reducing these two gold centres *via* two discrete Au(I) → Au(0) reductions. This transformation would result in conversion of a coordination cluster containing all Au(I) atoms into a two-electron superatom Au cluster. Analysis of a 0.100 M solution of **5** by circular voltammetry did in fact show two irreversible reduction events, one at −0.6 V, and the second at −1.4 V (Fig. S23, ESI†), however it was not possible to tell whether the cluster remained intact after the second reduction. Therefore, we attempted chemical reduction with a variety of reducing agents to determine whether Au(0)

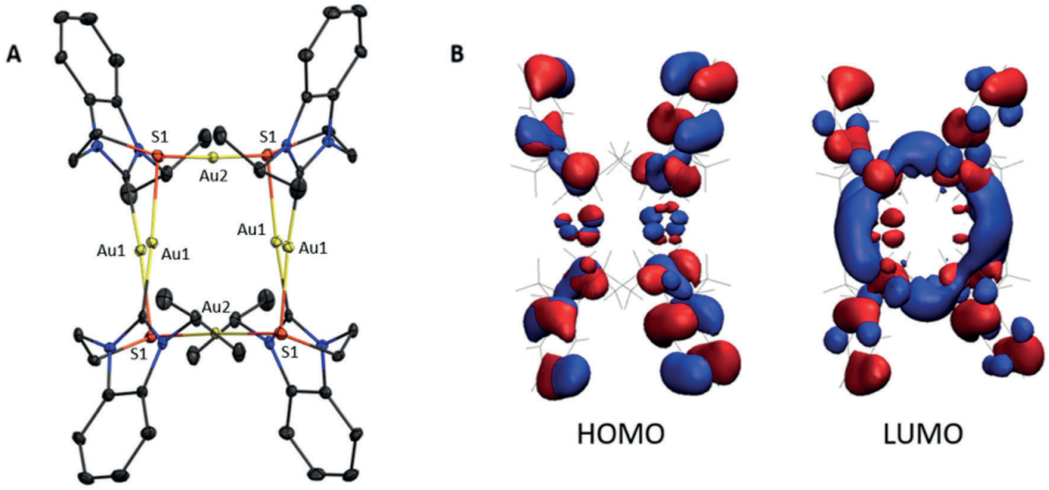

Fig. 2 (A) Molecular structure of cationic portion of $[Au_6\{^{iPr}BnIm\text{-}C_2H_4\text{-}(\mu_3\text{-}S)\}_4]^{2+}$ (**5a**). For clarity, all hydrogen atoms have been omitted. (B) Calculated frontier molecular orbitals of **5a**, with HOMO (left) and LUMO (right). For additional data on the molecular structure, and additional views of calculated orbitals, please refer to the ESI.†

clusters could be obtained, however, all synthetic attempts to obtain the neutral, doubly-reduced cluster were unsuccessful.

Density functional theory (DFT) computations were performed to provide insight into the electronic structure and optical properties of **5a** (for technical details, please see the ESI†). Optimization of the atomic structure with a total cluster charge of 2+ was done starting from the experimental crystal structure and using the PBE (Perdew–Burke–Ernzerhof) exchange–correlation functional.[25] Subsequently, the electronic structure and optical properties were analysed by re-calculating the wave functions in the PBE-optimized structure (Fig. S24, ESI†) using the GLLB-SC (Gritsenko-van Leeuwen-van Lenthe-Baerends with solid correlation) potential.[26] Optimization kept the overall cluster structure unchanged, although the Au–Au distances were overestimated by 2–4% which is typical for the PBE functional (Table S13, ESI†). Both functionals predict a very large energy gap (PBE: 3.22 eV and GLLB-SC: 3.55 eV) between the highest occupied (HOMO) and lowest unoccupied (LUMO) molecular orbitals and subsequently the cluster absorbs only in the UV region. Comparison of the measured (CH_2Cl_2) and computed optical spectra in Fig. 3 shows that the GLLB-SC spectrum yields a rather good agreement with the measured data. The first weaker absorption in the experimental spectrum around 325 nm is reproduced well. A double-peak main absorption, which shows in the experimental data just below 300 nm, is slightly blue-shifted in the computed spectrum. Furthermore, there is a peak in the computed spectrum close to 250 nm, probably corresponding to the rising absorption in the measured data to the blue from 250 nm.

Electronic state analysis (Fig. S25, ESI†) and visualization of a few frontier orbitals (Fig. 2B and Fig. S26, ESI†) revealed that many of the frontier orbitals have a mixed ligand-metal character and are lacking a clear superatomic symmetry. Rather they are of bonding–antibonding character between each metal atom, as would be expected for a coordination cluster complex.

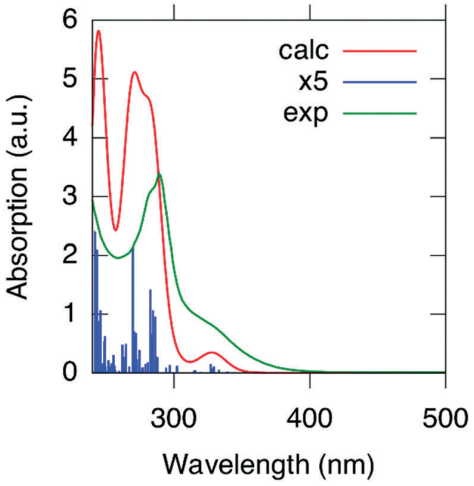

Fig. 3 Comparison of the computed (red, GLLB-SC functional) and the measured (green, in CH_2Cl_2) optical absorption spectrum of **5a** in UV-vis region. The computed spectrum is folded from the oscillator strengths (blue lines) of individual transitions using 0.1 eV Gaussian broadening. No energy shift or intensity scaling is applied to the computational data.

This agrees with the chemical formula of **5a**, where all Au atoms are in the 1+ oxidation state, and the cluster has a total 2+ charge.[27]

Analysis of the optical absorption spectrum (Fig. 3) in terms of dipole transition contribution maps showed that the two lowest-energy absorption peaks at 3.78 eV and 4.41 eV (Fig. S28 and S29, ESI†) have a strong ligand-to-metal character, while the peak at 4.57 eV has also metal-to-metal contribution, where the holes are formed in the occupied metal states around −3 eV (Fig. S30, ESI†).

In conclusion, we have synthesized novel Au_6 clusters using a bidentate, mono-anionic mixed NHC–sulfide ligand. The clusters

form as non-metallic di-cations. The cluster formation is sensitive to the chain length of the sidearm between the central benzimidazolylidine and the pendant thiolate, with a C_2 chain resulting in cluster formation and C_3 sidearm resulting in only monomeric Au species being detected. Further work to investigate novel homoleptic clusters with similar mixed ligand system is ongoing at this time.

The Natural Sciences and Engineering Research Council of Canada (NSERC) and the Canada Foundation for Innovation (CFI) are thanked for financial support of this work in terms of operating and equipment grants. AJV thanks NSERC for a Vanier Scholarship and also the Walter C. Sumner foundation for a Walter C. Sumner Memorial Fellowship. This work was supported by KAKENHI from JSPS (17H03030 to C. M. C.). JSPS and NU are acknowledged for funding of this research through The World Premier International Research Centre Initiative (WPI) program. Dr Yasutomo Segawa is thanked for assistance with X-ray crystal-structure analysis. Dr Gabriele Schatte is thanked for her assistance in collecting data for **4a**. The theory work was supported by the Academy of Finland (grants 294217, 319208, and HH's Academy Professorship). The computations were made at the Jyväskylä node of the Finnish Grid and Cloud infrastructure (FGCI).

Conflicts of interest

The authors declare no conflicts of interest.

Notes and references

1 S. Yamazoe, K. Koyasu and T. Tsukuda, *Acc. Chem. Res.*, 2014, **47**, 816.
2 R. Jin, *Nanoscale*, 2015, **7**, 1549.
3 I. Chakraborty and T. Pradeep, *Chem. Rev.*, 2017, **117**, 8208.
4 R. Jin, C. Zeng, M. Zhou and Y. Chen, *Chem. Rev.*, 2016, **116**, 10346.
5 (*a*) D. A. Pichugina, N. E. Kuz'menko and A. F. Shestakov, *Russ. Chem. Rev.*, 2015, **84**, 1114; (*b*) I. Chakraborty and T. Pradeep, *Chem. Rev.*, 2017, **117**, 8208.
6 (*a*) H. Schmidbaur and A. Schier, *Chem. Soc. Rev.*, 2008, **37**, 1931; (*b*) H. Schmidbaur and A. Schier, *Chem. Soc. Rev.*, 2012, **41**, 370.
7 P. D. Jadzinsky, G. Calero, C. J. Ackerson, D. A. Bushnell and R. D. Kornberg, *Science*, 2007, **318**, 430.
8 (*a*) B. K. Teo, X. Shi and H. Zhang, *J. Am. Chem. Soc.*, 1992, **114**, 2743; (*b*) F. Wen, U. Englert, B. Gutrath and U. Simon, *Eur. J. Inorg. Chem.*, 2008, 106; (*c*) G. Schmid, R. Pfeil, R. Boese, F. Bandermann, S. Meyer, G. H. M. Calis and J. W. A. van der Velden, *Chem. Ber.*, 1981, **114**, 3634.
9 (*a*) X.-K. Wan, S.-F. Yuan, Z.-W. Lin and Q.-M. Wang, *Angew. Chem., Int. Ed.*, 2014, **53**, 2923; (*b*) J. Chen, Q.-F. Zhang, T. A. Bonaccorso, P. G. Willard and L.-A. Wang, *J. Am. Chem. Soc.*, 2014, **136**, 92; (*c*) Y. Shichibu and K. Konishi, *Small*, 2010, **6**, 1216; (*d*) L. C. McKenzie, T. O. Zaikova and J. E. Hutchison, *J. Am. Chem. Soc.*, 2014, **136**, 13426.
10 C. R. Larrea, C. J. Baddeley, M. R. Narouz, N. J. Mosey, J. H. Horton and C. M. Crudden, *ChemPhysChem*, 2017, **18**, 3536.
11 R. W. Y. Man, C.-H. Li, M. W. A. MacLean, O. V. Zenkina, M. T. Zamora, L. N. Saunders, A. Rousina-Webb, M. Nambo and C. M. Crudden, *J. Am. Chem. Soc.*, 2018, **140**, 1576.
12 K. Salorinne, R. W. Y. Man, C.-H. Li, M. Taki, M. Nambo and C. M. Crudden, *Angew. Chem., Int. Ed.*, 2017, **56**, 6198.
13 (*a*) C. M. Crudden, J. H. Horton, I. I. Ebralidze, O. V. Zenkina, A. B. McLean, B. Drevniok, Z. She, H. B. Kraatz, N. J. Mosey, T. Seki, E. C. Keske and J. D. Leake, *Nat. Chem.*, 2014, **6**, 409; (*b*) A. V. Zhukhovitskiy, M. G. Mavros, T. Van Voorhis and J. A. Johnson, *J. Am. Chem. Soc.*, 2013, **135**, 7418–7421; (*c*) A. V. Zhukhovitskiy, M. J. MacLeod and J. A. Johnson, *Chem. Rev.*, 2015, **115**, 11503–11532; (*d*) S. Engel, E.-C. Fritz and B. J. Ravoo, *Chem. Soc. Rev.*, 2017, **46**, 2057–2075; (*e*) A. Bakker, A. Timmer, E. Kolodzeiski, M. Freitag, H. Y. Gao, H. Mönig, S. Amirjalayer, F. Glorius and H. Fuchs, *J. Am. Chem. Soc.*, 2018, **140**, 11889–11892.
14 C. M. Crudden, J. H. Horton, M. R. Narouz, Z. J. Li, C. A. Smith, K. Munro, C. J. Baddeley, C. R. Larrea, B. Drevniok, B. Thanabalasingam, A. B. McLean, O. V. Zenkina, I. I. Ebralidze, Z. She, H. B. Kraatz, N. J. Mosey, L. N. Saunders and A. Yagi, *Nat. Commun.*, 2016, **7**, 1.
15 A. M. Polgar, F. Weigend, A. Zhang, M. J. Stillman and J. F. Corrigan, *J. Am. Chem. Soc.*, 2017, **139**, 14045.
16 H. Ube, Q. Zhang and M. Shionoya, *Organometallics*, 2018, **37**, 2007.
17 O. Fuhr, S. Dehnen and D. Fenske, *Chem. Soc. Rev.*, 2013, **42**, 1871.
18 T. J. Robilotto, J. Bacsa, T. G. Gray and J. P. Sadighi, *Angew. Chem., Int. Ed.*, 2012, **51**, 12077.
19 D. S. Weinberger, M. Melaimi, C. E. Moore, A. L. Rheingold, G. Frenking, P. Jerabek and G. Bertrand, *Angew. Chem., Int. Ed.*, 2013, **52**, 8964.
20 M. R. Narouz, K. M. Osten, P. J. Unsworth, R. W. Y. Man, K. Salorinne, S. Takano, R. Tomihara, S. Kaappa, S. Malola, C.-T. Dinh, J. D. Padmos, K. Ayoo, P. Garrett, M. Nambo, J. H. Horton, E. H. Sargent, H. Häkkinen, T. Tsukuda and C. M. Crudden, *Nat. Chem.*, 2019, **11**, 419.
21 (*a*) M. R. Narouz, S. Takano, P. A. Lummis, T. I. Levchenko, A. Nazemi, S. Kaappa, S. Malola, G. Yousefalizadeh, L. Calhoun, K. G. Stamplecoskie, H. Häkkinen, T. Tsukuda and C. M. Crudden, *J. Am. Chem. Soc.*, 2019, **141**, 14997; (*b*) H. Shen, G. Deng, S. Kaappa, T. Tan, S. Malola, S.-C. Lin, B. K. Teo, H. Häkkinen and N. Zheng, *Angew. Chem., Int. Ed.*, 2019, **49**, 17895.
22 (*a*) A. Rühling, K. Schaepe, L. Rakers, B. Vonhören, P. Tegeder, B. J. Ravoo and F. Glorious, *Angew. Chem., Int. Ed.*, 2016, **55**, 5856; (*b*) M. J. MacLeod, A. J. Goodman, H.-Z. Ye, H. V. T. Nguyen, T. Van Voorhis and J. A. Johnson, *Nat. Chem.*, 2019, **11**, 57.
23 A. Collado, A. Gomez-Suárez, A. R. Martin, A. M. Z. Slawin and S. P. Nolan, *Chem. Commun.*, 2013, **49**, 5541.
24 M. Zhu, C. M. Aikens, F. J. Hollander, G. C. Schatz and R. Jin, *J. Am. Chem. Soc.*, 2008, **130**, 5883.
25 J. P. Perdew, K. Burke and M. Ernzerhof, *Phys. Rev. Lett.*, 1996, **77**, 3865.
26 M. Kuisma, J. Ojanen, J. Enkovaara and T. T. Rantala, *Phys. Rev. B: Condens. Matter Mater. Phys.*, 2010, **82**, 115106.
27 M. Walter, *et al.*, *Proc. Natl. Acad. Sci. U. S. A.*, 2008, **105**, 9157.

Electronic Supplementary Information

Synthesis and Properties of an Au_6 Cluster Supported by a Mixed *N*-Heterocyclic Carbene-Thiolate ligand

Kirsi Salorinne,[a] Renee W. Y. Man,[a] Paul A. Lummis,[b] Maryam Sabooni Asre Hazer,[c] Sami Malola,[c] Jacky C.-H. Yim,[a] Alex J. Veinot,[b] Wenxia Zhou,[b] Hannu Häkkinen,[c]* Masakazu Nambo,[a]* and Cathleen M. Crudden[a,b]*

[a.] *Institute of Transformative Bio-Molecules (WPI-ITbM), Nagoya University, Chikusa, Nagoya, Aichi 464-8602, Japan.*
[b.] *Department of Chemistry, Queen's University, Chernoff Hall, Kingston, Ontario, K7L 3N6, Canada.*
[c.] *Departments of Chemistry and Physics, Nanoscience Centre, University of Jyväskylä, 40014 Jyväskylä, Finland*

4. Computational data

4.1 Computational analysis of cluster 5a.

4.1.1 Figure S24: Relaxed structure of 5a calculated using PBE functional.

Au atoms are labeled as 1-6 in reference to Table S13.

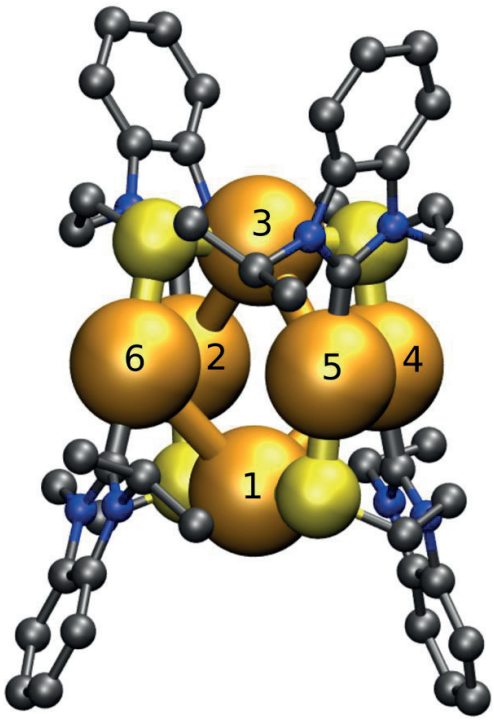

4.1.2 Figure S25: Gold-projected density of states for 5a.

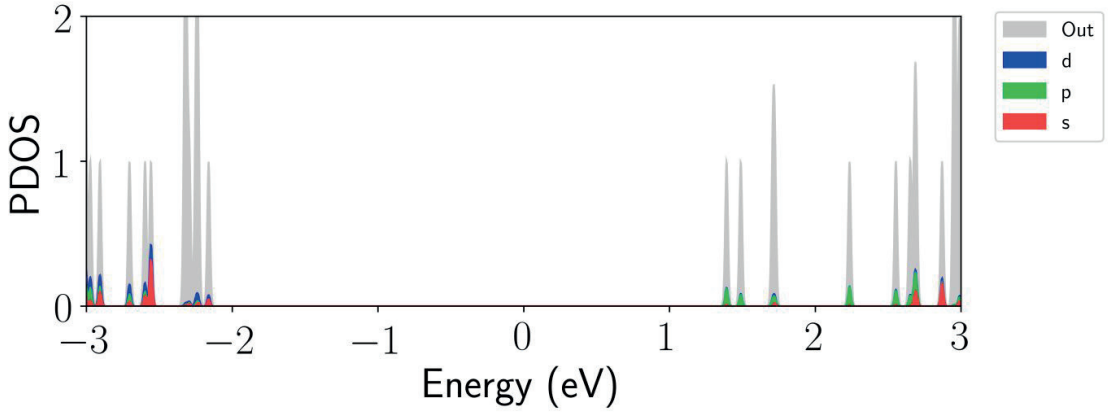

4.1.3 Figure S26: A few frontier orbitals for 5a.

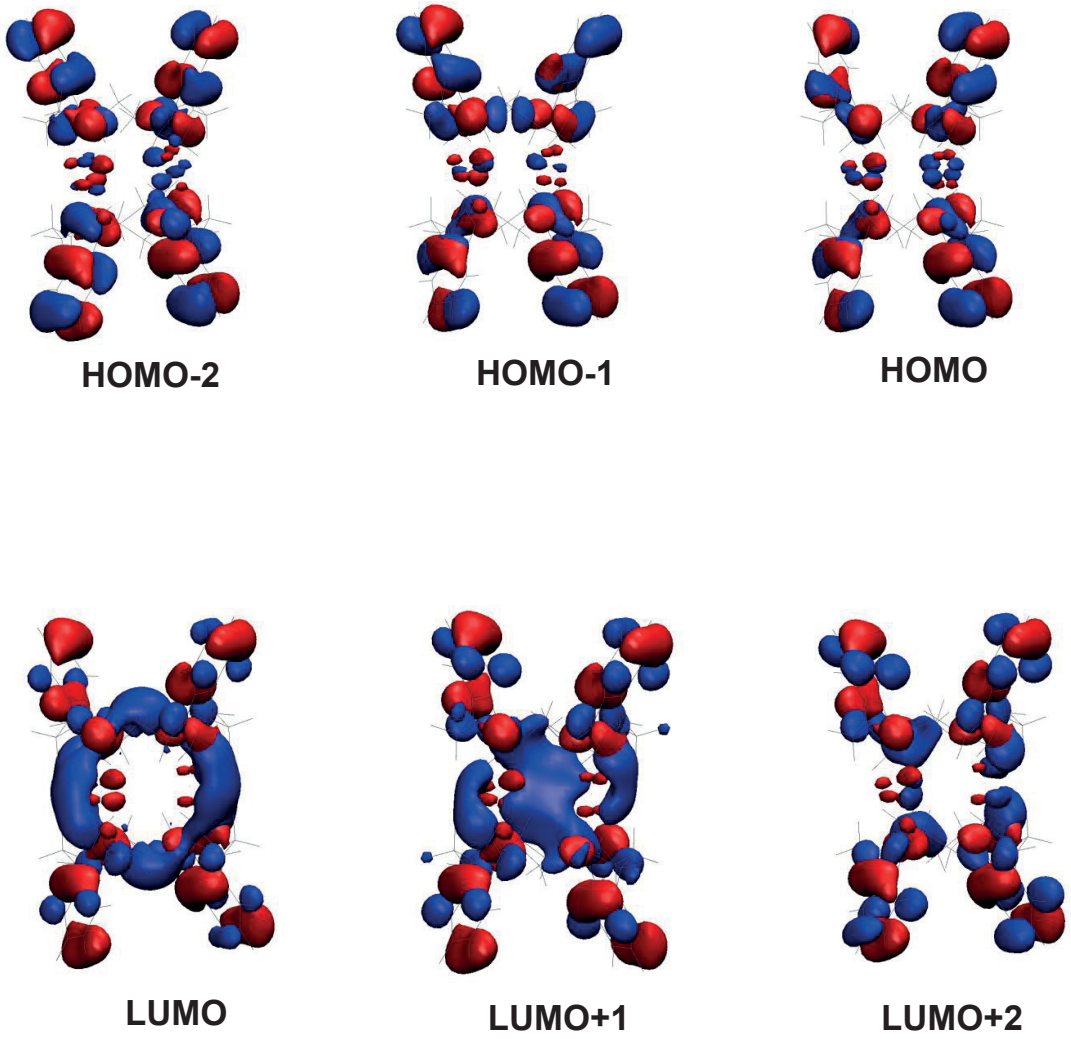

4.1.4 Table S13: Shortest Au-Au distances in 5a.

Au-Au	Experimental geometry Distance [**5a**][PF_6]$_2$ (Å)	Optimized geometry distance (Å)
1-6	3.537	3.637
1-5	3.426	3.582
1-3	4.633	4.753
1-4	3.537	3.600
2-3	3.537	3.597
3-4	3.426	3.592
3-5	3.537	3.626

4.1.5 Figure S27: Dipole transition contribution maps (DTCM) analysis for 5a – Principal axes of moments of inertia.

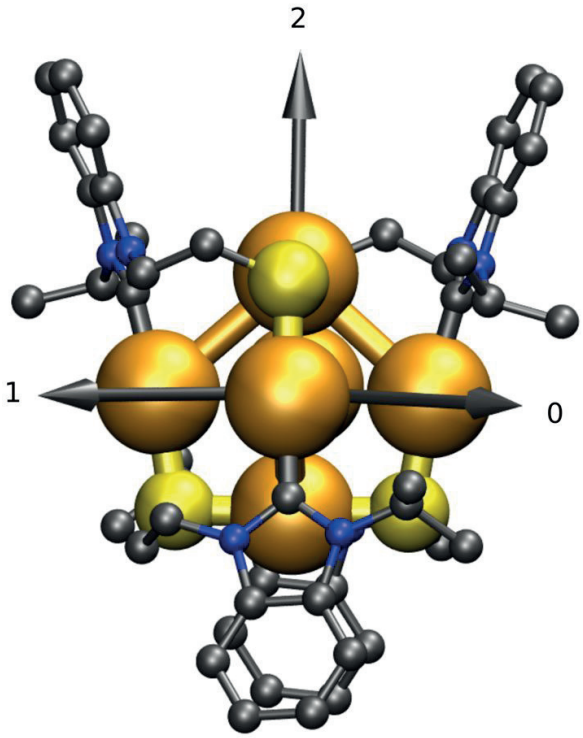

4.1.6 Figure S28: DTCM for peak at E = 3.779 eV.

Red / blue areas indicate constructive / destructive contributions of individual transitions to the total dipole moment. PDOS is analysed as projected to atomic Au s, p, d components. The grey area denotes orbital weights in ligands.

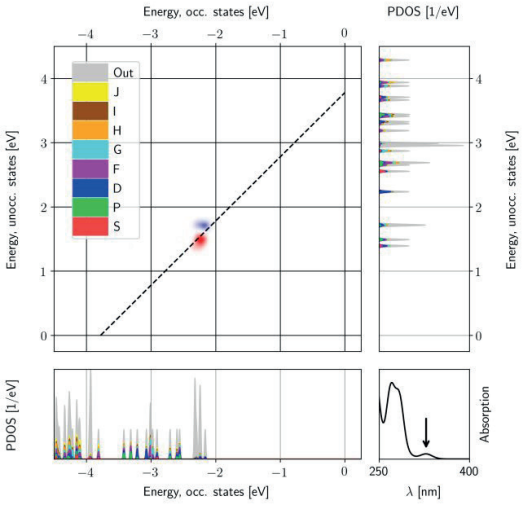

Axis 0

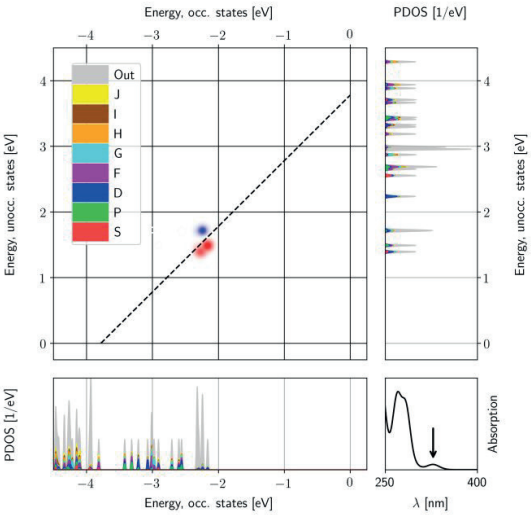

Axis 1

4.1.7 Figure S29: DTCM for peak at E = 4.413 eV.

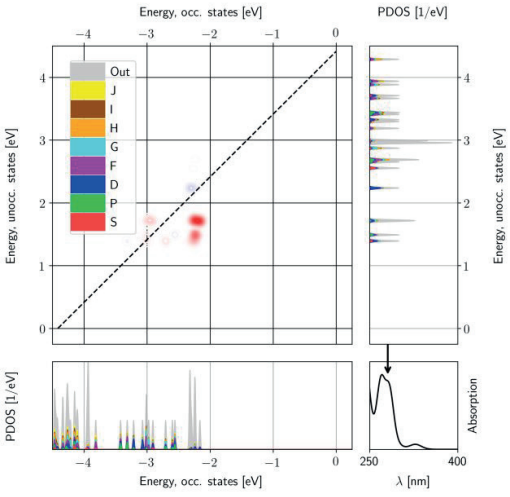

Axis 0

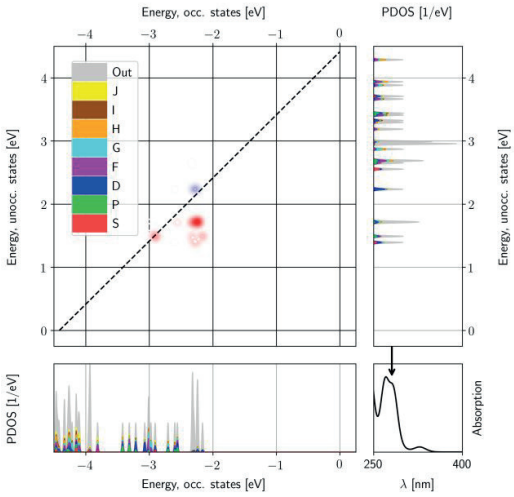

Axis 1

4.1.8 Figure S30: DTCM for peak at E = 4.570 eV.

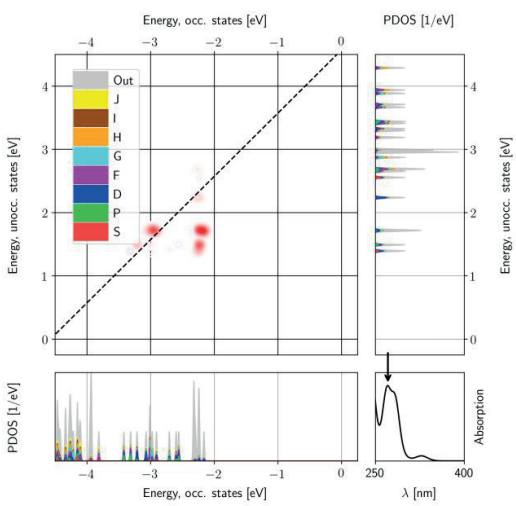

Axis 0

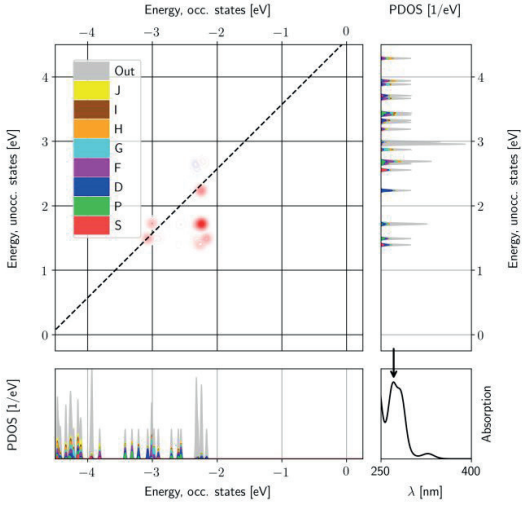

Axis 1

5. References

1. a) Y. Zhu, C. Cai and G. Lu, *Helv. Chim. Acta*, 2014, **97**, 1666. b) M. -C. Brandy, M. C. Jennings and R. J. Puddephatt, *J. Chem. Soc., Dalton Trans.*, 2000, 4601.
2. H. Hope, *Prog. Inorg. Chem.*, 1993, **41**, 1.
3. G. M. Sheldrick, *Acta. Cryst.*, 2015, **A71**, 3.
4. G. M. Sheldrick, *Acta. Cryst.*, 2015, **C71**, 3.
5. J. Enkovaara, et. al. *J. Phys. Condens. Matter*, 2010, **22**, 253202.
6. J. P. Perdew, K. Burke, and M. Ernzahof, *Phys. Rev. Lett.*, 1996, **78**, 3856.
7. M. Kuisma, J. Ojanen, J. Enkovaara, and T. T. Rantala, *Phys. Rev. B*, **82**, 115106
8. M. Walter, H. Häkkinen, L. Lehtovaara, J. Enkovaara, C. Rostgaard and J. J. Mortensen, *J. Phys. Chem.*, 2008, **128**, 244101.
9. S. Malola, L. Lehtovaara, J. Enkovaara, and H. Häkkinen, *ACS Nano*, 2013, **7**, 10263

PIV

ISOMER DYNAMICS OF THE $[AU_6(NHC\text{-}S)_4]^{2+}$ NANOCLUSTER

by

Maryam Sabooni Asre Hazer, Sami Malola and Hannu Hakkinen (2022)

Chem. Commun., **58(19)**, 3218-3221

https://doi.org/10.1039/D2CC00676F

ChemComm

COMMUNICATION

View Article Online
View Journal

Cite this: DOI: 10.1039/d2cc00676f

Received 2nd February 2022,
Accepted 7th February 2022

DOI: 10.1039/d2cc00676f

rsc.li/chemcomm

Isomer dynamics of the $[Au_6(NHC\text{-}S)_4]^{2+}$ nanocluster†

Maryam Sabooni Asre Hazer,[a] Sami Malola[b] and Hannu Häkkinen *[ab]

The use of metal nanoclusters is strongly reliant on their size and configuration; hence, studying the potential isomers of a cluster is extremely beneficial in understanding their performance. In general, the prediction and identification of isomer structures and their properties can be challenging and computationally expensive. Our work describes an investigation to find local isomers for the previously experimentally characterized small gold cluster $[Au_6(NHC\text{-}S)_4]^{2+}$ protected by bidentate mixed carbene-thiolate ligands. We employ the molecular dynamics simulation method where the interatomic forces are calculated from density functional theory. We find several isomers that are more stable than the isomer corresponding to the experimental crystal structure, as well as a significant impact of the finite-temperature atom dynamics on the electronic structure and optical properties. Our work highlights the growing need to investigate ligand-stabilized metal clusters to uncover isomerism and temperature effects on their properties.

Ligand-protected metal nanoclusters (NCs) have a wide range of applications due to their unique properties.[1–3] In order to investigate metal NCs and their characteristics, it is important to consider the influence of ligand groups.[4,5] A broad range of different ligands like chalcogenates, phosphines, alkynyls and N-heterocyclic carbenes (NHCs) have already been used.[6–20] Among all, gold clusters, in particular, have sparked considerable attention, for example due to their catalytic activity when supported by metal oxides.[21] A rising number of research studies have shown that the physicochemical properties of metal NCs are substantially impacted by the presence of different isomers, which influences the crystallization of the main NC.[22,23] However, this study demonstrates that the crystallized structure is not automatically the most stable isomer in the gas phase or in solution, which raises intriguing questions regarding how the presence of isomers affects crystallization or the catalytic activity of NCs in different conditions.

Computational methods provide a controlled way to study isomers. Properties of thiolate-protected gold NCs have been extensively studied using density functional theory (DFT) techniques. As an example, a study on the $Au_{28}(SR)_{20}$ cluster[24] suggested a novel isomer with relatively high stability composed of the same Au_{14} kernel but a different ligand shell compared to the two experimentally reported structures. It showed also that the new isomer is an important link in the formation of $Au_{22}(SR)_{18}$, $Au_{34}(SR)_{22}$ and $Au_{40}(SR)_{24}$ clusters. In another DFT study,[25] two low-lying $Au_{28}(SR)_{20}$ isomers were suggested successfully and three isomerism mechanisms were identified by studying the crystallized $Au_{38}(SR)_{24}$, $Au_{28}(SR)_{20}$, and $Au_{30}(SR)_{18}$ clusters.

DFT studies offer significant insight on isomerism, but finding the potential structures can be a considerable challenge. Here, combining DFT with molecular dynamics (MD) methods can help. A DFT-MD study, performed on $Au_{38}(SCH2CH2Ph)_{24}$[26] revealed that from the two empirically discovered isomers[27,28] the prolate shaped one is more stable than the oblate one.

Although many experimental techniques are successful to determine the atomic structure of metal NCs,[29–34] finding the presence of isomers is a difficult task by itself. In this regard, computational work can inspire new experimental investigations. In a recent work, a new isomer structure for the widely studied thiolate-protected gold cluster $Au_{25}(SR)_{18}$ was predicted from DFT-MD calculations in 2020,[35] and soon after, the presence of this isomer was confirmed both in gas-phase studies[36] and in solution.[37]

In this work, we investigate the previously characterized $[Au_6(NHC\text{-}S)_4]^{2+}$ cluster, protected by bidentate mixed carbene-thiolate ligands, with the experimental crystal structure provided in ref. 6. We performed DFT-MD simulations at three temperatures (approximately 145 K, 280 K and 475 K) with a goal to characterize the impact of temperature on the

[a] Department of Chemistry, Nanoscience Center, University of Jyväskylä, Jyväskylä, 40014, Finland. E-mail: hannu.j.hakkinen@jyu.fi
[b] Department of Physics, Nanoscience Center, University of Jyväskylä, Jyväskylä, 40014, Finland

† Electronic supplementary information (ESI) available: Details of the atomic structure of the Au_6 cluster, optical spectra and their analysis, and simulations in the crystal environment. See DOI: 10.1039/d2cc00676f

structural, electronic and optical properties. Our study reveals a systematic understanding of how temperature impacts the structure–property relations of the above-mentioned cluster. The most important findings are: (i) new isomers with a lower total energy than the structure reported from the experiment, (ii) demonstration of the effect of crystal environment on the isomer structure, (iii) a strong temperature dependence of the energy gap between the highest occupied and the lowest unoccupied molecular orbital (*i.e.* HOMO and LUMO), (iv) a clear correlation between the size of the HOMO–LUMO energy gap and a descriptive structural parameter of the cluster, and (v) shifting and splitting of the absorption peaks in the UV-vis spectrum due to temperature effects (dynamics of single-electron orbitals) as compared to the calculations for the known static structure.

The experimental crystal structure (ref. 6) was used as our initial point for the calculations. Density-functional theory (DFT) implemented in the real-space code-package GPAW[38] was used to calculate the wave functions and eigenenergies for the Kohn–Sham states. Relativistic effects for gold are included in GPAW setups. All DFT calculations were performed using the PBE (Perdew–Burke–Ernzerhof) functional.[39] The structural optimization has been done by 0.2 Å grid spacing and 0.01 eV $Å^{-1}$ convergence criterion for the maximum forces acting on atoms in the cluster. Molecular dynamics (MD) simulations were done using the Langevin thermostat with 0.01 friction parameter and 2 fs time step that is justified by treating all hydrogen atoms as deuteriums during the simulation. The dynamics was collected at three different temperatures 145 K, 280 K and 475 K. The total length of the simulation runs were 20 ps for 145 K, 10 ps for 280 K and 30 ps for 475 K including heating. Analysis was done after the thermalization stage, which takes less than 2 ps at 475 K, ~4 ps at 148 K and 2 ps in the 280 K run. From these results, the 475 K run was continued after the 280 K run. 120 optical spectra were calculated after thermalization for the MD snapshot structures with an increment of 65 steps using 145 K and 475 K data and 50 spectra with an increment of 65 steps using 280 K data. Absorption spectra were calculated using linear response time dependent density functional theory (lr-TDDFT) as implemented in GPAW software.[40] Spectra were calculated using 0.25 Å grid spacing and the PBE functional for the wavefunctions and for the lr-TDDFT kernel.

A previous study on $[Au_6(NHC\text{-}S)_4]^{2+}$ revealed that this cluster is made up of an anti-prismatic central Au_6 core supported by four NHC-thiolate ligand groups composed of two neutral $[(NHC\text{-}S)_2Au_2]$ staple-type units. The PBE-relaxed single crystal structure, shown in Fig. 1, was used as our starting point to run DFT-MD calculations at three different temperatures: 145 K, 280 K, and 475 K. Fig. 1a depicts two gold atoms Au_a and Au_b, which are uniquely positioned as part of the SR–Au–SR staple units, and the distance between the two gold atoms and the dihedral angle shown in Fig. 1b and c, respectively, are used as two of the key parameters to study the isomer configurations.

Fig. 2 shows the total energy behavior of the system at three temperatures 145 K, 280 K and 475 K as a function of time. To

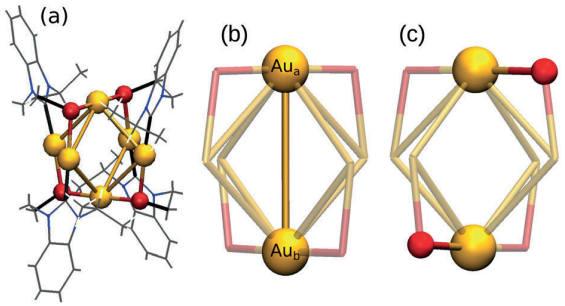

Fig. 1 (a) PBE-optimized structure of $[Au_6(NHC\text{-}S)_4]^{2+}$. (b) Au_a-Au_b distance – 4.74 Å part of the SR-Au-SR linear motif. (c) Dihedral angle – 89.10° in S–Au–Au–S. (Au: golden, S: red, N: blue, C: gray, H: white).

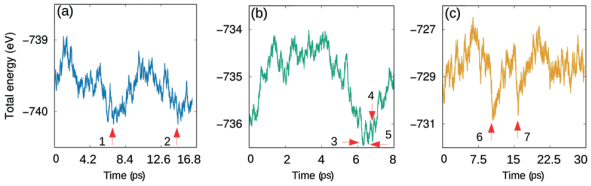

Fig. 2 Total energy as a function of time for DFT-MD runs in (a) 145 K, (b) 280 K and (c) 475 K. The selected isomers are labeled 1–7.

find potential isomer configurations, seven structures from the MD-runs were chosen and optimized (labeled in Fig. 2 and visualized in Fig. S2, ESI†) based on their proximity to the local minimum in terms of energy. The previously introduced Au_a–Au_b bond and dihedral angle were determined to analyse the differences of the structures. The results presented in Table S1 (ESI†) indicate that the Au_a–Au_b distance varies between 3.51 Å–3.83 Å, and the dihedral angles get values between 94° and 106°. Compared to the crystal structure there is a considerable change in the structure that gets more compact and twisted by the two protecting unit ends, which happens without any bond breaking. As a general trend, the largest twisting connects to the most compact structures. Interestingly, the crystal structure is not part of the structural phase space seen in the MD-simulation. With an energy of 0.19–0.42 eV per cluster, all the observed isomers are more stable than the single crystal structure. The most stable structure is the isomer number 2 as labeled in Fig. 2 at 145 K (check the structure for isomer 2 in Fig. S1a (ESI†).

Next, we studied systematically dynamical and structural effects on the electronic structure of the cluster at different temperatures. Fig. 3 shows the distribution of the energy gap values between the HOMO and LUMO as a function of the Au_a–Au_b distance at 145 K, 280 K, and 475 K.

The initial distance for the relaxed single crystal cluster is 4.74 Å, and the HOMO–LUMO gap is 3.22 eV. As shown in Fig. 3, universal correlation can be seen at all three temperatures; the HOMO–LUMO energy gap value is lower for configurations with shorter Au_a–Au_b distance. Furthermore, the

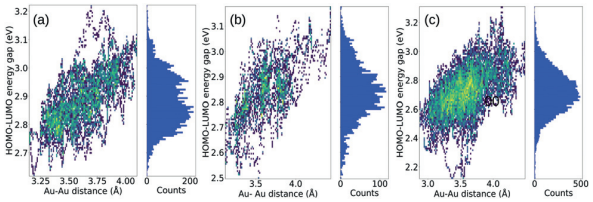

Fig. 3 Heat and distribution maps of the HOMO–LUMO gap variation with respect to the Au_a–Au_b distance at three temperatures: (a) 145 K, (b) 280 K and (c) 475 K. Lighter colors in the heat maps indicate the most densely populated area with similar HOMO–LUMO energy gap values.

distribution of the HOMO–LUMO gap values (Fig. 3 right vertical panels) is centered at about 2.85 eV for 145 K, 2.78–2.85 eV for 280 K and 2.6–2.8 eV for 475 K. The shape approaches normal distribution at higher temperatures. The central region is the most densely populated area also based on the scatter map plots. Note that the thermalization part has been removed from the data.

Fig. 4 shows a diagram of the energy levels for occupied states (a) and unoccupied states (b) as a function of time at 145 K. The energy of the HOMO state fluctuates strongly, within 0.5 eV, and over time this eigenenergy splits from the "band" of lower-lying states. The energies of the other states either increase or decrease in comparison to the PBE-relaxed crystal structure, but with much smaller fluctuations than the HOMO.

It is now intriguing to see how the optical absorption spectrum as one of the key signatures of electronic structure changes. Optical absorption spectra were calculated for three temperatures. Fig. 5 shows computed lr-TDDFT spectra of the static single crystal structure after structural optimization presented as a folded spectrum of electron–hole excitations compared to the dynamical multi-structure spectrum calculated from 145 K DFT-MD simulation. Temperature dependent spectra are combined from the single particle transitions calculated and collected for 120 snapshot structures that are chosen in every 65 steps after thermalization.

Absorption spectra show that even minor changes in the structure have a considerable impact on optical behaviour (Au_a–Au_b bond lengths and dihedral angle values of the selected isomers and single crystal structure are listed in Table S1, ESI†). Optical absorption spectra of DFT-MD findings in Fig. 5 show four absorption bands. The first peak appears

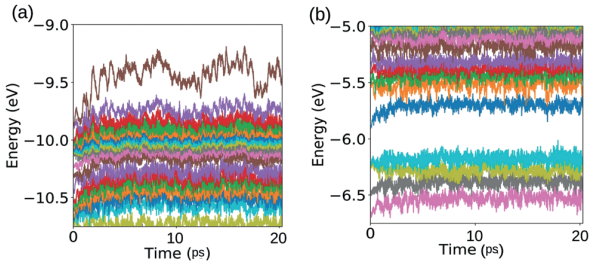

Fig. 4 Energies of the electron states (drawn in diverse colors) as a function of time at 145 K for (a) occupied and (b) unoccupied states.

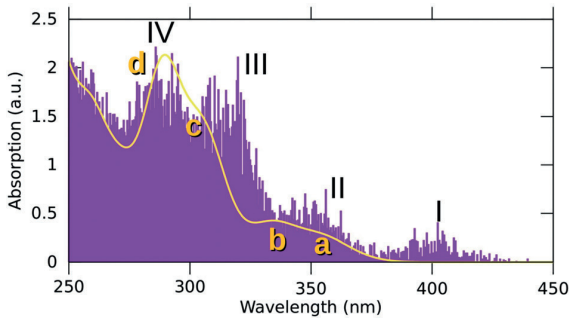

Fig. 5 Optical absorption spectra in 145 K as combined from 120 snapshot structures (purple lines) chosen in every 65 steps compared to the single crystal structure (yellow curve). Spectrum for the dynamic structures is shown as a stick spectrum including all single particle transitions and their oscillator strengths from the 120 structures that are collected into energy bins (peaks I–IV). The spectrum of the optimized single crystal structure is broadened by 0.1 eV Gaussians (peaks a–d).

around 400 nm (I) which is absent in the PBE-optimized single crystal structure. The remaining peaks appear at about 350 nm (II), 310 nm (III) and 285 nm (IV) whereas the single crystal structure displays two prominent peaks at 290 nm (d) and 335 nm (b) as well as two weak shoulders at 305 nm (c) and 355 nm (a). The first three absorption peaks (a), (b) and (c) in the single crystal structure are blue-shifted, while the fourth peak (d) shows a comparable agreement with that for DFT-MD (IV). Absorption spectra calculated for 280 K display four peaks, however, there are no discrete peaks in 475 K (check Fig. S3 for 280 K and Fig. S4 for 475 K results, ESI†).

To understand the origin of the optical absorption peaks for the single crystal structure and dynamic structures, we computed the dipole transition contribution maps (DTCMs). Fig. S5 (ESI†) shows DTCMs for the selected dynamic structure in 145 K. Red/blue dots in DTCMs represent the relative (strengthening/screening) contributions of single electron–hole excitations to the total transition dipole moment. To reduce the computational load, one representative structure from 120 configurations was selected for analysing the origin of the first and the fourth absorption peaks. The selected structure has the highest resemblance of peak locations to those of the combined spectrum shown in Fig. 5, so that less costly DTCM computations could be obtained. The first and fourth absorption peaks at 396 nm and 288 nm (shown by the arrows in the bottom right panels) are analyzed in Fig. S5 (ESI†). The bottom horizontal and right vertical panels illustrate the occupied (negative energies) and the unoccupied (positive energies) electron states. The absorption for the first peak at 396 nm arises from the HOMO to LUMO+1 transition (Fig. S5a, ESI†), whereas the second peak (Fig. S5b, ESI†) has several contributions from states below the HOMO to states above the LUMO. Higher energy peaks are composed of increasing numbers of transitions and are more collective (DTCMs for the third and the fourth peaks at 145 K shown in Fig. S6a and b, ESI†). Fig. S5c (ESI†) depicts DTCMs for the optimized single crystal structure. The first peak at 355 nm is combined of two main transitions

from HOMO to LUMO+1 and HOMO−1 to LUMO. Note that the finite-temperature dynamics splits this peak into two in Fig. S5a (ESI†). This is due to the splitting and decoupling of the HOMO away from the deeper states as shown in Fig. 4a. (DTCMs for the third and fourth peaks for the chosen dynamic structure shown in Fig. S6, ESI,† and DTCMs for the second, third and fourth peaks for the relaxed crystal presented in Fig. S7, ESI†).

To relate the observed crystal structure to the optimal gas phase isomer, we did a 7.4 ps MD simulation starting from the lowest-energy gas phase isomer 2, surrounding it with counterions (10 PF_6^-) and solvent molecules (2 EtOH) in the crystal structure symmetry.[6] The total charge was set to 8- and the central P- and C-atoms of PF_6^- and EtOH were fixed. Interestingly, the cluster changes spontaneously back to the crystal structure conformation when heating starts, as shown in Fig. S8 (ESI†). Compared to gas phase isomers (Table S1 and Fig. S2, ESI†), the Au–Au distance increases drastically and fluctuates around 4.6 Å. Simultaneously, the S–Au–Au–S dihedral angle decreases and oscillates around 85°. Hence, isomerization happens spontaneously in both directions between the gas and crystal phases. Optimization of the packing and interactions to counterions and solvent molecules in the crystal stabilizes a structure that is not seen in the gas phase isomers.

We have shown that DFT-MD calculation is an effective approach to analyze previously studied cluster $[Au_6(NHC\text{-}S)_4]^{2+}$ in order to find possible isomers at different temperatures. The current findings show the presence of at least seven isomers at three different temperatures: 145 K, 280 K, and 475 K. The isomer transition occurs at low temperature without any bond breakage and is shown to be reversible if the cluster environment is changed. In general, we have shown that the optical and electronic properties of a cluster can be very different depending on the exact structure and therefore understanding the isomerism better for protected metal clusters aids designing them for different applications. In this study, we imply that the crystallized structure is not automatically the lowest energy isomer in the gas phase or *vice versa*. In contrast to the small molecules, protected metal clusters are computationally more demanding and it is not self-evident whether their crystal, gas or solution phase structures should or should not be the same – even less is understood regarding how isomerization affects properties such as the catalytic activity.

This work was supported by the Academy of Finland (grants 315549 and 319208). The computations were done at the JYU node of the Finnish national FCCI infrastructure.

Conflicts of interest

There are no conflicts to declare.

Notes and references

1 R. Jin, C. Zeng, M. Zhou and Y. Chen, *Chem. Rev.*, 2016, **116**, 10346–10413.
2 P. M. Clusters, *From Fundamentals to Applications*, Elsevier, Amsterdam, 2015, vol. 9.
3 Q.-Y. Zhang and L. Zhao, *Tetrahedron Lett.*, 2018, **59**, 310–316.
4 I. Chakraborty and T. Pradeep, *Chem. Rev.*, 2017, **117**, 8208–8271.
5 R. R. Nasaruddin, T. Chen, N. Yan and J. Xie, *Coord. Chem. Rev.*, 2018, **368**, 60–79.
6 K. Salorinne, R. W. Man, P. A. Lummis, M. S. A. Hazer, S. Malola, J. C.-H. Yim, A. J. Veinot, W. Zhou, H. Häkkinen and M. Nambo, *et al.*, *Chem. Commun.*, 2020, **56**, 6102–6105.
7 H. Shen, Z. Xu, M. S. A. Hazer, Q. Wu, J. Peng, R. Qin, S. Malola, B. K. Teo, H. Häkkinen and N. Zheng, *Angew. Chem., Int. Ed.*, 2021, **60**, 3752–3758.
8 M. Brust, M. Walker, D. Bethell, D. J. Schiffrin and R. Whyman, *J. Chem. Soc., Chem. Commun.*, 1994, 801–802.
9 Q. Yao, T. Chen, X. Yuan and J. Xie, *Acc. Chem. Res.*, 2018, **51**, 1338–1348.
10 S. Hossain, Y. Niihori, L. V. Nair, B. Kumar, W. Kurashige and Y. Negishi, *Acc. Chem. Res.*, 2018, **51**, 3114–3124.
11 R. L. Whetten, H.-C. Weissker, J. J. Pelayo, S. M. Mullins, X. López-Lozano and I. L. Garzón, *Acc. Chem. Res.*, 2019, **52**, 34–43.
12 Y. Pei, P. Wang, Z. Ma and L. Xiong, *Acc. Chem. Res.*, 2018, **52**, 23–33.
13 J. Yan, B. K. Teo and N. Zheng, *Acc. Chem. Res.*, 2018, **51**, 3084–3093.
14 H. Yang, Y. Wang, H. Huang, L. Gell, L. Lehtovaara, S. Malola, H. Häkkinen and N. Zheng, *Nat. Commun.*, 2013, **4**, 1–8.
15 H. Yang, Y. Wang, X. Chen, X. Zhao, L. Gu, H. Huang, J. Yan, C. Xu, G. Li and J. Wu, *et al.*, *Nat. Commun.*, 2016, **7**, 1–8.
16 W. Kurashige, Y. Niihori, S. Sharma and Y. Negishi, *J. Phys. Chem. Lett.*, 2014, **5**, 4134–4142.
17 Y. Song, S. Wang, J. Zhang, X. Kang, S. Chen, P. Li, H. Sheng and M. Zhu, *J. Am. Chem. Soc.*, 2014, **136**, 2963–2965.
18 Z. Lei, X.-K. Wan, S.-F. Yuan, Z.-J. Guan and Q.-M. Wang, *Acc. Chem. Res.*, 2018, **51**, 2465–2474.
19 K. Konishi, M. Iwasaki and Y. Shichibu, *Acc. Chem. Res.*, 2018, **51**, 3125–3133.
20 Q.-F. Zhang, X. Chen and L.-S. Wang, *Acc. Chem. Res.*, 2018, **51**, 2159–2168.
21 M. Haruta, N. Yamada, T. Kobayashi and S. Iijima, *J. Catal.*, 1989, **115**, 301–309.
22 W. Chen and S. Chen, *Functional nanometer-sized clusters of transition metals: Synthesis, properties and applications*, Royal Society of Chemistry, 2014, vol. 7.
23 K. M. Jensen, P. Juhas, M. A. Tofanelli, C. L. Heinecke, G. Vaughan, C. J. Ackerson and S. J. Billinge, *Nat. Commun.*, 2016, **7**, 1–8.
24 X. Sun, P. Wang, L. Xiong and Y. Pei, *Chem. Phys. Lett.*, 2018, **704**, 68–75.
25 W. W. Xu, X. C. Zeng and Y. Gao, *Nanoscale*, 2018, **10**, 9476–9483.
26 R. Juarez Mosqueda, S. Malola and H. Häkkinen, *Eur. Phys. J. D*, 2019, **73**, 62.
27 H. Qian, W. T. Eckenhoff, Y. Zhu, T. Pintauer and R. Jin, *J. Am. Chem. Soc.*, 2010, **132**, 8280–8281.
28 S. Tian, Y.-Z. Li, M.-B. Li, J. Yuan, J. Yang, Z. Wu and R. Jin, *Nat. Commun.*, 2015, **6**, 1–7.
29 K. Taylor, C. Pettiette-Hall, O. Cheshnovsky and R. Smalley, *J. Chem. Phys.*, 1992, **96**, 3319–3329.
30 F. Furche, R. Ahlrichs, P. Weis, C. Jacob, S. Gilb, T. Bierweiler and M. M. Kappes, *J. Chem. Phys.*, 2002, **117**, 6982–6990.
31 P. Weis, *Int. J. Mass Spectrom.*, 2005, **245**, 1–13.
32 A. Fielicke, A. Kirilyuk, C. Ratsch, J. Behler, M. Scheffler, G. von Helden and G. Meijer, *Phys. Rev. Lett.*, 2004, **93**, 023401.
33 P. Gruene, D. M. Rayner, B. Redlich, A. F. van der Meer, J. T. Lyon, G. Meijer and A. Fielicke, *Science*, 2008, **321**, 674–676.
34 X. Xing, B. Yoon, U. Landman and J. H. Parks, *Phys. Rev. B: Condens. Matter Mater. Phys.*, 2006, **74**, 165423.
35 M. F. Matus, S. Malola, E. K. Bonilla, B. M. Barngrover, C. M. Aikens and H. Häkkinen, *Chem. Commun.*, 2020, **56**, 8087–8090.
36 E. Kalenius, S. Malola, M. F. Matus, R. Kazan, T. Burgi and H. Hakkinen, *J. Am. Chem. Soc.*, 2021, **143**, 1273–1277.
37 Y. Cao, S. Malola, M. F. Matus, T. Chen, Q. Yao, R. Shi, H. Häkkinen and J. Xie, *Chem*, 2021, **7**, 2227–2244.
38 J. Enkovaara, C. Rostgaard, J. J. Mortensen, J. Chen, M. Dułak, L. Ferrighi, J. Gavnholt, C. Glinsvad, V. Haikola and H. Hansen, *et al.*, *J. Phys.: Condens. Matter*, 2010, **22**, 253202.
39 J. P. Perdew, K. Burke and M. Ernzerhof, *Phys. Rev. Lett.*, 1996, **77**, 3865–3868.
40 M. Walter, H. Häkkinen, L. Lehtovaara, M. Puska, J. Enkovaara, C. Rostgaard and J. J. Mortensen, *J. Chem. Phys.*, 2008, **128**, 244101.

Supporting Information:

Table S1. Au_a-Au_b distance part of SR-Au-SR linear motif and dihedral values in S-Au-Au-S including relaxed energy values.

Temp. (K)	Isomer numbers as labeled in Fig. 2	Dihedral angle [°] S-Au- Au -S	Distance [Å] Au-Au	Relaxed energy [eV]
-	Static crystal structure	89.3	4.7	0
145	1	100.4	3.6	−0.40
145	2	101.6	3.8	−0.412
280	3	103.6	3.6	−0.32
280	4	99.4	3.7	−0.33
280	5	100.4	3.8	−0.35
475	6	94.7	3.8	−0.19
475	7	106.6	3.5	−0.33

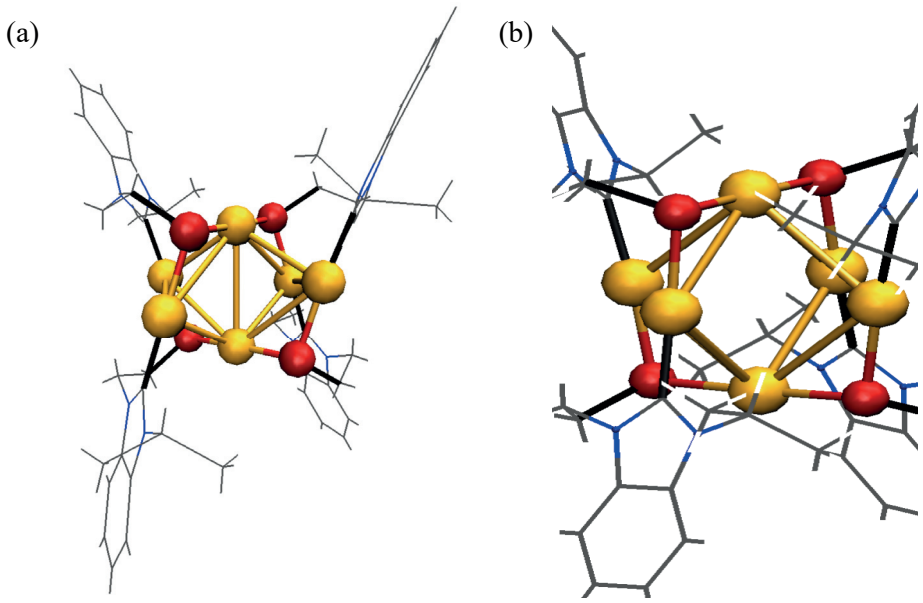

Fig. S1 (a) Optimized structure of isomer 2 (as labeled in Fig. 2), (b) optimized structure of static single crystal structure. The Au-Au distance in isomer 2 is 3.8 Å and dihedral angle value is 101.6°, the Au-Au distance in single crystal structure is 4.7 Å and dihedral angle is 89.3°.

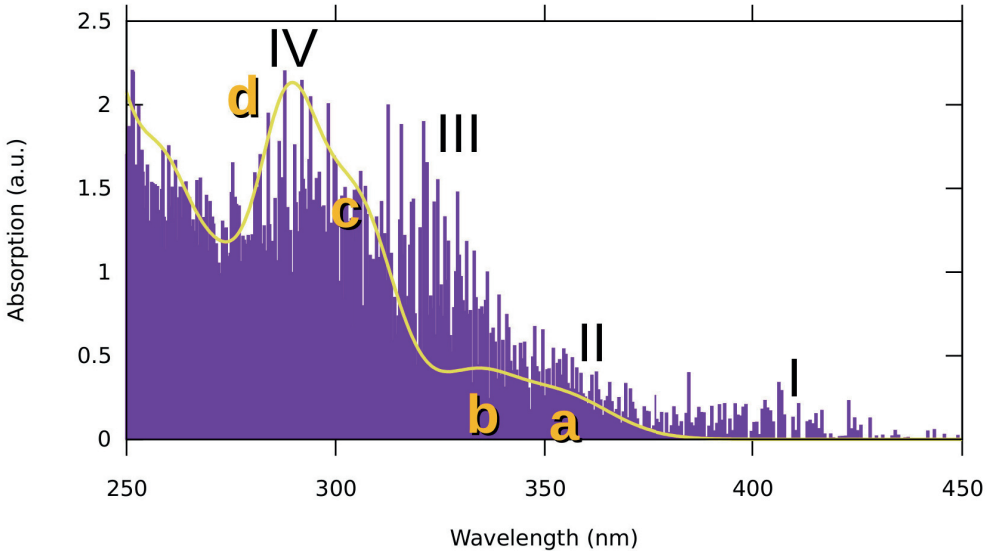

Fig. S2 Optical absorption spectra in 280 K as combined from 50 snapshot structures (purple lines) chosen in every 65 steps compared to static single crystal structure (yellow curve). Spectrum for the dynamic structures is shown as a stick spectrum including all single particle transitions and their oscillator strengths from the 50 structures that are collected into energy bins. The spectrum for optimized static crystal structure is broadened by 0.1 ev Gaussians.

Fig. S3

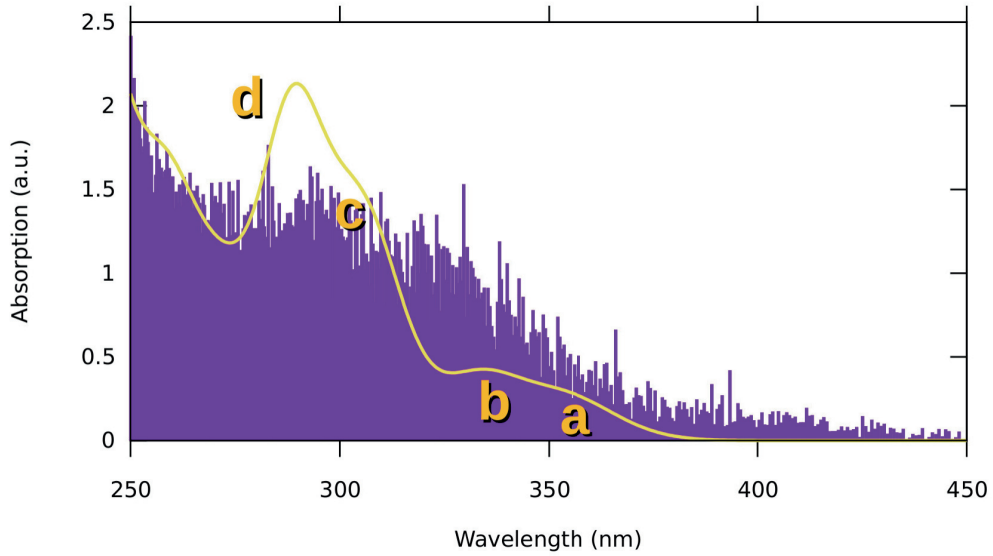

Optical absorption spectra in 475 K as combined from 120 snapshot structures (purple lines) chosen in every 65 steps compared to static single crystal structure (yellow curve). Discrete peaks oscillator strengths are not visible at 475 K, as they are in 145 K and 280 K.

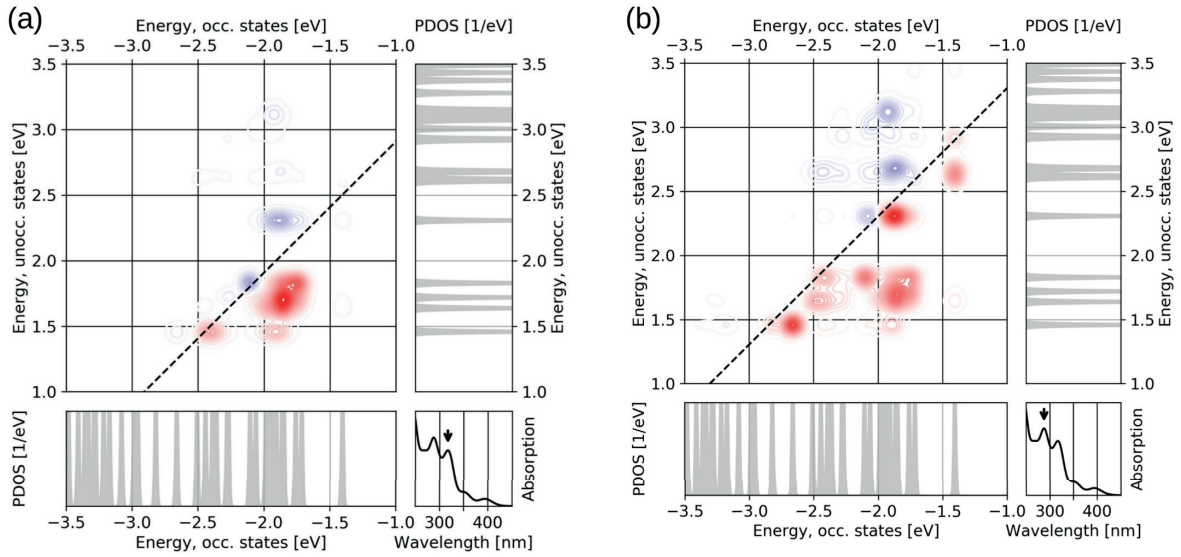

Fig. S4 DTCM for the chosen dynamic structure showing strengthening and sreening contributions in red and blue respectively for the selected absorption peak that is label with the spectrum in the lower right panel (a) peak III (b) peak IV. The occupied and the unoccupied electron states are shown in the bottom left sub-plot and on the right sub-plot respectively.

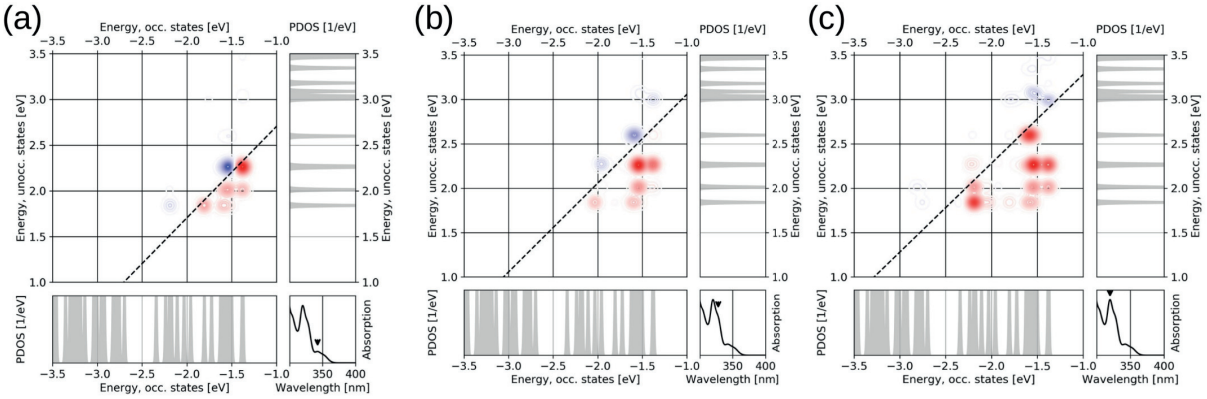

Fig. S5 The same as in Figure S4 but the peaks second, third and fourth for relaxed crystal structure in (a), (b) and (c) panels respectively.

DEPARTMENT OF CHEMISTRY, UNIVERSITY OF JYVÄSKYLÄ
RESEARCH REPORT SERIES

1. Vuolle, Mikko: Electron paramagnetic resonance and molecular orbital study of radical ions generated from (2.2)metacyclophane, pyrene and its hydrogenated compounds by alkali metal reduction and by thallium(III)trifluoroacetate oxidation. (99 pp.) 1976
2. Pasanen, Kaija: Electron paramagnetic resonance study of cation radical generated from various chlorinated biphenyls. (66 pp.) 1977
3. Carbon-13 Workshop, September 6-8, 1977. (91 pp.) 1977
4. Laihia, Katri: On the structure determination of norbornane polyols by NMR spectroscopy. (111 pp.) 1979
5. Nyrönen, Timo: On the EPR, ENDOR and visible absorption spectra of some nitrogen containing heterocyclic compounds in liquid ammonia. (76 pp.) 1978
6. Talvitie, Antti: Structure determination of some sesquiterpenoids by shift reagent NMR. (54 pp.) 1979
7. Häkli, Harri: Structure analysis and molecular dynamics of cyclic compounds by shift reagent NMR. (48 pp.) 1979
8. Pitkänen, Ilkka: Thermodynamics of complexation of 1,2,4-triazole with divalent manganese, cobalt, nickel, copper, zinc, cadmium and lead ions in aqueous sodium perchlorate solutions. (89 pp.) 1980
9. Asunta, Tuula: Preparation and characterization of new organometallic compounds synthesized by using metal vapours. (91 pp.) 1980
10. Sattar, Mohammad Abdus: Analyses of MCPA and its metabolites in soil. (57 pp.) 1980
11. Bibliography 1980. (31 pp.) 1981
12. Knuuttila, Pekka: X-Ray structural studies on some divalent 3d metal compounds of picolinic and isonicotinic acid N-oxides. (77 pp.) 1981
13. Bibliography 1981. (33 pp.) 1982
14. 6^{th} National NMR Symposium, September 9-10, 1982, Abstracts. (49 pp.) 1982
15. Bibliography 1982. (38 pp.) 1983
16. Knuuttila, Hilkka: X-Ray structural studies on some Cu(II), Co(II) and Ni(II) complexes with nicotinic and isonicotinic acid N-oxides. (54 pp.) 1983
17. Symposium on inorganic and analytical chemistry May 18, 1984, Program and Abstracts. (100 pp.) 1984
18. Knuutinen, Juha: On the synthesis, structure verification and gas chromatographic determination of chlorinated catechols and guaiacols occuring in spent bleach liquors of kraft pulp mill. (30 pp.) 1984
19. Bibliography 1983. (47 pp.) 1984
20. Pitkänen, Maija: Addition of BrCl, B_2 and Cl_2 to methyl esters of propenoic and 2-butenoic acid derivatives and ^{13}C NMR studies on methyl esters of saturated aliphatic mono- and dichlorocarboxylic acids. (56 pp.) 1985
21. Bibliography 1984. (39 pp.) 1985
22. Salo, Esa: EPR, ENDOR and TRIPLE spectroscopy of some nitrogen heteroaromatics in liquid ammonia. (111 pp.) 1985

23. Humppi, Tarmo: Synthesis, identification and analysis of dimeric impurities of chlorophenols. (39 pp.) 1985
24. Aho, Martti: The ion exchange and adsorption properties of sphagnum peat under acid conditions. (90 pp.) 1985
25. Bibliography 1985 (61 pp.) 1986
26. Bibliography 1986. (23 pp.) 1987
27. Bibliography 1987. (26 pp.) 1988
28. Paasivirta, Jaakko (Ed.): Structures of organic environmental chemicals. (67 pp.) 1988
29. Paasivirta, Jaakko (Ed.): Chemistry and ecology of organo-element compounds. (93 pp.) 1989
30. Sinkkonen, Seija: Determination of crude oil alkylated dibenzothiophenes in environment. (35 pp.) 1989
31. Kolehmainen, Erkki (Ed.): XII National NMR Symposium Program and Abstracts. (75 pp.) 1989
32. Kuokkanen, Tauno: Chlorocymenes and Chlorocymenenes: Persistent chlorocompounds in spent bleach liquors of kraft pulp mills. (40 pp.) 1989
33. Mäkelä, Reijo: ESR, ENDOR and TRIPLE resonance study on substituted 9,10-anthraquinone radicals in solution. (35 pp.) 1990
34. Veijanen, Anja: An integrated sensory and analytical method for identification of off-flavour compounds. (70 pp.) 1990
35. Kasa, Seppo: EPR, ENDOR and TRIPLE resonance and molecular orbital studies on a substitution reaction of anthracene induced by thallium(III) in two fluorinated carboxylic acids. (114 pp.) 1990
36. Herve, Sirpa: Mussel incubation method for monitoring organochlorine compounds in freshwater recipients of pulp and paper industry. (145 pp.) 1991
37. Pohjola, Pekka: The electron paramagnetic resonance method for characterization of Finnish peat types and iron (III) complexes in the process of peat decomposition. (77 pp.) 1991
38. Paasivirta, Jaakko (Ed.): Organochlorines from pulp mills and other sources. Research methodology studies 1988-91. (120 pp.) 1992
39. Veijanen, Anja (Ed.): VI National Symposium on Mass Spectrometry, May 13-15, 1992, Abstracts. (55 pp.) 1992
40. Rissanen, Kari (Ed.): The 7. National Symposium on Inorganic and Analytical Chemistry, May 22, 1992, Abstracts and Program. (153 pp.) 1992
41. Paasivirta, Jaakko (Ed.): CEOEC'92, Second Finnish-Russian Seminar: Chemistry and Ecology of Organo-Element Compounds. (93 pp.) 1992
42. Koistinen, Jaana: Persistent polychloroaromatic compounds in the environment: structure-specific analyses. (50 pp.) 1993
43. Virkki, Liisa: Structural characterization of chlorolignins by spectroscopic and liquid chromatographic methods and a comparison with humic substances. (62 pp.) 1993
44. Helenius, Vesa: Electronic and vibrational excitations in some

biologically relevant molecules. (30 pp.) 1993

45. Leppä-aho, Jaakko: Thermal behaviour, infrared spectra and x-ray structures of some new rare earth chromates(VI). (64 pp.) 1994
46. Kotila, Sirpa: Synthesis, structure and thermal behavior of solid copper(II) complexes of 2-amino-2- hydroxymethyl-1,3-propanediol. (111 pp.) 1994
47. Mikkonen, Anneli: Retention of molybdenum(VI), vanadium(V) and tungsten(VI) by kaolin and three Finnish mineral soils. (90 pp.) 1995
48. Suontamo, Reijo: Molecular orbital studies of small molecules containing sulfur and selenium. (42 pp.) 1995
49. Hämäläinen, Jouni: Effect of fuel composition on the conversion of fuel-N to nitrogen oxides in the combustion of small single particles. (50 pp.) 1995
50. Nevalainen, Tapio: Polychlorinated diphenyl ethers: synthesis, NMR spectroscopy, structural properties, and estimated toxicity. (76 pp.) 1995
51. Aittola, Jussi-Pekka: Organochloro compounds in the stack emission. (35 pp.) 1995
52. Harju, Timo: Ultrafast polar molecular photophysics of (dibenzylmethine)borondifluoride and 4-aminophthalimide in solution. (61 pp.) 1995
53. Maatela, Paula: Determination of organically bound chlorine in industrial and environmental samples. (83 pp.) 1995
54. Paasivirta, Jaakko (Ed.): CEOEC'95, Third Finnish-Russian Seminar: Chemistry and Ecology of Organo-Element Compounds. (109 pp.) 1995
55. Huuskonen, Juhani: Synthesis and structural studies of some supramolecular compounds. (54 pp.) 1995
56. Palm, Helena: Fate of chlorophenols and their derivatives in sawmill soil and pulp mill recipient environments. (52 pp.) 1995
57. Rantio, Tiina: Chlorohydrocarbons in pulp mill effluents and their fate in the environment. (89 pp.) 1997
58. Ratilainen, Jari: Covalent and non-covalent interactions in molecular recognition. (37 pp.) 1997
59. Kolehmainen, Erkki (Ed.): XIX National NMR Symposium, June 4-6, 1997, Abstracts. (89 pp.) 1997
60. Matilainen, Rose: Development of methods for fertilizer analysis by inductively coupled plasma atomic emission spectrometry. (41 pp.) 1997
61. Koistinen, Jari (Ed.): Spring Meeting on the Division of Synthetic Chemistry, May 15-16, 1997, Program and Abstracts. (36 pp.) 1997
62. Lappalainen, Kari: Monomeric and cyclic bile acid derivatives: syntheses, NMR spectroscopy and molecular recognition properties. (50 pp.) 1997
63. Laitinen, Eira: Molecular dynamics of cyanine dyes and phthalimides in solution: picosecond laser studies. (62 pp.) 1997
64. Eloranta, Jussi: Experimental and theoretical studies on some

quinone and quinol radicals. (40 pp.) 1997

65. Oksanen, Jari: Spectroscopic characterization of some monomeric and aggregated chlorophylls. (43 pp.) 1998
66. Häkkänen, Heikki: Development of a method based on laser-induced plasma spectrometry for rapid spatial analysis of material distributions in paper coatings. (60 pp.) 1998
67. Virtapohja, Janne: Fate of chelating agents used in the pulp and paper industries. (58 pp.) 1998
68. Airola, Karri: X-ray structural studies of supramolecular and organic compounds. (39 pp.) 1998
69. Hyötyläinen, Juha: Transport of lignin–type compounds in the receiving waters of pulp mills. (40 pp.) 1999
70. Ristolainen, Matti: Analysis of the organic material dissolved during totally chlorine-free bleaching. (40 pp.) 1999
71. Eklin, Tero: Development of analytical procedures with industrial samples for atomic emission and atomic absorption spectrometry. (43 pp.) 1999
72. Välisaari, Jouni: Hygiene properties of resol-type phenolic resin laminates. (129 pp.) 1999
73. Hu, Jiwei: Persistent polyhalogenated diphenyl ethers: model compounds syntheses, characterization and molecular orbital studies. (59 pp.) 1999
74. Malkavaara, Petteri: Chemometric adaptations in wood processing chemistry. (56 pp.) 2000
75. Kujala Elena, Laihia Katri, Nieminen Kari (Eds.): NBC 2000, Symposium on Nuclear, Biological and Chemical Threats in the 21st Century. (299 pp.) 2000
76. Rantalainen, Anna-Lea: Semipermeable membrane devices in monitoring persistent organic pollutants in the environment. (58 pp.) 2000
77. Lahtinen, Manu: *In situ* X-ray powder diffraction studies of Pt/C, CuCl/C and Cu_2O/C catalysts at elevated temperatures in various reaction conditions. (92 pp.) 2000
78. Tamminen, Jari: Syntheses, empirical and theoretical characterization, and metal cation complexation of bile acid-based monomers and open/closed dimers. (54 pp.) 2000
79. Vatanen, Virpi: Experimental studies by EPR and theoretical studies by DFT calculations of α-amino-9,10-anthraquinone radical anions and cations in solution. (37 pp.) 2000
80. Kotilainen, Risto: Chemical changes in wood during heating at 150-260 °C. (57 pp.) 2000
81. Nissinen, Maija: X-ray structural studies on weak, non-covalent interactions in supramolecular compounds. (69 pp.) 2001
82. Wegelius, Elina: X-ray structural studies on self-assembled hydrogen-bonded networks and metallosupramolecular complexes. (84 pp.) 2001
83. Paasivirta, Jaakko (Ed.): CEOEC'2001, Fifth Finnish-Russian Seminar: Chemistry and Ecology of Organo-Element Compounds. (163 pp.) 2001
84. Kiljunen, Toni: Theoretical studies on spectroscopy and

atomic dynamics in rare gas solids. (56 pp.) 2001

85. Du, Jin: Derivatives of dextran: synthesis and applications in oncology. (48 pp.) 2001
86. Koivisto, Jari: Structural analysis of selected polychlorinated persistent organic pollutants (POPs) and related compounds. (88 pp.) 2001
87. Feng, Zhinan: Alkaline pulping of non-wood feedstocks and characterization of black liquors. (54 pp.) 2001
88. Halonen, Markku: Lahon havupuun käyttö sulfaattiprosessin raaka-aineena sekä havupuun lahontorjunta. (90 pp.) 2002
89. Falábu, Dezsö: Synthesis, conformational analysis and complexation studies of resorcarene derivatives. (212 pp.) 2001
90. Lehtovuori, Pekka: EMR spectroscopic studies on radicals of ubiquinones Q-*n*, vitamin K_3 and vitamine E in liquid solution. (40 pp.) 2002
91. Perkkalainen, Paula: Polymorphism of sugar alcohols and effect of grinding on thermal behavior on binary sugar alcohol mixtures. (53 pp.) 2002
92. Ihalainen, Janne: Spectroscopic studies on light-harvesting complexes of green plants and purple bacteria. (42 pp.) 2002
93. Kunttu, Henrik, Kiljunen, Toni (Eds.): 4th International Conference on Low Temperature Chemistry. (159 pp.) 2002
94. Väisänen, Ari: Development of methods for toxic element analysis in samples with environmental concern by ICP-AES and ETAAS. (54 pp.) 2002
95. Luostarinen, Minna: Synthesis and characterisation of novel resorcarene derivatives. (200 pp.) 2002
96. Louhelainen, Jarmo: Changes in the chemical composition and physical properties of wood and nonwood black liquors during heating. (68 pp.) 2003
97. Lahtinen, Tanja: Concave hydrocarbon cyclophane π-prismands. (65 pp.) 2003
98. Laihia, Katri (Ed.): NBC 2003, Symposium on Nuclear, Biological and Chemical Threats – A Crisis Management Challenge. (245 pp.) 2003
99. Oasmaa, Anja: Fuel oil quality properties of wood-based pyrolysis liquids. (32 pp.) 2003
100. Virtanen, Elina: Syntheses, structural characterisation, and cation/anion recognition properties of nano-sized bile acid-based host molecules and their precursors. (123 pp.) 2003
101. Nättinen, Kalle: Synthesis and X-ray structural studies of organic and metallo-organic supramolecular systems. (79 pp.) 2003
102. Lampiselkä, Jarkko: Demonstraatio lukion kemian opetuksessa. (285 pp.) 2003
103. Kallioinen, Jani: Photoinduced dynamics of $Ru(dcbpy)_2(NCS)_2$ – in solution and on nanocrystalline titanium dioxide thin films. (47 pp.) 2004
104. Valkonen, Arto (Ed.): VII Synthetic Chemistry Meeting and XXVI Finnish NMR Symposium. (103 pp.) 2004

105. Vaskonen, Kari: Spectroscopic studies on atoms and small molecules isolated in low temperature rare gas matrices. (65 pp.) 2004
106. Lehtovuori, Viivi: Ultrafast light induced dissociation of $Ru(dcbpy)(CO)_2I_2$ in solution. (49 pp.) 2004
107. Saarenketo, Pauli: Structural studies of metal complexing Schiff bases, Schiff base derived *N*-glycosides and cyclophane π-prismands. (95 pp.) 2004
108. Paasivirta, Jaakko (Ed.): CEOEC'2004, Sixth Finnish-Russian Seminar: Chemistry and Ecology of Organo-Element Compounds. (147 pp.) 2004
109. Suontamo, Tuula: Development of a test method for evaluating the cleaning efficiency of hard-surface cleaning agents. (96 pp.) 2004
110. Güneş, Minna: Studies of thiocyanates of silver for nonlinear optics. (48 pp.) 2004
111. Ropponen, Jarmo: Aliphatic polyester dendrimers and dendrons. (81 pp.) 2004
112. Vu, Mân Thi Hong: Alkaline pulping and the subsequent elemental chlorine-free bleaching of bamboo (*Bambusa procera*). (69 pp.) 2004
113. Mansikkamäki, Heidi: Self-assembly of resorcinarenes. (77 pp.) 2006
114. Tuononen, Heikki M.: EPR spectroscopic and quantum chemical studies of some inorganic main group radicals. (79 pp.) 2005
115. Kaski, Saara: Development of methods and applications of laser-induced plasma spectroscopy in vacuum ultraviolet. (44 pp.) 2005
116. Mäkinen, Riika-Mari: Synthesis, crystal structure and thermal decomposition of certain metal thiocyanates and organic thiocyanates. (119 pp.) 2006
117. Ahokas, Jussi: Spectroscopic studies of atoms and small molecules isolated in rare gas solids: photodissociation and thermal reactions. (53 pp.) 2006
118. Busi, Sara: Synthesis, characterization and thermal properties of new quaternary ammonium compounds: new materials for electrolytes, ionic liquids and complexation studies. (102 pp.) 2006
119. Mäntykoski, Keijo: PCBs in processes, products and environment of paper mills using wastepaper as their raw material. (73 pp.) 2006
120. Laamanen, Pirkko-Leena: Simultaneous determination of industrially and environmentally relevant aminopolycarboxylic and hydroxycarboxylic acids by capillary zone electrophoresis. (54 pp.) 2007
121. Salmela, Maria: Description of oxygen-alkali delignification of kraft pulp using analysis of dissolved material. (71 pp.) 2007
122. Lehtovaara, Lauri: Theoretical studies of atomic scale impurities in superfluid ^{4}He. (87 pp.) 2007
123. Rautiainen, J. Mikko: Quantum chemical calculations of structures, bonding, and spectroscopic properties of some sulphur and selenium iodine cations. (71 pp.) 2007
124. Nummelin, Sami: Synthesis, characterization, structural and

retrostructural analysis of self-assembling pore forming dendrimers. (286 pp.) 2008

125. Sopo, Harri: Uranyl(VI) ion complexes of some organic aminobisphenolate ligands: syntheses, structures and extraction studies. (57 pp.) 2008
126. Valkonen, Arto: Structural characteristics and properties of substituted cholanoates and *N*-substituted cholanamides. (80 pp.) 2008
127. Lähde, Anna: Production and surface modification of pharmaceutical nano- and microparticles with the aerosol flow reactor. (43 pp.) 2008
128. Beyeh, Ngong Kodiah: Resorcinarenes and their derivatives: synthesis, characterization and complexation in gas phase and in solution. (75 pp.) 2008
129. Välisaari, Jouni, Lundell, Jan (Eds.): Kemian opetuksen päivät 2008: uusia oppimisympäristöjä ja ongelmalähtöistä opetusta. (118 pp.) 2008
130. Myllyperkiö, Pasi: Ultrafast electron transfer from potential organic and metal containing solar cell sensitizers. (69 pp.) 2009
131. Käkölä, Jaana: Fast chromatographic methods for determining aliphatic carboxylic acids in black liquors. (82 pp.) 2009
132. Koivukorpi, Juha: Bile acid-arene conjugates: from photoswitchability to cancer cell detection. (67 pp.) 2009
133. Tuuttila, Tero: Functional dendritic polyester compounds: synthesis and characterization of small bifunctional dendrimers and dyes. (74 pp.) 2009
134. Salorinne, Kirsi: Tetramethoxy resorcinarene based cation and anion receptors: synthesis, characterization and binding properties. (79 pp.) 2009
135. Rautiainen, Riikka: The use of first-thinning Scots pine (*Pinus sylvestris*) as fiber raw material for the kraft pulp and paper industry. (73 pp.) 2010
136. Ilander, Laura: Uranyl salophens: synthesis and use as ditopic receptors. (199 pp.) 2010
137. Kiviniemi, Tiina: Vibrational dynamics of iodine molecule and its complexes in solid krypton - Towards coherent control of bimolecular reactions? (73 pp.) 2010
138. Ikonen, Satu: Synthesis, characterization and structural properties of various covalent and non-covalent bile acid derivatives of N/O-heterocycles and their precursors. (105 pp.) 2010
139. Siitonen, Anni: Spectroscopic studies of semiconducting single-walled carbon nanotubes. (56 pp.) 2010
140. Raatikainen, Kari: Synthesis and structural studies of piperazine cyclophanes – Supramolecular systems through Halogen and Hydrogen bonding and metal ion coordination. (69 pp.) 2010
141. Leivo, Kimmo: Gelation and gel properties of two- and three-component Pyrene based low molecular weight organogelators. (116 pp.) 2011
142. Martiskainen, Jari: Electronic energy transfer in light-harvesting complexes isolated from *Spinacia oleracea* and from three

photosynthetic green bacteria *Chloroflexus aurantiacus*, *Chlorobium tepidum*, and *Prosthecochloris aestuarii*. (55 pp.) 2011

143. Wichmann, Oula: Syntheses, characterization and structural properties of [O,N,O,X´] aminobisphenolate metal complexes. (101 pp.) 2011
144. Ilander, Aki: Development of ultrasound-assisted digestion methods for the determination of toxic element concentrations in ash samples by ICP-OES. (58 pp.) 2011
145. The Combined XII Spring Meeting of the Division of Synthetic Chemistry and XXXIII Finnish NMR Symposium. Book of Abstracts. (90 pp.) 2011
146. Valto, Piia: Development of fast analysis methods for extractives in papermaking process waters. (73 pp.) 2011
147. Andersin, Jenni: Catalytic activity of palladium-based nanostructures in the conversion of simple olefinic hydro- and chlorohydrocarbons from first principles. (78 pp.) 2011
148. Aumanen, Jukka: Photophysical properties of dansylated poly(propylene amine) dendrimers. (55 pp.) 2011
149. Kärnä, Minna: Ether-functionalized quaternary ammonium ionic liquids – synthesis, characterization and physicochemical properties. (76 pp.) 2011
150. Jurček, Ondřej: Steroid conjugates for applications in pharmacology and biology. (57 pp.) 2011
151. Nauha, Elisa: Crystalline forms of selected Agrochemical actives: design and synthesis of cocrystals. (77 pp.) 2012
152. Ahkola, Heidi: Passive sampling in monitoring of nonylphenol ethoxylates and nonylphenol in aquatic environments. (92 pp.) 2012
153. Helttunen, Kaisa: Exploring the self-assembly of resorcinarenes: from molecular level interactions to mesoscopic structures. (78 pp.) 2012
154. Linnanto, Juha: Light excitation transfer in photosynthesis revealed by quantum chemical calculations and exiton theory. (179 pp.) 2012
155. Roiko-Jokela, Veikko: Digital imaging and infrared measurements of soil adhesion and cleanability of semihard and hard surfaces. (122 pp.) 2012
156. Noponen, Virpi: Amides of bile acids and biologically important small molecules: properties and applications. (85 pp.) 2012
157. Hulkko, Eero: Spectroscopic signatures as a probe of structure and dynamics in condensed-phase systems – studies of iodine and gold ranging from isolated molecules to nanoclusters. (69 pp.) 2012
158. Lappi, Hanna: Production of Hydrocarbon-rich biofuels from extractives-derived materials. (95 pp.) 2012
159. Nykänen, Lauri: Computational studies of Carbon chemistry on transition metal surfaces. (76 pp.) 2012
160. Ahonen, Kari: Solid state studies of pharmaceutically important molecules and their derivatives. (65 pp.) 2012

161. Pakkanen, Hannu: Characterization of organic material dissolved during alkaline pulping of wood and non-wood feedstocks. (76 pp.) 2012
162. Moilanen, Jani: Theoretical and experimental studies of some main group compounds: from closed shell interactions to singlet diradicals and stable radicals. (80 pp.) 2012
163. Himanen, Jatta: Stereoselective synthesis of Oligosaccharides by *De Novo* Saccharide welding. (133 pp.) 2012
164. Bunzen, Hana: Steroidal derivatives of nitrogen containing compounds as potential gelators. (76 pp.) 2013
165. Seppälä, Petri: Structural diversity of copper(II) amino alcohol complexes. Syntheses, structural and magnetic properties of bidentate amino alcohol copper(II) complexes. (67 pp.) 2013
166. Lindgren, Johan: Computational investigations on rotational and vibrational spectroscopies of some diatomics in solid environment. (77 pp.) 2013
167. Giri, Chandan: Sub-component self-assembly of linear and non-linear diamines and diacylhydrazines, formulpyridine and transition metal cations. (145 pp.) 2013
168. Riisiö, Antti: Synthesis, Characterization and Properties of Cu(II)-, Mo(VI)- and U(VI) Complexes With Diaminotetraphenolate Ligands. (51 pp.) 2013
169. Kiljunen, Toni (Ed.): Chemistry and Physics at Low Temperatures. Book of Abstracts. (103 pp.) 2013
170. Hänninen, Mikko: Experimental and Computational Studies of Transition Metal Complexes with Polydentate Amino- and Aminophenolate Ligands: Synthesis, Structure, Reactivity and Magnetic Properties. (66 pp.) 2013
171. Antila, Liisa: Spectroscopic studies of electron transfer reactions at the photoactive electrode of dye-sensitized solar cells. (53 pp.) 2013
172. Kemppainen, Eeva: Mukaiyama-Michael reactions with α-substituted acroleins – a useful tool for the synthesis of the pectenotoxins and other natural product targets. (190 pp.) 2013
173. Virtanen, Suvi: Structural Studies of Dielectric Polymer Nanocomposites. (49 pp.) 2013
174. Yliniemelä-Sipari, Sanna: Understanding The Structural Requirements for Optimal Hydrogen Bond Catalyzed Enolization – A Biomimetic Approach.(160 pp.) 2013
175. Leskinen, Mikko V: Remote β-functionalization of β'-keto esters. (105 pp.) 2014
176. 12th European Conference on Research in Chemistry Education (ECRICE2014). Book of Abstracts. (166 pp.) 2014
177. Peuronen, Anssi: N-Monoalkylated DABCO-Based N-Donors as Versatile Building Blocks in Crystal Engineering and Supramolecular Chemistry. (54 pp.) 2014
178. Perämäki, Siiri: Method development for determination and recovery of rare earth elements from industrial fly ash. (88 pp.) 2014

179. Chernyshev, Alexander, N.: Nitrogen-containing ligands and their platinum(IV) and gold(III) complexes: investigation and basicity and nucleophilicity, luminescence, and aurophilic interactions. (64 pp.) 2014
180. Lehto, Joni: Advanced Biorefinery Concepts Integrated to Chemical Pulping. (142 pp.) 2015
181. Tero, Tiia-Riikka: Tetramethoxy resorcinarenes as platforms for fluorescent and halogen bonding systems. (61 pp.) 2015
182. Löfman, Miika: Bile acid amides as components of microcrystalline organogels. (62 pp.) 2015
183. Selin, Jukka: Adsorption of softwood-derived organic material onto various fillers during papermaking. (169 pp.) 2015
184. Piisola, Antti: Challenges in the stereoselective synthesis of allylic alcohols. (210 pp.) 2015
185. Bonakdarzadeh, Pia: Supramolecular coordination polyhedra based on achiral and chiral pyridyl ligands: design, preparation, and characterization. (65 pp.) 2015
186. Vasko, Petra: Synthesis, characterization, and reactivity of heavier group 13 and 14 metallylenes and metalloid clusters: small molecule activation and more. (66 pp.) 2015
187. Topić, Filip: Structural Studies of Nano-sized Supramolecular Assemblies. (79 pp.) 2015
188. Mustalahti, Satu: Photodynamics Studies of Ligand-Protected Gold Nanoclusters by using Ultrafast Transient Infrared Spectroscopy. (58 pp.) 2015
189. Koivisto, Jaakko: Electronic and vibrational spectroscopic studies of gold-nanoclusters. (63 pp.) 2015
190. Suhonen, Aku: Solid state conformational behavior and interactions of series of aromatis oligoamide foldamers. (68 pp.) 2016
191. Soikkeli, Ville: Hydrometallurgical recovery and leaching studies for selected valuable metals from fly ash samples by ultrasound-assisted extraction followed by ICP-OES determination. (107 pp.) 2016
192. XXXVIII Finnish NMR Symposium. Book of Abstracts. (51 pp.) 2016
193. Mäkelä, Toni: Ion Pair Recognition by Ditopic Crown Ether Based bis-Urea and Uranyl Salophen Receptors. (75 pp.) 2016
194. Lindholm-Lehto, Petra: Occurrence of pharmaceuticals in municipal wastewater treatment plants and receiving surface waters in Central and Southern Finland. (98 pp.) 2016
195. Härkönen, Ville: Computational and Theoretical studies on Lattice Thermal conductivity and Thermal properties of Silicon Clathrates. (89 pp.) 2016
196. Tuokko, Sakari: Understanding selective reduction reactions with heterogeneous Pd and Pt: climbing out of the black box. (85 pp.) 2016
197. Nuora, Piia: Monitapaustutkimus LUMA-Toimintaan liittyvissä oppimisympäristöissä tapahtuvista kemian oppimiskokemuksista. (171 pp.) 2016

198. Kumar, Hemanathan: Novel Concepts on The Recovery of By-Products from Alkaline Pulping. (61 pp.) 2016
199. Arnedo-Sánchez, Leticia: Lanthanide and Transition Metal Complexes as Building Blocks for Supramolecular Functional Materials. (227 pp.) 2016
200. Gell, Lars: Theoretical Investigations of Ligand Protected Silver Nanoclusters. (134 pp.) 2016
201. Vaskuri, Juhani: Oppiennätyksistä opetussuunnitelman perusteisiin - lukion kemian kansallisen opetussuunnitelman kehittyminen Suomessa vuosina 1918-2016. (314 pp.) 2017
202. Lundell Jan, Kiljunen Toni (Eds.): 22nd Horizons in Hydrogen Bond Research. Book of Abstracts. 2017
203. Turunen, Lotta: Design and construction of halogen-bonded capsules and cages. (61 pp.) 2017
204. Hurmalainen, Juha: Experimental and computational studies of unconventional main group compounds: stable radicals and reactive intermediates. (88 pp.) 2017
205. Koivistoinen Juha: Non-linear interactions of femtosecond laser pulses with graphene: photo-oxidation, imaging and photodynamics. (68 pp.) 2017
206. Chen, Chengcong: Combustion behavior of black liquors: droplet swelling and influence of liquor composition. (39 pp.) 2017
207. Mansikkamäki, Akseli: Theoretical and Computational Studies of Magnetic Anisotropy and Exchange Coupling in Molecular Systems. (190 p. + included articles) 2018.
208. Tatikonda, Rajendhraprasad: Multivalent N-donor ligands for the construction of coordination polymers and coordination polymer gels. (62 pp.) 2018
209. Budhathoki, Roshan: Beneficiation, desilication and selective precipitation techniques for phosphorus refining from biomass derived fly ash. (64 pp.) 2018
210. Siitonen, Juha: Synthetic Studies on 1-azabicyclo[5.3.0]decane Alkaloids. (140 pp.) 2018
211. Ullah, Saleem: Advanced Biorefinery Concepts Related to Non-wood Feedstocks. (57 pp.) 2018
212. Ghalibaf, Maryam: Analytical Pyrolysis of Wood and Non-Wood Materials from Integrated Biorefinery Concepts. (106 pp.) 2018

DEPARTMENT OF CHEMISTRY, UNIVERSITY OF JYVÄSKYLÄ
DISSERTATIONS PUBLISHED IN THE JYU DISSERTATIONS RESEARCH SERIES

1. Bulatov, Evgeny: Synthetic and structural studies of covalent and non-covalent interactions of ligands and metal center in platinum(II) complexes containing 2,2′-dipyridylamine or oxime ligands. (58 pp.) 2019. JYU Dissertations 70.
2. Annala, Riia: Conformational Properties and Anion Complexes of Aromatic Oligoamide Foldamers. (80 pp.) 2019. JYU Dissertations 84.
3. Isoaho, Jukka Pekka: Dithionite Bleaching of Thermomechanical Pulp - Chemistry and Optimal Conditions. (73 pp.) 2019. JYU Dissertations 85.
4. Nygrén, Enni: Recovery of rubidium from power plant fly ash. (98 pp.) 2019. JYU Dissertations 136.
5. Kiesilä, Anniina: Supramolecular chemistry of anion-binding receptors based on concave macromolecules. (68 pp.) 2019. JYU Dissertations 137.
6. Sokolowska, Karolina: Study of water-soluble p-MBA-protected gold nanoclusters and their superstructures. (60 pp.) 2019. JYU Dissertations 167.
7. Lahtinen, Elmeri: Chemically Functional 3D Printing: Selective Laser Sintering of Customizable Metal Scavengers. (71 pp.) 2019. JYU Dissertations 175.
8. Larijani, Amir: Oxidative reactions of cellulose under alkaline conditions. (102 pp.) 2020. JYU Dissertations 217.
9. Kolari, Kalle: Metal-metal contacts in late transition metal polymers. (60 pp.) 2020. JYU Dissertations 220.
10. Kauppinen, Minttu: Multiscale computational investigation of catalytic properties of zirconia supported noble metals. (87 pp.) 2020. JYU Dissertations 231.
11. Ding, Xin: Halogen Bond in Crystal Engineering: Structural Studies on Crystals with Ruthenium Centered Complexes and 1-(4-Pyridyl)-4-thiopyridine Zwitterion as Halogen Bond Acceptors. (59 pp.) 2020. JYU Dissertations 323.
12. Neuvonen, Antti: Toward an Understanding of Hydrogen-Bonding Bifunctional Organocatalyst Conformations and Their Activity in Asymmetric Mannich Reactions. (77 pp.) 2020. JYU Dissertations 336.
13. Kortet, Sami: 2,5-Diarylpyrrolidines and Pyroglutamic-Acid-Derived 2-Diarylmethyl-5-Aryl-Pyrrolidines: Their Synthesis and Use in Asymmetric Synthesis. (221 pp.) 2020. JYU Dissertations 337.
14. Saarnio, Ville: Fluorescent probes, noble metal nanoparticles and their nanocomposites: detection of nucleic acids and other biological targets. (80 pp.) 2021. JYU Dissertations 361.
15. Chernysheva, Maria: σ-hole interactions: the effect of the donors and acceptors nature in selenoureas, thioureas, halogenated species, substituted benzenes, and their adducts. (72 pp.) 2021. JYU Dissertations 370.
16. Bulatova, Margarita: Noncovalent interactions as a tool for supramolecular self-assembly of metallopolymers. (62 pp.) 2021. JYU Dissertations 377.

17. Romppanen, Sari: Laser-spectroscopic studies of rare earth element- and lithium-bearing minerals and rocks. (66 pp.) 2021. JYU Dissertations 393.
18. Kukkonen, Esa: Nonlinear optical materials through weak interactions and their application in 3D printing. (58 pp.) 2021. JYU Dissertations 441.
19. Kuosmanen, Riikka: The Effect of Structure on the Gel Formation Ability and the Properties of Bile Acid Based Supramolecular Organogels. (68 pp.) 2021. JYU Dissertations 465.
20. Reuna, Sini: Development of a Method for Phosphorus Recovery from Wastewaters. (67 pp.) 2022. JYU Dissertations 486.
21. Taipale, Essi: Synthetic and Structural Studies on the Effect of Non-Covalent Interactions on N(*sp2*)-Heterocyclic Molecules. (67 pp.) 2022. JYU Dissertations 496.
22. Järvinen, Teemu: Molecular Dynamics View on Matrix Isolation. (143 pp.) 2022. JYU Dissertations 544.
23. Kumar, Parveen: Synthesis and Structural Studies on Halogen(I) Complexes. (160 pp.) 2022. JYU Dissertations 549.
24. Forsblom, Samu: Design and Construction of Metal-Organic Polyhedra. (212 pp.) 2022. JYU Dissertations 569.
25. Korpelin, Ville: Computational Studies of Catalytic Active Site Properties and Reactions at the Metal–Oxide Interface. (78 pp.) 2022. JYU Dissertations 578.
26. Vuori, Hannu: Extending Benson Group Increment Theory to Compounds of Phosphorus, Silicon, and Boron with Computational Chemistry. (59 pp.) 2022. JYU Dissertations 581.
27. Pallerla, Rajanish: Studies Towards Synthesis of Favipiravir & Humilisin E. (139 pp.) 2023. JYU Dissertations 611.
28. Taponen, Anni: Radical-Ion Salts based on Thiazyls and Tetracyanoquinodimethane: Hysteretic Magnetic Bistability in a Multicomponent System. (66 pp.) 2023. JYU Dissertations 613.
29. Aho, Noora: Molecular Dynamics Simulations of Acids and Bases in Biomolecular Environments. (78 pp.) 2023. JYU Dissertations 614.